ELECTRON MAGNETIC RESONANCE OF CHLOROPHYLLS: RADICAL ANIONS AND CATIONS

By

LEE MATTHEW WALKER

A DISSERTATION PRESENTED TO THE GRADUATE SCHOOL
OF THE UNIVERSITY OF FLORIDA IN PARTIAL FULFILLMENT
OF THE REQUIREMENTS FOR THE DEGREE OF
DOCTOR OF PHILOSOPHY

UNIVERSITY OF FLORIDA

2003

Copyright 2003

by

Lee Matthew Walker

This is for my parents.

ACKNOWLEDGMENTS

I would like to thank the University of Florida for the opportunity to earn this degree. Thanks also go to my advisor, Alex Angerhofer, for his guidance, inspiration, and encouragement, which have been so valuable over the years. I must also express my appreciation for the support and tutelage of Hans van Tol and Louis-Claude Brunel, who truly made this research possible. But, without the help of my organic friends, and the expertise and assistance of Andrew Ozarowski, Chris Chang and Peter Bratt, this graduation would have never come. Of course, you can't do research without money, so thanks to the NSF and NHMFL for the financial seeds they planted this work.

TABLE OF CONTENTS

page

ACKNOWLEDGMENTS iv

LIST OF TABLES vii

LIST OF FIGURES viii

ABSTRACT xi

CHAPTER

1 PHOTOSYNTHESIS 1

Energy Conversion 3
The Bacterial Reaction Center 4
Ionic Cofactors 7

2 MAGNETIC RESONANCE THEORY 10

Magnetic Moments and Angular Momenta 11
cw-EPR 13
g-Tensor 14
Hyperfine Interaction 16
cw-ENDOR 20
Orientational Selection 22
Pulsed EPR 24
Pulsed ENDOR 26
ESEEM 29

3 EXPERIMENTAL PROCEDURES 32

Bacteriochlorophyll *a* Purification 32
Bacteriopheophytin *a* Generation 33
Chlorophylls *a* and *b* -- Extraction and Purification 34
Radical Anion Generation 36
X-Band EPR/ENDOR 37
Transmission High Field cw-EPR 38
Quasioptic High Field cw-EPR/ENDOR 39
Magnetic Field Calibration Procedure 41

4 RESULTS 44

Bacteriochlorophyll *a* Radical Anion 44
Bacteriopheophytin *a* Radical Anion 53
Bacteriochlorophyll *a* Radical Cation 65
Bacteriopheophytin *a* Radical Cation 69
Chlorophyll *a* Radical Anion 72
Chlorophyll *b* 74

5 DISCUSSION 78

Bacteriochlorophyll *a* Radical Anion 78
Bacteriopheophytin *a* Radical Anion 91
Bacteriochlorophyll *a* Radical Cation 98
Bacteriopheophytin *a* Radical Cation 101
Chlorophyll Radical Anions 103

6 CONCLUSIONS 109

APPENDIX ABBREVIATIONS AND CONSTANTS 114

LIST OF REFERENCES 116

BIOGRAPHICAL SKETCH 127

LIST OF TABLES

Table page

4-1 Isotropic hyperfine coupling constants for BChl *a*$^{-}$ and BPheo *a*$^{-}$ 54

4-2 Davies and Mims ENDOR data for BChl *a* radical cation 69

4-3 BPheo *a* radical cation pulsed W-band ENDOR data 72

4-4 Radical anion g-tensor data 77

5-1 Isotropic hyperfine coupling constants estimated with DFT and X-Band EPR for BChl *a* anion 89

5-2 Radical Anion hyperfine tensor data 90

5-3 Hyperfine tensor data for BChl *a* and BPheo *a* radical anions 98

6-1 Radical anion g-values measured with high field EPR 110

6-2 Experimental hyperfine data for BChl *a* and BPheo *a* radical anions. 112

LIST OF FIGURES

Figure page

1-1 *Rb. sphaeroides* reaction center crystal structure 5

1-2 Relative energy levels for the radical pairs in the primary photochemistry in photosynthetic bacteria. 7

1-3 Molecular structures of prokaryotic (bacterial) and eukaryotic (plant) pigments. 9

2-1 The effect of a strong external magnetic field, B_o, on dipole moments in a paramagnetic sample. 11

2-2 Electron spin vector and quantized Zeeman energy states for $S = \frac{1}{2}$ 13

2-3 EPR powder patterns showing rhombic and axial symmetry 19

2-4 Cw-ENDOR population effects on a system with $S=\frac{1}{2}$, $I=\frac{1}{2}$ 20

2-5 Effects of microwave pulses on the spin magnetic moment, **S**, and the net magnetization, **M** 26

2-6 Davies ENDOR pulse sequence 27

2-7 Mims ENDOR pulse sequence 28

2-8 2 pulse and 3 pulse ESEEM sequences 30

3-1 UV-Vis absortion spectrum of purified BChl *a* 33

3-2 UV-Vis absorption spectrum of BPheo *a* 34

3-3 UV-Vis absorption spectra of chlorophyll *a* and *b* 35

3-3 Anaerobic reaction vessel 36

3-4 Transmission cw-EPR block diagram 39

3-5 Quasi-optical superheterodye instrumental setup 40

3-6 Quasi-optical sample holder 41

4-1 X-Band EPR of BChl *a* radical anion 45

4-2 X-Band Mims ENDOR of BChl *a* radical anion 46

4-3 High field EPR spectrum of BChl *a* radical anion 47

4-4 Saturated BChl *a* anion EPR signal with fully resolved g-tensor 48

4-5 High field cw-ENDOR spectrum of BChl *a* radical anion, measured at g = 2.00402 (–7 mT) 49

4-6 High field cw-ENDOR spectrum of BChl *a* radical anion, measured at g = 2.00303 (-2 mT) 50

4-7 High field cw-ENDOR spectrum of BChl *a* radical anion, measured at g = 2.00218 (+2 mT) 50

4-8 Stack plot of BChl *a* radical anion ENDOR spectra 51

4-9 Effective hyperfine splittings for BChl *a* radical anion 52

4-10 Cw-EPR of BPheo *a* radical anion 53

4-11 X-band 3-pulse ESEEM on BPheo *a* radical anion 55

4-12 Fast Fourier transform of the time domain 3-pulse ESEEM data for BPheo *a* radical anion 56

4-13 W-band echo detected field sweep of BPheo *a* radical anion 57

4-14 Davies ENDOR of BPheo *a* radical anion 58

4-15 High field EPR of BPheo *a* radical anion 59

4-16 Saturated EPR absorption of BPheo *a* radical anion 60

4-17 High field cw-ENDOR on BPheo *a* anion, measured at g = 2.00415 (g_x) 61

4-18 High field cw-ENDOR of BPheo *a* anion, measured at g = 2.00338 (g_y) 61

4-19 High field cw-ENDOR of BPheo *a* anion, measured at g = 2.00228 (g_z) 62

4-20 Stack plot of cw-ENDOR spectra on BPheo *a* radical anion 63

4-21 Effective hyperfine splittings for BPheo *a* radical anion 64

4-22 X-band cw-EPR spectrum of BChl *a* radical cation 65

4-23 W-band echo detected field sweep on BChl *a* radical cation 66

4-24 W-band Davies ENDOR on BChl *a* radical cation.. 67

4-25 W-band Mims ENDOR on BChl *a* radical cation 68

4-26 W-band echo detected field sweep of BPheo *a* radical cation................................. 70

4-27 W-band Davies ENDOR of BPheo *a* radical cation 71

4-28 W-band Mims ENDOR of BPheo *a* radical cation.. 71

4-29 X-band cw-EPR spectrum of Chl *a* radical anion.. 73

4-30 High field EPR spectrum of Chl *a* radical anion with
phosphorus standard 74

4-31 X-band cw-EPR of Chl *b* radical anion 75

4-32 High field EPR spectrum of Chl *b* radical anion with
phosphorus standard 76

5-1 Proposed orientation of **g** on the BChl *a* radical anion.. 80

5-2 Spin density plots for BChl *a* radical anion generated with DFT.............................. 82

5-3 Molecular structure and atomic numbering of BChl *a* 84

5-4 ENDOR spectra from the principal g-tensor components
of BChl *a* radical anion.. 87

5-5 Theoretical and experimental isotropic hyperfine couplings
for BChl *a* radical anion 88

5-6 Molecular structure and atomic numbering of BPheo *a* 91

5-7 Spin density plots predicted by DFT for BPheo *a* radical anion 93

5-8 Molecular structure and atomic numbering of BPheo *a*. 94

5-8 High field ENDOR spectra of BPheo *a* radical anion 97

5-9 Spatial spin density plots generated with DFT predictions
for BChl *a* radical cation 100

Abstract of Dissertation Presented to the Graduate School
of the University of Florida in Partial Fulfillment of the
Requirements for the Degree of Doctor of Philosophy

ELECTRON MAGNETIC RESONANCE OF CHLOROPHYLLS: RADICAL ANIONS AND CATIONS

By

Lee Matthew Walker

August 2003

Chair: Alex Angerhofer
Major Department: Chemistry

Photosynthesis is the major natural process that provides free energy to the metabolism of plants and photosynthetic bacteria. However, understanding of the primary events in this process is still incomplete. The energy of incident photons is collected and channeled into the membrane spanning reaction center where it is used to initiate an electron transfer. The first ion formed within the bacterial reaction center is a dimer of bacteriochlorophyll *a* molecules, known as the primary donor (D), which becomes cationic upon losing an electron. This electron then begins its journey through the A-branch of the reaction center, which is composed of a bacteriochlorophyll molecule, a bacteriopheophytin molecule, and a ubiquinone molecule. Upon leaving the primary donor, the electron reduces the bacteriochlorophyll *a* (BChl *a*) molecule and then the bacteriopheophytin *a* (BPheo *a*) molecule. The charge separation between the primary donor and the bacteriopheophytin has been generated and studied by others. The role of BChl *a* in this electron transfer remains unclear. In this work, the radical cationic and anionic states of BChl *a* and BPheo *a* were investigated with EPR, ENDOR and ESEEM. Photosynthetic plant pigments, chlorophyll *a* (Chl *a*) and chlorophyll *b* (Chl *b*), were reduced and studied with high field EPR. This work reports the first high field EPR data with fully resolved g-tensors for the radical anions of BChl *a*, BPheo *a*, Chl *a*, and Chl *b*. Also, for the first time, orientationally selected ENDOR was used to measure the proton hyperfine interactions of BChl *a* and BPheo *a* radical anions. These anions show similar trends in their anisotropic hyperfine interactions, but the differences in the Zeeman and hyperfine interactions are discernable at high fields. The orientations and values of the Zeeman and hyperfine tensors have been approximated using spectral fitting procedures and density functional theory predictions. This work marks the first steps toward full characterization of the electronic nature of the primary acceptors in (bacterial and plant) photosynthesis.

CHAPTER 1
PHOTOSYNTHESIS

Photosynthesis is the process used by plants, algae, and photosynthetic bacteria to convert the energy of light into chemical energy. This energy is used in different ways depending on the specific organism. Green plants and algae (eukaryotes) use photosynthesis to consume carbon dioxide and produce oxygen and carbohydrates, while certain bacteria (prokaryotes) consume organic compounds and can adapt to their environment to survive in a variety of conditions. Basically, photosynthesis provides the energy and reduced carbon necessary for life on this planet, as well as the oxygen necessary for the survival of aerobic organisms. The last 200 years have led to great achievements in understanding the basic processes of photosynthesis, yet fundamental uncertainties remain [1-6]. After a brief historical perspective, the structure of the photosynthetic machinery will be discussed and then a closer look will be taken at the chemistry of this process.

The first step toward understanding the process of photosynthesis came in the discovery of oxygen production. In 1780, Joseph Priestly kept a mouse alive through the oxygen production of a sprig of mint [7]. Priestly also showed that a burning candle would go out when under a closed vessel, but the presence of a sprig of mint would allow the candle to burn again after several days. He did not know about molecular oxygen, but he did ultimately claim that plants could "restore air which had been injured by the burning of candles" [8, p. 432]. By the beginning of the 19th century, understanding of photosynthesis was sufficient to develop the basic equation we know today.

$$CO_2 + 2H_2X + h\nu \ = \ (CH_2O) + X_2 + H_2O$$

The energy needed to drive this reaction is supplied by sunlight. The X in this reaction denotes oxygen for plant photosynthesis and sulfur for certain photosynthetic bacteria, such as *Rb. sphaeroides* and *Rps. viridis* [7]. This rather simple equation represents an amazing orchestration of macromolecules and proteins, which carry out a very efficient conversion of solar energy to chemical energy. In 1845, Julius Robert von Mayer proposed that photosynthetic organisms convert light energy into chemical free energy [8]. The magnitude of Mayer's statement is still being realized today, since the fine details of this energy conversion process are still not fully understood. In the 1930's, Gaffron and Wohl postulated that incident light is absorbed by antenna chlorophyll molecules to produce an exciton, which migrates to a more stable photochemical trapping chlorophyll molecule, which is part of the integral photosynthetic unit: the reaction center [9]. It was not until the 1980's that the structures of bacterial reaction centers were solved [6,10-13], and it was 2000 before plant photosystem crystal structures were solved [14,15]. Solving the structure of the reaction center provided a spatial reference of the components involved in the energy conversion, which allowed research to focus on the energetics and electronic structure.

In 1956, Commoner et al. measured a radical species with EPR generated from photo-oxidized chloroplasts [16]. The nature of this ionic species would be debated for years, until it was identified as a chlorophyll cation radical [17,18-21,22-25]. In the early 1970's, this species was further identified as a dimer of bacteriochlorophyll molecules in bacterial reaction centers through EPR and ENDOR studies [26-29,30-32], as well as through X-ray crystallography [6,33]. Further magnetic resonance studies have examined the electronic structure of this dimer to estimate the properties and location of the electron density [34,35].

Energy Conversion

Photosynthesis can be divided into three separate but complementary processes: collection of incident light and transfer of this light energy to special trans-membrane complexes known as reaction centers, charge separation within the reaction center through electron transfer, and protonation of electron acceptors and establishment of a proton gradient [36]. The work presented here will focus on the charge separation and electron transfer pathway. To appreciate the pathway of the electron transfer reactions, the structure of the photochemical machinery must be understood.

Solar energy enters the reaction center through a pair of chlorophyll molecules known as the special pair or the primary donor. The primary donor (D) uses this excess energy to initiate an electron transfer within a chain of cofactor molecules, which comprise the heart of the reaction center (RC). This RC complex is composed of cofactor molecules and proteins, which perform an efficient electron transfer through the stromal (for green plants) or cytoplasmic (for bacteria) membrane. Electron transfer reactions occur between the primary donor and intermediate acceptor molecules, creating charge separated pairs between the primary donor and each consecutive intermediate acceptor. The ultimate charge separation is equalized by a proton gradient to drive the production of ATP. This series of oxidative and reductive steps is heavily driven by the redox potential and molecular orbital overlap of each consecutive cofactor. Although the mechanism of the photosynthetic process differs between green plants and bacteria, the efficient conversion of light into chemical energy is similar. Photosynthetic bacteria contain only one type of reaction center, while green plants have two: photosystem I and photosystem II [37]. These photosystems work in series with photosystem I being the primary energy source for the plant while photosystem II is mainly responsible for producing oxygen and splitting water [37]. Since photosystem I has a strong optical absorbance at $\lambda \sim 700$ nm, and photosystem II requires light of $\lambda \leq 680$ nm, the primary donor molecule that initiates the electron transfer within each photosystem is termed P_{700} and P_{680}, respectively. Bacterial primary donors are labeled similarly as P_{865} for *Rhodobacter sphaeroides* and P_{960} for *Rhodopseudomonas viridis*. Bacterial reaction centers build the primary donor from bacteriochlorophyll *a* and *b* molecules for *Rb. sphaeroides* and *Rps. viridis*, respectively. These chlorophyll molecules are photochemical traps for the excess energy of the light harvesting system. The energy conversion in the reaction center entails the absorption of one photon, which results in a near unity quantum yield [6]. This efficiency also applies to photosynthetic bacteria, which seem to have certain structural and functional similarities to photosystem II [38,39]. The crystal structure of plant photosystems has just recently been solved [14,15,37], which makes it advantageous to turn to certain non-sulfur bacterial reaction centers whose reaction center structures are known to high resolution, such as *Rb. sphaeroides* [13] and *Rps. viridis* [6,10-12,40].

The Bacterial Reaction Center

The bacterial reaction center is composed of a protein scaffolding and cofactor molecules which perform the chemistry of the energy conversion. The cofactor components of the reaction center are: a bacteriochlorophyll dimer, two bacteriochlorophyll monomers, two bacteriopheophytin molecules, two quinone

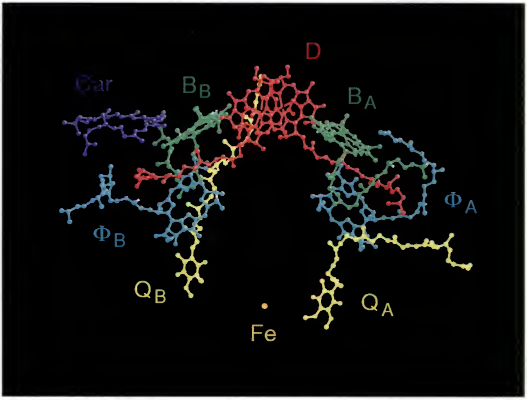

Figure 1-1 *Rb. sphaeroides* reaction center crystal structure [41] consisting of a primary donor (D), a carotenoid (Car), two accessory bacteriochlorophyll molecules (B), two bacteriopheophytin molecules (Φ), two ubiquinone molecules (Q), and a non-heme iron (Fe).

molecules, and a non-heme iron atom. Figure 1-1 is a crystal structure image of the bacterial reaction center from *Rb. sphaeroides* [13]. Branches A and B are chemically identical, with the exception of a carotenoid molecule on the B branch which quenches the triplet state on the primary donor ($^3D^*$) [42]. These branches maintain an approximate C_2 symmetry about an axis running between the branches, through the planes of the primary donor and the Fe atom [10,43,44]. Despite structural symmetry in the pigments of the reaction center, the electron transfer occurs asymmetrically, following only the A branch [45,46]. The origins of this behavior have been postulated to result from the alteration of the MO on bacteriopheophytin (Φ_A) by the protein environment [47,48]. The LUMO of Φ_A must overlap with the HOMO of B_A^-, in order for an electron transfer to occur between these two molecules [49]. Electrostatic influences, such as polar protein side-chains, are suspected to play a role in the unidirectionality of the electron transfer. Depending on the rotation angle of the acetyl group on ring I, hydrogen bonding interactions can affect the LUMO, which affects the electron transfer [49-51]. Upon receiving the solar energy from the antenna chlorophylls, the primary donor (D) promotes an electron within the singlet manifold to the first excited state. Upon leaving the primary donor, the electron density generates an anionic state on a bacteriochlorophyll molecule (B_A), a bacteriopheophytin molecule (Φ_A), and a quinone molecule (Q_A).

This electron transfer creates a charge separated state between D^+ and possibly B_A^- [4,52-59] which very quickly results in the reduction of Φ_A to create D^+— Φ_A^- [53-55,60]. The exact role of B_A in this process is still under discussion. The initial charge separation between D and B_A occurs in about 3ps [61-64]. This charge separated state, D^+— B_A^-, state decays in less than 1 ps to generate, D^+— Φ_A^- [53,54,65,66]. The electron transfer then proceeds to Q_A in about 200 ps [6,41]. The rate of these reactions indicates the efficiency of this process, but introduces an element of difficulty in the study of this process. Figure 1-2 illustrates the relative energies of the various ionic species involved in the electron transfer process. The approach of this work will be to isolate various ionic species to study the electronic properties of the individual radicals, which dictates the chemistry of this electron transfer process.

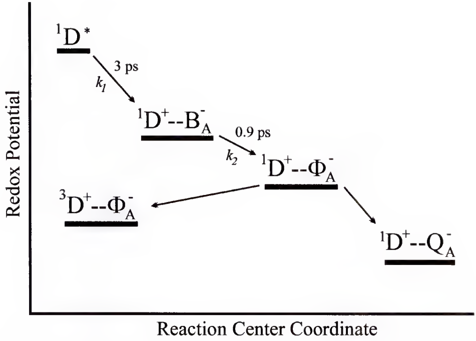

Figure 1-2 Relative energy levels for the radical pairs in the primary photochemistry in photosynthetic bacteria. Relative energies are not to scale.

Ionic Cofactors

The reaction center cofactors have slight molecular variations, which are specific to the organism in which they are found. *Rb. sphaeroides* is composed of *a*-type bacteriochlorin pigments, *Rps. viridis* is composed of *b*-type bacteriochlorin pigments, and eukaryotic reaction centers are composed of *a*-type and *b*-type chlorin pigments (shown in Figure 1-3). The main chemical difference between prokaryotic (bacteriochlorin) and eukaryotic (chlorin) pigments lies in the extent of saturation on the tetrapyrrole [67]. Bacteriochlorin molecules have two saturated pyrrole rings (rings II and IV), while chlorin molecules have one reduced pyrrole ring (ring IV). This difference reduces the extent of conjugation on the plant pigments, which increases the oxidation and reduction potential for the plant species, relative to bacterial pigments. Within the reaction centers, the protein environment influences the redox behavior as well, but the nature of the individual species will be the focus here. According to Marcus theory, the rate and efficiency of the radical pairing depend on the extent of molecular orbital (MO) overlap, the difference in redox energy, and the reorganization energy [68]. The cationic state serves as a direct probe of the highest occupied molecular orbital (HOMO), while the anionic state probes the lowest unoccupied molecular orbital (LUMO). Hence, the intermediate acceptor radical cation and anion species have been isolated from the reaction center and studied with electron magnetic resonance (EMR). In this way, the frontier orbitals may be studied, which are responsible for the electron transfer pathway.

The recent crystallization of photosystems I and II have identified the cofactors responsible for the primary charge separation in higher plants [14]. The apparent versatility of chlorophyll *a* in these photosystems prompted the study of this species. Chl *a* seems to be a plant analogue to BChl *a* in bacterial reaction centers. The absence of chlorophyll *b* in the photosystems generated curiosity, and applied magnetic resonance to probe any differences in electronic structure between these anions.

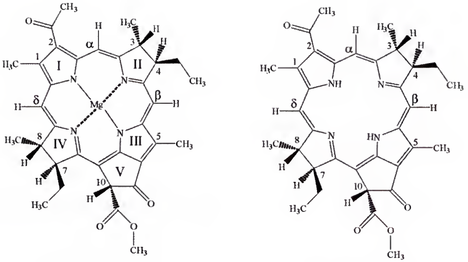

Bacteriochlorophyll *a* Bacteriopheophytin *a*

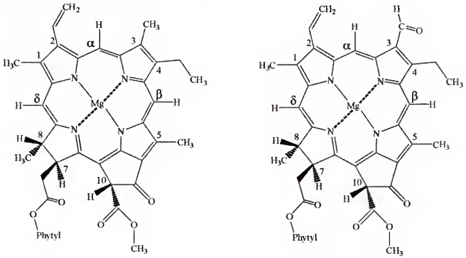

Chlorophyll *a* Chlorophyll *b*

Figure 1-3 Molecular structures of prokaryotic (bacterial) and eukaryotic (plant) pigments.

CHAPTER 2
MAGNETIC RESONANCE THEORY

Magnetic resonance spectroscopy is a technique that uses an external magnetic field to lift the degeneracy of spatial quantization among the dipoles in the sample. Nuclear Magnetic Resonance (NMR) is a popular technique, which probes the nuclear magnetic moments of a system, while Electron Magnetic Resonance (EMR), also known as Electron Spin Resonance (ESR) or Electron Paramagnetic Resonance (EPR), probes the electronic dipole moments of a system. Since the EMR performed in this work, studies paramagnetic radical ions, the expression EPR will be applied from now on. Certain nuclei are magnetic, and thus, can be investigated using NMR. Magnetic nuclei are commonly found in organic molecules, such as hydrogen and nitrogen, which gives NMR a certain utility among synthetic organic chemists. All electrons on the other hand, possess a magnetic moment. The interaction of these nuclear and electronic moments contributes to the utility of EPR. Electrons occupy orbitals, which are filled according to Hund's rules. These rules require electron pairing within orbital sublevels, which leads to a cancellation of the total spin. If at least one electron remains unpaired, the molecule is paramagnetic and may be investigated with EPR to study molecular structure and geometry, inter-molecular interactions, and molecular orbital energy level behavior. The main focus here will be the application of EPR to photosynthetic pigment ions to determine structural information and predict chemistry of the various ionic species involved in the primary charge separation of bacterial and plant reaction centers. A variety of EPR experiments were used to investigate these systems, such as, Electron

Spin Echo Envelope Modulation (ESEEM), high field cw-EPR, and Electron Nuclear DOuble Resonance (ENDOR). An introduction to EPR will be limited but a myriad of texts exists for further background information [69-71].

Magnetic Moments and Angular Momenta

Electrons are magnetic particles that will interact with an externally applied magnetic field. Classical physics predicts the moment will precess about an externally applied magnetic field with a certain angular velocity. This classical picture would allow the moment to maintain any arbitrary angle with the external field during its precession. In the quantum picture, however, the angle between the moment and the external field, B_o, is quantized, which only allows space-quantized values of angular momentum. Since the electron's magnetic moment and angular momentum are directly related to the energy, this quantization of momentum leads to a quantization of energy. Figure 2-1 illustrates the effect of a strong magnetic field on the electronic dipoles within a sample. When B_o is turned on, the electrons align with this field and precess about the axis of B_o

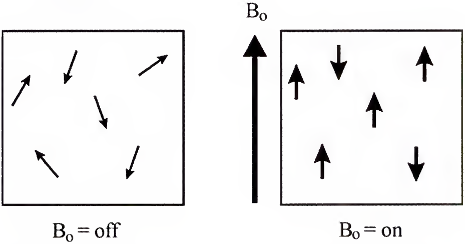

Figure 2-1 The effect of a strong external magnetic field, B_o, on dipole moments in a paramagnetic sample. The vectors in the left frame represent individual dipoles, while the larger vectors in the right frame are net dipoles, resulting from the electronic dipole precession about B_o.

with spatially quantized orientations. The vectors shown on the right of figure 2-1 are actually resultants of each electronic dipole moment's precession about B_o. The arrows parallel to B_o represent dipoles in the lower spin state, while the antiparallel arrows represent dipole moments in the upper energy state. The frequencies of precession will be intimately related to the nature of the electron density on the paramagnetic molecules in the sample. This relationship is described through the electronic Zeeman equation.

$$H_{Zeeman} = \mu_B \cdot g \cdot B_o \cdot S \tag{2.1}$$

$$h\nu = \mu_B \cdot g \cdot B_o \tag{2.2}$$

Equation 2.1 is the Zeeman component of the Hamiltonian equation, where equation 2.2 describes the Zeeman resonance condition, or difference between two electronic Zeeman levels. The left side of this equation is the microwave energy and the right side is the Zeeman energy splitting that is proportional to the external magnetic field. In this equation *h* represents Planck's constant (6.626 x 10^{-34} Js), ν represents the microwave frequency (in Hz), **g** represents the g-tensor, μ_B is the Bohr magneton (9.27402 x 10^{-24} JT^{-1}), **S** is the spin angular momentum, and B_o is the static external magnetic field. When the Zeeman condition is satisfied, an EPR transition occurs, as shown in figure 2-2. The selection rule limits transitions to $\Delta M_S = \pm 1$, which explains why **S** does not appear in equation 2.2.

Electrons possess two forms of angular momentum: orbital and spin. Thus, the total angular momentum is given as the sum of the orbital and spin components. Orbital angular momentum (L) can be accounted for quantum mechanically as well as classically. In the classical picture, this quantity results from the electron's motion within the orbitals of the molecule. This motion generates a magnetic field, which alters the

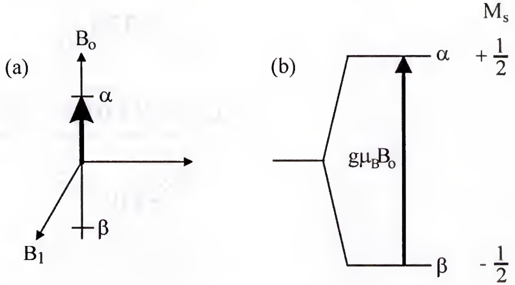

Figure 2-2 (a) Net spin vector (which has a resulting dipole in the opposite direction) and (b) energy level scheme for S = ½ system, having two allowed energy states.

magnetic field felt by neighboring molecules in the sample. Spin angular momentum (S), on the other hand, is purely a relativistic quantum property that has been detected experimentally. The coupling of the spin (S) and orbital (L) angular momenta is measured by the value of a sample's g-tensor. All the species to be dealt with here have one unpaired electron, S= ½, that is delocalized over the conjugated π-system on the molecule, which has relatively weak spin-orbit interactions leading to $g \approx 2$. Spin angular momentum can also interact with neighboring dipoles--nuclear (I) or electronic (S)--which changes the local field felt by the electron spin. This dipolar interaction is known as hyperfine (I-S) or fine structure (S-S) interactions and will be discussed after EPR.

cw-EPR

An EPR experiment may be performed in one of two ways, continuous wave (cw) or pulsed. In the continuous wave experiment the sample is continuously irradiated with microwaves of a fixed frequency. The magnetic component of this radiation, B_1, interacts with the electronic magnetic moments of the sample while the static field, B_o, is swept through the resonance condition described by equation 2.2. Figure 2-2 illustrates the behavior of the net spin magnetization vector in the presence of the magnetic components of the external static field, B_o, and the microwave radiation, B_1. When the frequency of the incident microwave radiation and the static field satisfy the resonance condition, radiation is absorbed by the sample. This radiation is absorbed by the spins that are “flipped” from the lower energy state to a higher energy state. That is, when the resonance condition is satisfied a portion of the spin population is promoted from a lower energy state to a higher energy state, which reduces the population of the lower level and increases the population of the upper level. The relative populations of these energy states determine the intensity of the microwave absorption. If the upper state’s population approaches the population of the lower state, saturation effects distort the EPR signal and can reduce its intensity. The number and splitting of these energy levels depend on the number and nature (orbital location) of the unpaired electron(s), and on the magnetic nuclei interacting with the electron density. These electronic energy states may interact with neighboring magnetic nuclei to produce hyperfine splitting of the electronic Zeeman states.

g-Tensor

The g-tensor is the proportionality constant that represents the Zeeman levels’ deviation from a true spin system. This quantity can be single valued (isotropic), or can be anisotropic due to anisotropic spin-orbit interactions and mixing of the ground state with excited states. The g-tensor can be a very useful parameter for identifying molecules, determining geometrical molecular structure, or assessing interactions between a radical and its environment [33,72-75]. The interaction of ground and excited electronic states also influence this parameter. The g-value for a "free" electron, which is free of orbital interaction, is known very accurately to be: 2.002319304386(20) [76]. Organic free radicals maintain isotropic g-values close to the free electron value. However, interaction with excited states and spin-orbit coupling introduce slight anisotropy in the g-tensor, but this anisotropy is usually on the order of 10^{-3}, which is relatively small. Equation 2.3 shows the relationship between the g-value and the free electron:

$$g_{mn} = g_e \delta_{mn} + 2\lambda \sum_{n} \frac{\langle 0 \mid L_m \mid n \rangle \langle n \mid L_n \mid 0 \rangle}{E_n - E_o} \qquad (2.3)$$

This equation results from Rayleigh-Schroedinger perturbation treatment of the spin Hamiltonian, which represents the individual elements of the g-matrix, and their dependence on the orbital functions of the excited states, n. The resulting g-value, g_{mn} is equal to the free electron g-value, g_e, unless orbital angular momentum is obtained from n excited states, which is represented by the summation of excitations to higher states. The denominator of the mixing term is the energy difference between the excited state, E_n and the ground state, E_o. The spin-orbit coupling constant, λ, is unique to individual nuclei.

Initially proposed by Stone [77] and modified by Pryce [78], it was determined that the component of the g-tensor normal to the plane of conjugation experiences minimal spin-orbit coupling, and thus, falls closest to the free electron value. Anisotropic Zeeman interaction gives rise to the characteristic powder pattern shown in figure 2-3. The theory of this interaction has been further developed for conjugated, doublet π-radicals to characterize molecular structure [41,75,79-81] and intermolecular interactions [74,81-83]. Advances in high magnetic field technology have turned the focus of much research to better understanding this parameter. In doublet radicals with few heavy atoms and a largely (spatially) delocalized electronic wavefunction, the g-tensor is usually too isotropic to detect with conventional, X-band (9.5 GHz) experiments, showing anisotropy on the order of 10^{-4}. Often, frequencies of at least 200 GHz are required to obtain full resolution in **g**. The principal components of the g-tensor can be measured if the anisotropy in the Zeeman interaction exceeds the unresolved hyperfine (nuclear) interaction. The g-tensor can be theoretically predicted as a function of spin-orbit interactions and electronic Zeeman interactions, with relativistic mass and gauge corrections [75,79]. The interaction of the electronic spin density with the magnetic field generated by the electron's orbital motion gives rise to spin-orbit interactions. This parameter will be discussed further in the following section.

Hyperfine Interaction

Hyperfine interaction is expressed in the Hamiltonian as the sum of the products of the spin moment vector, **S**, the hyperfine coupling constant, $\mathbf{A}_i$, and the nuclear moment vector, $\mathbf{I}_i$, as shown in the following equation.

$$H_{hfi} = \sum_i \mathbf{S} \cdot \mathbf{A}_i \cdot \mathbf{I}_i \tag{2.4}$$

This summation is evaluated over all nuclei, *i*, and represents the hyperfine interaction between an unpaired electron and magnetic nuclei. This interaction is independent of field; however, the nuclear Zeeman interaction is field dependent. In solution, the hyperfine interaction becomes isotropic due to the averaging effect of molecular motion. In the disordered solid phase, such as frozen solution, the anisotropic hyperfine interaction on large molecules with many weak nuclear interactions, such as chlorophylls, produce such weak coupling that the EPR spectral line becomes broadened by this effect. Chlorophylls possess approximately 6 alpha, 15 beta, and 8 gamma protons, as well as 4 nitrogen atoms that can contribute to the hyperfine interaction (see figure 1-3). Since the electron density is delocalized over the π system of about 20 carbon atoms, the spin density on each atom is relatively small, leading to relatively small hyperfine couplings from the aforementioned nuclei. In addition, the coupled nuclei are not symmetry related, and thus maintain slightly different hyperfine coupling constants. So, the number and diversity of hyperfine interactions, in addition to the small **g**-anisotropy, lead to an unresolved EPR line at X-band with a linewidth ~12-18 G. This lack of resolution prevents accurate g-tensor measurements and must be overcome with higher fields. Even though H_{hfi} is independent of the external field, B_o, another term in the Hamiltonian must be considered. Consider the entire Hamiltonian for this system:

$$\begin{aligned} H &= H_{Zeeman} + H_{NuclearZeeman} + H_{hfi} \\ H &= \mu_B \mathbf{g} \cdot \mathrm{B_o} \cdot \mathbf{S} - \sum_i \mu_N \mathrm{B_o} \cdot \mathbf{g}_N \cdot \mathbf{I}_i + \sum_i \mathbf{S} \cdot \mathbf{A}_i \cdot \mathbf{I}_i \end{aligned} \tag{2.5}$$

If the g-tensor is not fully resolved, the inhomogeneous EPR linewidth ($\Delta B_{1/2}$) must be dominated by field independent factors, such as H_{hfi}. By increasing B_o, the H_{Zeeman} term and the $H_{NuclearZeeman}$ term will eventually overcome the H_{hfi} term, allowing for full resolution in **g**. The magnitude of the field required to fully resolve **g** depends on the anisotropy of the g-tensor as well as the magnitude of the hyperfine interaction. For a given hyperfine interaction, the field required to resolve the g-tensor components decreases as the g-anisotropy increases. Similarly, if the g-anisotropy is very small, the external field required for full resolution will be large. The experimental aspects of high field experiments have been thoroughly reviewed by others [5] and will only be highlighted here.

The spectral separation (ΔB) in g-values, g_1 and g_2, is given by equation 2.6.

$$\Delta B = \frac{h\nu}{\mu_B}\left(\frac{1}{g_1} - \frac{1}{g_2}\right) \tag{2.6}$$

The ability to resolve the g-tensor components is enhanced by a factor of 40 when increasing the microwave frequency from 9.5 GHz to 330 GHz. G-tensor resolution is determined by the magnitude of the anisotropic hyperfine interactions. The magnetic nuclei, consisting mainly of protons and nitrogens in photosynthetic pigments, can interact with the magnetic moment of the electron density. This interaction splits the electronic Zeeman energy levels into hyperfine levels. The transitions between these levels can be partially resolved in solution state EPR since the molecular tumbling averages out the anisotropic interaction. If the linewidth of the anisotropic hyperfine interaction exceeds the splitting between the g-tensor components, then the g-tensor is not resolved and higher fields must be employed.

$$B\frac{\Delta g}{g_{iso}} > \Delta B_{1/2}^{hfi} \tag{2.7}$$

Equation 2.7 expresses the "high field" condition, which occurs when the anisotropic Zeeman interaction exceeds the linewidth of the unresolved hyperfine interactions. The electron density occupies the molecular orbitals that participate in the π-conjugation. This MO has a similar orientation on each paramagnetic molecule in the sample. In randomly oriented samples, such as a frozen solution, the molecular axes are distributed over all possible orientations with respect to the external field axis. Equation 2.8 illustrates the spatial relationship between the effective g-value, $g(\theta,\phi)$ and the external magnetic field:

$$g(\theta,\varphi) = \sqrt{(g_1\cos\varphi\sin\theta)^2 + (g_2\sin\varphi\sin\theta)^2 + (g_3\cos\theta)^2} \tag{2.8}$$

This angular distribution creates a characteristic EPR spectrum known as a powder pattern [63]. Figure 2-3 contains two possible shapes for the g-tensor to adopt. A rhombic geometry has three unequal diagonal elements in the tensor, $g_{xx} > g_{yy} > g_{zz}$, while an axial geometry resembles a cylindrical shape with two equal diagonal elements, $g_{xx} = g_{yy} > g_{zz}$. The edges of these absorption spectra result from distinct sets of molecules with a single orientation relative to the external field. That is, only molecules with the x-axis of their g-tensor parallel to B_o absorb at the g_{xx} point of the spectrum. This condition applies to the high field side of the spectrum, where molecules with g_{zz} parallel to B_o are in resonance. Full resolution of the g-tensor is a goal of this work and has important implications that will be addressed when high field ENDOR is discussed.

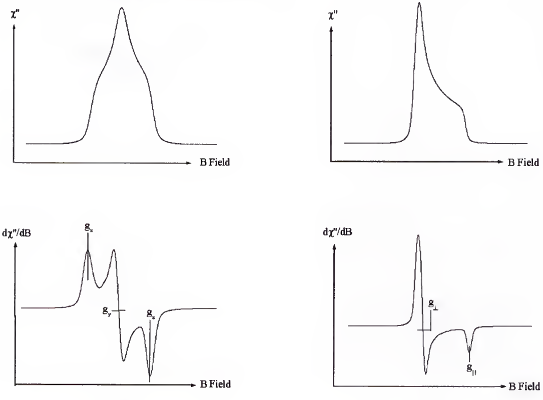

(a) (b)

Figure 2-3 EPR powder patterns showing (a) rhombic ($g_x > g_y > g_z$) and (b) axial symmetry ($g_\perp > g_\parallel$).

cw-ENDOR

Electron Nuclear DOuble Resonance (ENDOR) was experimentally discovered by George Feher in 1959 [84]. This experiment monitors the intensity of an EPR transition while stimulating NMR transitions, so it is basically: EPR detected NMR. If hyperfine coupling exists, the EPR signal intensity will be affected by the NMR transitions. This experiment saturates the EPR transition, then sweeps radiofrequency radiation to induce NMR transitions. If the nuclei experiencing NMR are coupled to the electron density, the intensity of the EPR absorption will change as a function of RF frequency. Figure 2-4 depicts an S=½ system coupled to a proton, I=½, demonstrating the theory of cw-ENDOR. The Boltzman population is disturbed by microwave radiation intense enough to saturate (equalize) the populations in the upper and lower states. Since the intensity of the EPR transition is proportional to the difference in populations

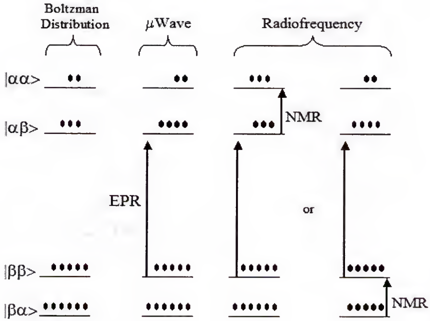

Figure 2-4 cw-ENDOR population effects on a system with S=½, I=½ at thermal equilibrium, with relative spin population depicted as dots.

between the states, any change in the populations between the energy states involved in the transition will affect the intensity of the EPR signal. Hence, when NMR is achieved, spins are taken out of the upper level (or pumped into the lower level) to enhance the population difference between EPR levels.

ENDOR experiments can shed light on the identity of coupled nuclei, number of coupled nuclei, and amount of spin density present at each coupled nucleus. In a powder, or frozen solution, the system is randomly oriented and the ENDOR resonance lines are broadened by the different orientations between the hyperfine tensors, A-tensors, of the individual nuclei and the external magnetic field. Increasing the resolution of the g-tensor can increase the resolution in the ENDOR spectra with orientational selection. This technique performs ENDOR experiments at the turning points in the powder pattern. Each turning point, corresponds to the radicals in the sample with one of their g-axes parallel to the external magnetic field. Thus, an ENDOR experiment performed at g_x in figure 2-3, will probe those species in the sample with g_x parallel to B_o. This effect creates a crystal-like order in the sample at the edges, g_x and g_z, with an average of the various orientations present between the extremes of the powder spectrum. If the hyperfine coupling is weak, i.e. less than the Larmor frequency, the ENDOR spectrum is centered around the nuclear Larmor frequency of the coupled nucleus, with ENDOR lines split with values equal to the hyperfine coupling constant, *A*.

$$\nu_{RF} = \left| \nu_H \pm \frac{A}{2} \right| \tag{2.9}$$

Equation 2.9 illustrates the relationship between the frequency of the external RF, ν_{RF}, and the proton precessional frequency, ν_H. This equation has been simplified to the isotropic case, where the angle between the external magnetic field vector and the vector connecting the electron and the nucleus is insignificant. So, in equation 2.9, we should think of *A* as the effective hyperfine coupling constant, rather than a component of the A-tensor, or strictly an isotropic value. The details of orientation selection will be discussed further in the following section. These experimental details have been thoroughly described elsewhere and have only been highlighted here [70,71].

Orientational Selection

In the realm of high fields, the distribution of molecular orientations, and hence, g-tensor orientations, are separated such that the orientations may be selected by changing the magnetic field [85,86]. By selecting an orientation, a powder or frozen solution, sample may be studied in a partially ordered, crystalline, way. This work uses orientational selection to perform ENDOR experiments on individual orientations to obtain hyperfine tensor magnitudes and orientations relative to the g-tensor axis system [87-90]. The success of this technique, and its utility toward organic radicals, has been demonstrated in the past [91-93]. The hyperfine coupling tensor, *A*, is a sum of the isotropic and anisotropic interaction between magnetic nuclei and the electron density. The isotropic component of this tensor results from contact interaction, known as Fermi contact interaction, which is generated through bonds and is directly proportional to the spin density on the atom. The anisotropic component of *A* results from dipolar interaction between the field produced by the nucleus and the field generated by the electron density. Equation 2.10 describes the dipolar field, H_d, induced by an electronic dipole at any point in space.

$$H_d = \frac{\mu_e}{r^3} \cdot \left(3\hat{r}\hat{r} - \overline{\overline{E}}\right) = \mu_e \cdot \overline{\overline{A}}_d \qquad (2.10)$$

In this equation, μ_e represents the electron magnetic moment, r is the distance from the electron to the nucleus, $\hat{r}$ is a unit vector connecting the electron and the nucleus, and $\overline{\overline{E}}$ is the unit dyadic. Thus, in frequency units, the hyperfine coupling, A_{ij}, can be expressed including the dipolar and isotropic contributions.

$$A_{ij} = -\frac{\beta_e g_e \beta_N}{hr^3} g_i \left(3r_i r_j - \delta_{ij}\right) + A_{iso}\delta_{ij} \qquad (2.11)$$

The first term on the right side of equation 2.11 is the dipolar contribution, A_d, with the second term obviously equal to the isotropic contribution, A_{iso}, which is non-zero on the diagonal elements of the tensor. The three spatial components of A lead to the total hyperfine interaction tensor, shown in equation 2.12.

$$A_{ij} = \begin{vmatrix} A_{d_{11}} + A_{iso} & A_{d_{12}} & A_{d_{13}} \\ A_{d_{21}} & A_{d_{22}} + A_{iso} & A_{d_{23}} \\ A_{d_{31}} & A_{d_{32}} & A_{d_{33}} + A_{iso} \end{vmatrix} \qquad (2.12)$$

Since an ENDOR experiment is primarily a nuclear magnetic resonance experiment, the total magnetic field at the nucleus must be known in order to predict the transition frequencies. The nuclear energy levels result from the nuclear Zeeman interaction, which get perturbed by the hyperfine interaction with the electronic moment and are dependent on the effective field direction. With these relationships accounted for, an expression for the frequency of expected ENDOR transitions can be written as equation 2.13 [86].

$$\nu(\vec{H}, m_s) = \left[\sum_{i=1}^{3} \left[\frac{m_s}{g(\theta,\phi)} \left(\sum_{j=1}^{3} g_j h_j A_{ji} \right) - h_i \nu_o \right]^2 \right]^{1/2} \qquad (2.13)$$

Equation 2.13 gives the resonant frequency of a nucleus having known coordinates as a function of the magnetic field direction $[h_1, h_2, h_3]$ and magnitude. In this equation, $\vec{H}$ represents the dipolar field induced by the electron at any point in space. Equation 2.13

shows that, contrary to equation 2.8, the nuclear frequencies are dependent on the electronic g-value and that the ENDOR transitions are not necessarily symmetric about the nuclear Larmor frequency. The hyperfine coupling expression can be simplified by assuming that the electron and nuclear moments are quantized along the direction of the applied external field, and that the spin-orbit interactions have a negligible effect on the g-value. Equation 2.14 results from these assumptions [86]:

$$A = \frac{g_N \beta_N g_e \beta_e}{r^3}(3\cos^2\theta - 1) + A_{iso} \qquad (2.14)$$

This equation relates the effective hyperfine splitting to the dipolar and isotropic hyperfine couplings for any dipolar angle, θ.

Pulsed EPR

Pulsed experiments have many functions, but in this work they have been used to identify nuclei in the sample. These experiments hold the B_o field constant while varying the power of the magnetic component of the microwave radiation, B_1. Figure 2-5 illustrates the effect of microwave pulses on the net spin vector, **S**. The resultant of this vector's motion is the bulk magnetization, **M**. This bulk magnetization can be composed of many different groups of electron spins, called spin packets. Each packet represents magnetic moments under a slightly different magnetic environment within the sample. Figure 2-5(a) depicts the motion of a spin moment in the presence of an external magnetic field. The resulting vector component of this moment is **M**, shown in figure 2-5(b). Frame (c) demonstrates the effect of a 90^o microwave pulse on the net magnetization. Frames (d) through (f), adopt the rotating frame point of reference. Since the net spin vector, **M**, is precessing about B_o, we can simplify the picture by leaving the laboratory frame and jumping on the x- or y-axis of the precessing frame. Upon application of a microwave pulse, B_1, perpendicular to B_o, **M** undergoes changes in orientation relative to B_o. The actual displacement angle is determined by the length and the power of the pulse, and is known as the Rabi angle.

$$\Omega = 2\pi(\tau)(\nu_r) \tag{2.15}$$

In equation 2.15, Ω, is the Rabi angle, τ is the length of the microwave pulse, and ν_r is the Rabi frequency. The Rabi frequency is given by:

$$\nu_r = \sqrt{\nu_1^2 + (\nu - \nu_B)^2} \tag{2.16}$$

The frequency of the microwave field B_1 is given by ν_1, and at resonance, $\nu = \nu_B$. Once displaced through Ω, the spin packets will dephase as a result of inhomogeneities in the effective magnetic field (figure 2-5(d)). This dephasing time is called T_2 or the transverse relaxation time and is inversely related to the strength of the spin-spin coupling. This dephasing, or relaxation, can result from homogeneous or inhomogeneous effects. Homogeneous relaxation occurs when the magnetic field is the same throughout the excited spins. Inhomogeneous relaxation occurs when the magnetic field felt by the spins varies throughout the sample. This inhomogeneity can result from an inhomogeneous external field, unresolved hyperfine structure, anisotropic hyperfine and Zeeman interactions, and dipolar interactions [69]. These effects alter the effective magnetic field felt by the individual spins, affecting their interaction with the external radiation. This dephasing can be reversed by refocusing the spin packets with a 180° pulse. The refocusing of the spin packets generates a spin echo (Figure 2-5(e)). This effect was first discovered by Hahn, who used a 90° pulse, followed by a 180° pulse [85]. Hahn echos are created with two pulses, but echos can be induced with many pulses, as long as the magnetization gets refocused in the xy plane. As long as the net

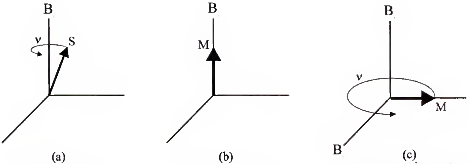

(a)
Spin Precession

(b)
Net Magnetization

(c)
Effect of 90° B Pulse

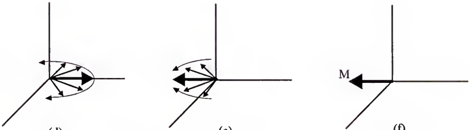

(d)
Spin Dephasing

(e)
Spin Refocussing

(f)
Spin Echo

Figure 2-5 Effects of microwave pulses on (a) the spin magnetic moment, **S**, and (b-f) the net magnetization, **M**. The spins are depicted in the laboratory (stationary) frame in (a) through (c). (d) through (f) assume the rotating frame of reference where point of view follows the precession of the magnetization.

magnetization, **M**, lies in the xy plane, the echo will be detected. The spin packets will relax to their equilibrium orientation, $\theta = 0$, with time constant, T_1. Different pulse sequences can be used to determine T_2 and T_1, which are used to optimize the parameters for pulsed ENDOR and ESEEM experiments.

Pulsed ENDOR

Pulsed ENDOR experiments allow the detection of NMR through the intensity of the electron spin echo. One advantage over cw-ENDOR is the detection of the ENDOR effect in the absence of all incident radiation. That is, the microwave and RF fields are turned off during the detection. Pulsed ENDOR experiments manipulate the spin packets with microwave pulses, then measure the affect of an RF pulse on the bulk magnetization. Davies [94] and Mims [95] developed two variations on the pulsed ENDOR experiment.

Davies ENDOR applies a selective, saturating microwave pulse, stimulates NMR transitions with an RF pulse, then refocuses the resulting magnetization with a Hahn echo sequence. The pulse sequence for Davies ENDOR is shown in figure 2-6. The first 180° pulse fully inverts the spin population of one of the EPR transitions, such that the bulk magnetization is inverted along B_o. This pulse saturates a portion of the inhomogeneously broadened EPR line. This "hole" in the EPR line is then filled in as NMR transitions are induced. The NMR transition moves spin population back into the hole created by the saturating microwave pulse. So, Davies ENDOR detects the restoration of spin echo intensity as a function of RF frequency. The bandwidth of the initial microwave pulse should be much less than the hyperfine coupling constant, as shown in equation 2.17.

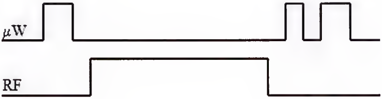

Figure 2-6 Davies ENDOR pulse sequence. A saturating microwave π pulse is followed by a π RF pulse, then a Hahn echo sequence, π/2 – π, refocuses the magnetization. The intensity of the spin echo generated will change if nuclear transitions are induced by the RF pulse.

$$\Delta \nu = \frac{2\pi}{t_{\mu w}} << a_{iso} \tag{2.17}$$

In this equation, Δν represents the bandwidth of the initial microwave pulse, $t_{\mu w}$ represents the duration of the initial microwave pulse, and a_{iso} is the isotropic hyperfine coupling constant. If the range of frequencies in the pulse is too large, on the order of a_{iso}, then the range of spin packets affected by the microwave pulse may overlap with the hyperfine levels, diminishing the ENDOR effect, since the levels that fill in the hole will be saturated as well.

Mims ENDOR applies a series of three non-selective 90° pulses with the second and third microwave pulses separated by an RF pulse (see figure 2-7). The first two microwave pulses create a grated polarization pattern between the electron spins, S_z, and the two-spin order terms, S_zI_z. If an RF pulse induces NMR transitions, the electron spins coupled to those nuclear spins (S_zI_z) will be dephased from the bulk magnetization, thus reducing the intensity of the electron spin echo. This technique is more sensitive to small hyperfine coupling constants ($a < 4$ MHz) but is also known to have “blind spots.” These blind spots result from incomplete refocusing of the bulk magnetization. The application of a $\pi/2$ microwave pulse along the y-axis of the rotating frame affects the bulk magnetization along the x-axis. The remaining, dephased spin packets in the xy-plane are rotated 90° about the y-axis, since the microwave pulses are applied along the y-direction. So, the spin packets on the y-axis are not refocused in the echo, which reduces

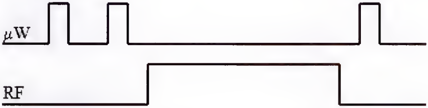

Figure 2-7 Mims ENDOR pulse sequence. Two $\pi/2$ microwave pulses are applied, followed by a π RF pulse, then another $\pi/2$ microwave pulse to refocus the spins. If the RF pulse “flips” any nuclear spins that are coupled to the electron spin, these coupled spin packets will not contribute to the spin echo.

the echo's intensity. The relationship between the pulse separation and the hyperfine interaction is shown in equation 2.18.

$$\tau = \frac{2\pi n}{a_{iso}} \tag{2.18}$$

In this equation, τ represents the time between the first and second microwave pulses, *n* is an integer, and a_{iso} is the isotropic hyperfine coupling constant given in units of 2πHz. Because of the condition shown in equation 2.18, Mims ENDOR data should be taken at various τ values.

ESEEM

Electron Spin Echo Envelope Modulation (ESEEM) was first demonstrated by Rowan et al. in 1965 [96]. Mims also contributed to the theory and experimental techniques for this experiment in 1975 [97]. ESEEM is a valuable technique used to locate interacting nuclei [101] and to measure hyperfine couplings of distant nuclei or nuclei with small nuclear moments. This experiment is essentially a spin echo experiment with a varied pulse separation. This technique capitalizes on the relative strength of the electron and nuclear magnetic moments. Since the nuclear moment is approximately three orders of magnitude smaller than the electron's, the response of these magnetic moments to microwave pulses varies by a few orders of magnitude in the time domain. That is, the microwave pulse reorients the electron's moment much more quickly than the nuclear moment. The effect of this lag time between the moments results in incomplete refocusing of the spin packets, which varies the intensity of the echo. If the microwave pulse interval, T, is divisible by the precessional periods of coupled nuclei, the intensity of the spin echo will be enhanced. The ESEEM effect can be observed with two microwave pulses, but stimulated (three pulse) ESEEM provides greater frequency resolution and eliminates hyperfine artifacts that result from phase interference between nuclei [98]. The ESEEM spectrum is a plot of T versus the intensity of the spin echo, where T is the varied pulse separation (see figure 2-8). As T is increased, nuclear couplings modulate the first order decay of the spin echo, which has time constant T_2 for 2-pulse ESEEM and T_1 for 3-pulse ESEEM. The ESEEM effect arises from the magnetic fields generated by coupled magnetic nuclei, which give rise to variation in the precessional frequency of the spin packets. Since the effect of the nuclear field on the electron is a function of the spin state of the electron, the spin packets coupled to nuclei can have a slightly greater precessional frequency (if the nuclear field is additive) or slightly smaller precessional frequency (if the nuclear field is subtractive) than the bulk magnetization. This fragments the magnetization and results in a phase difference between the coupled packets and the non-coupled packets. The interference between the precession of the coupled packets with the bulk magnetization results in a modulation of the echo intensity, which is ESEEM.

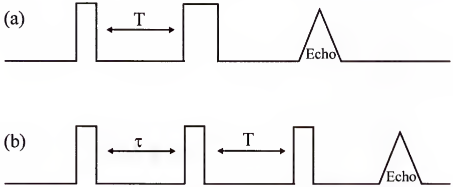

Figure 2-8 (a) 2 pulse and (b) 3 pulse ESEEM sequences. The delay time, T, is increased throughout the experiment and the response of the echo is detected at each T value.

The ESEEM effect can also be explained through the allowance of forbidden transitions. In order to fully explain this phenomenon, the classical picture must be enhanced with quantum effects. Since the microwave pulse covers a range of frequencies that encompass the M_I levels of a given spin sublevel, the wavefunctions become mixed. At small hyperfine couplings, formally forbidden transitions become weakly allowed, such as ($\Delta M_S = \pm 1$, $\Delta M_I = \pm 1$) and can interfere with the allowed ($\Delta M_S = \pm 1$, $\Delta M_I = \pm 0$) transitions. This interference, or branching, modulates the echo intensity with a frequency dependent on the spacing of the nuclear, M_I, sublevels [99,100]. The probability of this branching is determined by the forbidden transitions that become allowed if the non-selective microwave pulse flips the nuclear spin, which creates a two spin order. If branching does not occur, the upper and lower states become coherent and generate a spin echo. The branching then introduces coherent relationships between the upper and lower manifolds, which modulates the echo intensity.

CHAPTER 3
EXPERIMENTAL PROCEDURES

Bacteriochlorophyll *a* Purification

Crude BChl *a* was harvested from the cells of *Rhodobacter sphaeroides* [102]. The contents of the bacterial cells were separated using column chromatography. A powdered sugar column was used for the purification [67,103]. A 41mm Kontes column (K420530-0273) was packed with 16” of powdered sugar (1” ID). The sample (100 mg) was loaded onto the column in a minimal amount of 10% acetone in 1:9 ethyl ether/hexane (v/v). Elution was initiated with 200 mL aliquots of: 1:9 ethyl ether/hexane, 2% acetone in 1:9 ethyl ether/hexane, 3% acetone in 1:9 ethyl ether/hexane, 5% acetone in 1:9 ethyl ether/hexane, and finally 7% acetone in 1:9 ethyl ether/hexane. The eluted species were monitored using thin layer chromatography on silica plates developed in 70:30 hexane/acetone. The column was run in the dark, or in the presence of indirect green light. The BChl *a* fractions were combined, evaporated to dryness using a Buchi Rotovapor R-200 pumped with a Buchi Vac V-500, and stored under argon, in the dark, at –20°C. The fractions were also monitored with UV-Visible Spectroscopy on a Varian Cary 500e Spectrometer. Figure 3-1 contains the UV-Vis spectra, which are in agreement with the expected, published data.

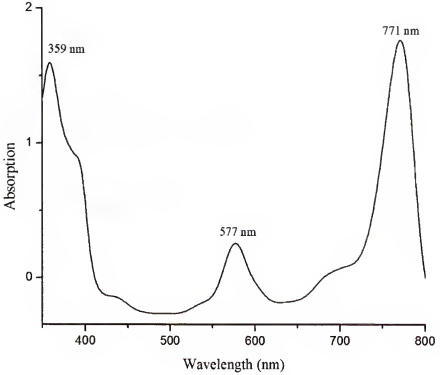

Figure 3-1 UV-Vis spectra of purified BChl *a* in acetone and 1:9 ethyl ether/hexane.

Bacteriopheophytin *a* Generation

BPheo *a* was generated from bacteriochlorophyll *a*. BChl *a* was purified as described in the previous section. Once pure, BPheo *a* was dissolved in glacial acetic acid, which protonates the two nitrogens coordinated to the magnesium atom, hence freeing the magnesium ion from the molecule. The bacteriopheophytin was extracted using a phase separation technique with toluene and water. The bacteriopheophytin goes into the toluene layer, while the magnesium ions and acetic acid are in the aqueous layer. The toluene layer was repeatedly washed with distilled water, and removed from the aqueous portions. The toluene layer was then evaporated under reduced pressure and the product was examined with a Cary 500e UV-Visible Spectrometer, spectrum shown in figure 3-2. An alternative procedure developed by Lotjonen and Hynninen in 1983 [103] can also be used for demetallation.

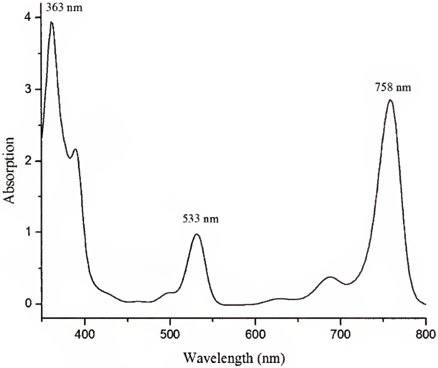

Figure 3-2 UV-Vis absorption spectrum of BPheo *a* in acetone and 1:9 ethyl ether/hexane.

Chlorophylls *a* and *b* -- Extraction and Purification

Plant chlorophylls *a* and *b* were isolated from spinach leaves using a modified dioxane method [104,105]. In the presence of dim green light, 60g of spinach leaves were ground up in a mortar and pestle in the presence of 90mL acetone and 0.30g $NaHPO_4 \cdot 7H_2O$. This leaf mixture was filtered through a coarse Buchner funnel into a 300mL round bottom flask. 60mL dioxane was added, then distilled water was added dropwise until precipitation became visible (~30mL). The flask was placed in the freezer (-20°C) for 45 minutes. The fully precipitated mixture was then centrifuged at 15,000 relative centrifugal force (RCF) for 30 minutes at 5°C using an Eppendorf 5804R centrifuge. The pellet was dissolved in ethanol and evaporated to dryness under reduced pressure. This pellet contains carotenoids, Chl *a* and Chl *b*. These components were separated with column chromatography using a custom made column; 48" tall, 2" ID. This column was packed with 40" of powdered sugar for 80mg of crude leaf extract. The sample was loaded in 10% acetone in 1:9 ethyl ether/hexane. The carotenoids were eluted with hexane and 1:9 ethyl ether/hexane. A solvent gradient was established with 200 mL aliquots, from 1% acetone in 1:9 ethyl ether/hexane to 10% acetone in 1:9 ethyl ether/hexane. Chl *a* was eluted with 3% acetone in 1:9 ethyl ether/hexane, and Chl *b* was eluted with 5% acetone in 1:9 ethyl ether/hexane. This column was run in total darkness and the fractions were monitored with TLC and with a Cary 500e UV-Visible

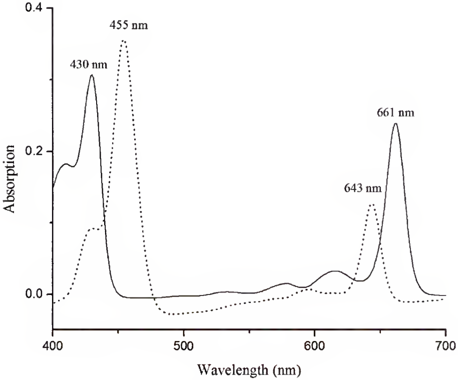

Figure 3-3 Chlorophyll *a* (solid) and *b* (dotted) UV-Vis absorption spectra in 1:9 ether/hexane.

spectrometer (Varian Instruments). The UV-Vis spectra are shown in figure 3-3 for both pigments in 1:9 ether/hexane. The pure components were stored under argon, in the dark, at –20° C.

Radical Anion Generation

Approximately 1-2 mg of the pigment was dissolved in acetone (C_3H_6O) or methylene chloride (CH_2Cl_2) and added to the reaction vessel shown in figure 3-3, which had been dried in a 150°C oven overnight. The solvent was then evaporated under reduced pressure, ~10^4 torr. Potassium was introduced into the vessel in glass capillaries, which were placed in the potassium arm. After repeated flame drying of the entire vessel

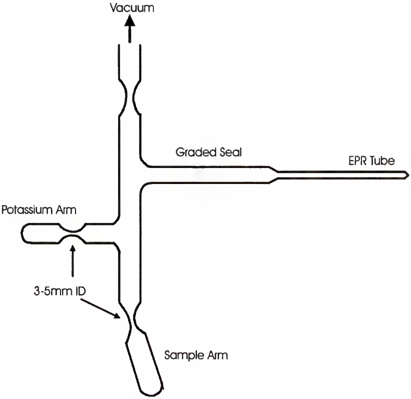

Figure 3-3 Anaerobic reaction vessel made from 10mm borosilicate tubing with 4mm or 5mm quartz EPR tubing and a borosilicate-quartz graded seal. The tapered sections of the vessel facilitate glassblowing under high vacuum.

(with care taken to keep the pigment in the sample arm around 30°C), the potassium arm of the reaction vessel was heated to produce a potassium mirror. This mirror was made several times over several hours, to allow sufficient reaction with any residual water in the system. The tip of the potassium arm was eventually sealed off with a torch to isolate any byproducts from the melting and boiling of the potassium. The solvent was then distilled over from another flask, which contained the freshly distilled and degassed solvent over a sodium mirror. This solvent was attracted to the reaction vessel by submerging the sample arm in liquid nitrogen. The reaction vessel was then sealed off from the vacuum system and once cool, the reduction was achieved by pouring the solution over the mirror. This reaction was monitored with EPR, and once a sufficient concentration of the product was formed, the EPR arm and the sample arm were frozen simultaneously and each sealed off with an O_2/H_2 mixed gas torch.

X-Band EPR/ENDOR

The X-band EPR was done on a Bruker Elexsys e580 pulsed spectrometer. This instrument uses an e580-1010 pulsed microwave bridge with a Gunn microwave source and an Applied Systems Engineering 117x TWT amplifier to generate high powered pulses. The static magnetic field is maintained by a 1.5 T electromagnet. The data was collected and stored on a Silicon Graphics O_2 Workstation, using the supplied Bruker Xepr software. An ENI A-300 Radio Frequency amplifier was used to generate and amplify the RF pulses required for pulsed ENDOR experiments. The cw experiments used a TE_{101} rectangular cavity with an Oxford CF-900 continuous flow cryostat. The pulsed experiments were performed using a Flexline Bruker ENDOR cavity with an Oxford CF-935 helium flow cryostat. Cryogenic temperatures were maintained by an

Oxford ITC 503 Temperature Control Unit, an Oxford GFS-650 Transfer Tube, and an Oxford VC40 Gas Flow Controller.

Transmission High Field cw-EPR

The transmission high field cw-EPR experiments were performed on a home-built setup at NHMFL that has been previously described [98]. This "single pass" setup is depicted in figure 3-4. Microwaves are generated using a 93 GHz Gunn source, which was coupled to a Shottky diode harmonic generator and high-pass filters, which allows operation at frequencies up to 550 GHz. The Gunn source is coupled to a YIG transistor oscillator to lock the frequency. This microwave radiation is sent through oversized, cylindrical, brass waveguides to the sample and then to a liquid helium cooled, QMC In:Sb hot electron bolometer detector (Model QFI/3BI). The absorption of microwaves is measured directly, without a reference arm or a cavity. The sample probe contains a modulation coil that was operated at 1 kHz, with modulation amplitudes between 1 Gauss and 10 Gauss. This instrument is outfitted with an Oxford Instruments Teslatron 17 Tesla, superconducting magnet, which uses a sweep coil for sweeps less than 0.1 Tesla. The EPR signal is monitored with a millimeter Vector Network Analyzer (MVNA), Model MVNA-8-350, for signal processing. The field modulation was generated using a Thurlby & Thandar function generator (Model TG210) which was amplified with a MOS-FET current amplifier (Model X-820HD). The modulation coil covers a 50 mm region of the waveguide and is tightly wound about a G-10 mandrel. Lock-In amplifiers from Stanford Research Systems, Inc. (Model DSP SR830) were also employed to isolate the signal component that follows the modulation frequency. Cryogenic temperatures were achieved through the use of an Oxford Instruments CF-1200 continuous flow cryostat.

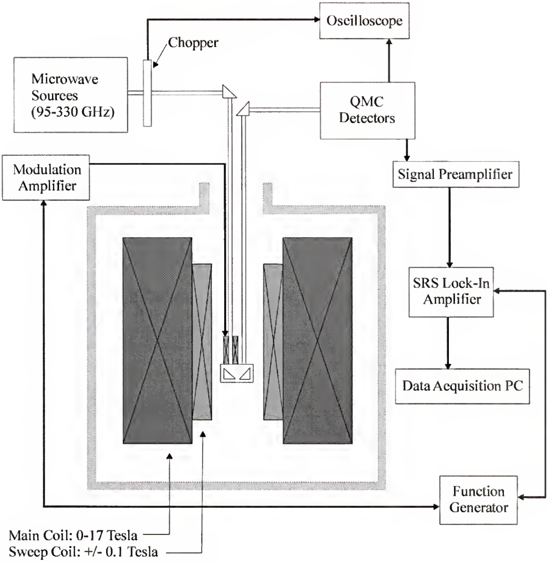

Figure 3-4 Transmission cw-EPR block diagram. Figure adapted from [98].

Quasioptic High Field cw-EPR/ENDOR

The quasi-optic high field EPR and ENDOR experiments were done on a home-built spectrometer at NHMFL [106]. This is a superheterodyne instrument, shown in figure 3-5, uses two Gunn sources (G1 and G2) and two Shottky diode detectors (M1 and M2), mixed with a quasi-optical bridge (dotted region). As the microwaves (from G1) enter the bridge, they are attenuated with a wire-grid polarizer, and a Faraday rotator.

The quasi-optical bridge is composed of elliptical aluminum mirrors that mix and guide the microwaves to a Martin-Pupplet interferometer, which converts the polarization before entering the oversized corrugated, cylindrical waveguide in the sample probe. The microwaves return from the sample, get split into two components by a wire-grid polarizer. The co-polarized beam returns to the circulator and then to the reference Schottky diode (M1), while the cross-polarized component goes to the signal detector (M2). The returning microwaves are mixed with the second Gunn source (G2), operating 6 GHz below the main Gunn, and provides a local oscillator signal for the Shottky diodes. At the sample, a corrugated horn is used to focus the microwaves down to the

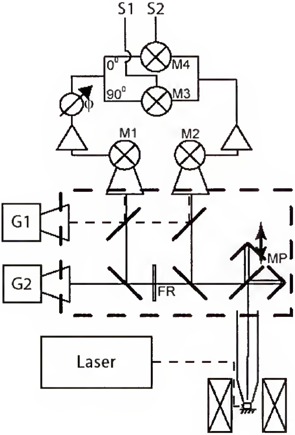

Figure 3-5 Quasi-optical superheterodye instrumental setup [106].

sample holder, which is made of Rexalite, shown in figure 3-6. This sample holder accommodates 5 mm quartz tubes with length, less than 60 mm. This setup allows for cold loading of the sample into the magnet. A modulation coil is fitted beneath the holder, and a 6 turn ENDOR coil is oriented around the sample tube. A Rhode and Schwartz RF source generates the radiofrequency radiation, which is amplified by an Amplified Research RF amplifier.

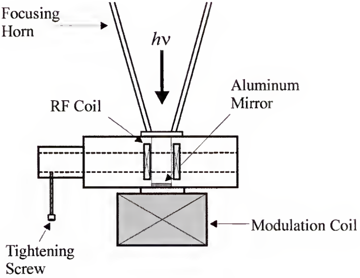

Figure 3-6 Quasi-optical sample holder for frozen liquid samples, for 240 GHz cw-EPR/ENDOR measurements.

Magnetic Field Calibration Procedure

The uncertainty in the magnetic field was reduced through the use of standards with well known Zeeman and hyperfine parameters. The two standards employed in this work were MgO containing 0.05% Mn (I = 5/2) and silicone doped with phosphorus (I = ½). One of these standards was included with the sample in the instrument and the position of the standard's lines provide a guide to correct the field. The gross uncertainty in the field arises from the hysteresis in the current within the sweep coil used to sweep the field during the EPR measurements.

The manganese standard, MgO powder, was incorporated into epoxy, allowed to harden, then cut to fit into the waveguide. The EPR spectrum was measured such that the Mn lines were resolved and intense enough to simulate. The field was corrected by fitting the manganese lines in the experimental data using EPR simulation software, taking the ratio of the experimental g-value to the accepted g-value, then shifting the spectrum by this correction factor. The experimental Mn spectrum was fitted, and the g-value for this fitting, $g(Mn)_{exp}$, was then divided by the accepted value, $g(Mn)_{acc} = 2.00101 \pm 5x10^{-5}$. The ratio of $g(Mn)_{exp}/g(Mn)_{acc}$ gives the correction factor. Once the powder pattern was fitted, using the DOUBLET software, the experimental g-values for the sample were divided by the correction factor. This procedure shifts the g-values, which are linearly proportional to the magnetic field values.

For the bacteriopheophytin *a* radical anion samples, the field calibration procedure was performed using a Si:P standard. This procedure is identical to the Mn field correction. The experimental phosphorus g-value, $g(P)_{exp}$, was determined by fitting the experimental phosphorus lines, which was then compared to the accepted value, $g(P)_{acc}= 1.998525 \pm 5x10^{-5}$. The ratio of these g-values, $g(P)_{exp}/g(P)_{acc}$, gives the correction factor by which the experimental powder pattern g-values were divided. The simulation procedure, which accounts for second order effects, accurately fit the manganese spectrum, which gives an experimental g-value for Mn as well as indicating linearity in the magnetic field throughout the spectrum.

The magnetic field on the Bruker e580 X-band spectrometer was calibrated using the perylene radical cation, which was generated in concentrated sulfuric acid. The accepted g-value for this radical is known to be $g(perylene^{+})_{iso} = 2.002569 \pm 6x10^{-6}$ [69].

The experimental spectrum was fitted using the DOUBLET software, and the ratio of the experimental g-value and the accepted g-value was used as a correction factor to shift the X-band spectra. The experimental g-value was measured to be g(perylene^{+})$_{exp}$ = 2.003877 ± 1x10^{-6}, which corresponds to a shift of -2.20 G.

CHAPTER 4
RESULTS

Bacteriochlorophyll *a* Radical Anion

X-Band (cw and pulsed) and high field (cw) measurements were used to investigate the bacteriochlorophyll *a* radical anion. The X-Band data provide only isotropic g and A-values, which serve as a reference for experiments at higher fields since g and A-tensor data are sought out. The magnitude of the hyperfine coupling dictates the linewidth at X and W-bands, but full resolution in **g** is achieved around 240 GHz. The X-band EPR experiments provide partially resolved isotropic hyperfine couplings. Figure 4-1 includes experimental (solid line) and simulated (dashed line) EPR spectra. This X-band data shows the presence of hyperfine coupling interactions that were estimated using the DOUBLET program, kindly provided by Dr. Andrew Ozarowski. The simulation in figure 4-1 was generated by considering contributions from the three methine bridge protons (positions α, β, δ), six methyl protons (three from the methyl on carbon 1, and three from the methyl at carbon 5), and two nitrogens (positions 22 and 24). Figure 1-3 presents the labeling assignments for these atoms. The hyperfine couplings are as follows: $A_{\mathrm{methyl}} = 3.0$ G (8.4 MHz), $A_{\mathrm{methine}} = 2.4$ G (6.7 MHz), and $A_N = 2.2$ G (6.2 MHz). The EPR line is centered at $g_{iso} = 2.003250 \pm 6\times10^{-6}$ with a linewidth of 1.2 G. This experiment gives partially resolved, isotropic hyperfine coupling constants since the liquid state averages out the anisotropic contribution. This is in agreement with previously published results [56,107]. Cryogenic X-Band EPR yields a single, unresolved line with a linewidth of 18 G.

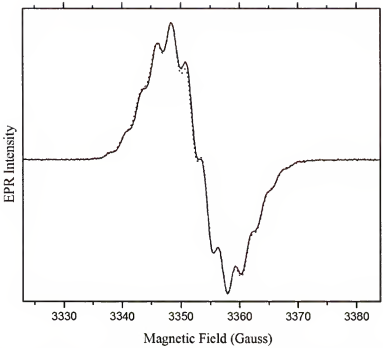

Figure 4-1 X-Band EPR of BChl *a* anion taken at 298 K and 9.405913 GHz, with 1.0 mW microwave power, 0.5 G modulation amplitude at 1 kHz, 10 ms time constant, and 20 ms conversion time. The experimental data (solid) was simulated (dotted) assuming the following hyperfine contributions: 6 x A_{methyl} = 3.0 G, 3 x A_{methine} = 2.4 G, and 2 x A_N = 2.2 G.

Pulsed experiments were done at X-Band to further investigate the hyperfine interactions in this species. Mims ENDOR was done on BChl *a* radical anion and shows two resolved proton couplings at 1.12 MHz and 9.60 MHz (see figure 4-2). Mims ENDOR is known to have blind spots that could explain the missing ENDOR transitions expected in this spectrum. However, these values fall within the range of isotropic couplings determined by the X-band cw-EPR, shown in figure 4-1. These pulsed experiments were conducted on the Bruker e580 pulsed EPR spectrometer described in chapter 3.

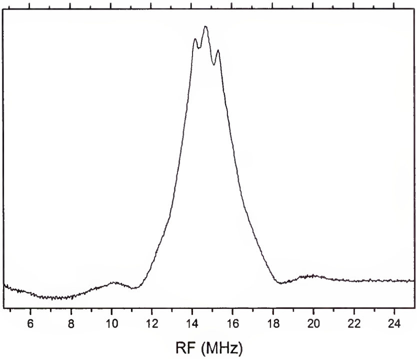

Figure 4-2 X-Band Mims ENDOR on BChl *a* radical anion, taken at 23K with two 16 ns (90°) pulses separated by 124 ns, a 7 μs RF pulse, and a 16 ns refocusing microwave pulse.

The high field EPR data show a fully resolved g-tensor at 210 GHz. Figure 4-3 shows a transmission cw-EPR experiment done at 210.374 GHz, 10 K, 1 mW microwave power, and 4 G field modulation at 1 kHz. The experimental setup for the transmission instrument is described in chapter 3. In addition to the powder pattern, this spectrum shows manganese lines from the field calibration standard. Three of the Mn lines are visible on the high field side of the radical signal, one on the low field side, and two overlap with the radical signal. The corrected g-values for BChl *a* radical anion: $g_x = 2.004257 \pm 5\text{x}10^{-5}$, $g_y = 2.003150 \pm 5\text{x}10^{-5}$, and $g_z = 2.002513 \pm 7\text{x}10^{-5}$. These g-values average to the isotropic g-value, $g_{ave} = 2.003306 \pm 7\text{x}10^{-5}$.

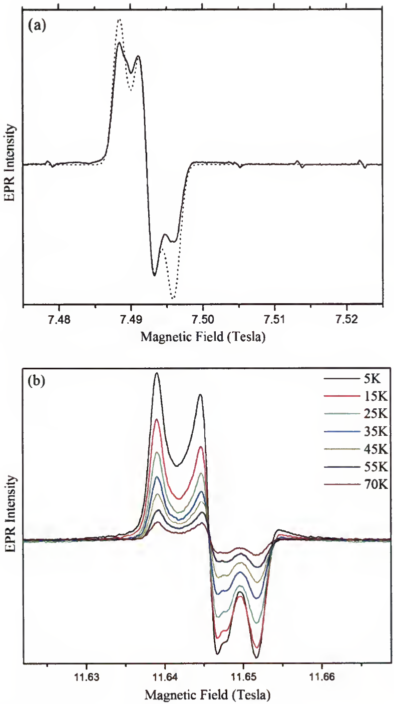

Figure 4-3 (a) High Field EPR spectrum of BChl *a* radical anion taken at 10 K and 210.374 GHz with ~ 0.4 mW microwave power and 4 G field modulation at ~1 kHz. This data was taken on the transmission setup with an MgO field standard containing manganese. The simulation employed anisotropic linewidths given by: $\Lambda_x = 4$ G, $\Lambda_y = 5$ G, and $\Lambda_z = 11$ G. (b) Temperature dependence EPR study of BChl *a* radical anion at 326.616 GHz with ~ 0.5 mW microwave power and 5 G field modulation at 1 kHz.

High field EPR and ENDOR measurements were taken at 9 T / 240 GHz, on the superheterodyne setup. This instrumental setup is discussed in chapter 3 [106]. The saturated EPR signal is shown in figure 4-4, with a fully resolved rhombic g-tensor. Figure 4-4 is a plot of the EPR intensity as the magnetic field is swept with a sweep coil, with the main coil in persistent mode at 8.560 T. This spectrum appears as an absorption due to rapid passage effects and lifetime broadening which results from saturation. ^{1}H-ENDOR spectra were taken in 10 G steps across the EPR envelope. ENDOR spectra for the principle g-values are shown in figures 4-5 through 4-7. The grid lines on figure 4-4 indicate the magnetic field value for each ENDOR spectrum. The principle g-values fall around –7 mT (g_x), -1.5 mT (g_y), and +2 mT (g_z), which correspond to 8.5988 T (g_x), 8.6036 T (g_y), and 8.6067 T (g_z) at 239.96 GHz. The ENDOR spectra have been

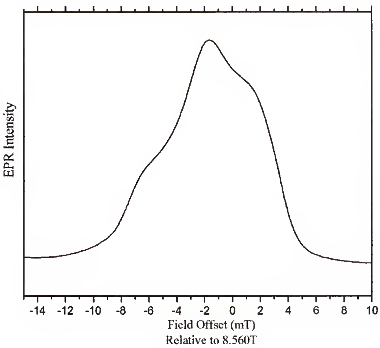

Figure 4-4 Saturated BChl *a* anion EPR signal with fully resolved g-tensor. The spectrum was taken at 30 K and 239.96 GHz, with 8.560 T persistent field, and 5 G field modulation at 1kHz.

simulated using GENDOR [107] to estimate the number and magnitude of each pair of ENDOR transitions. Figure 4-9 shows a stack plot of all the BChl *a* radical anion ENDOR spectra. These spectra change as a function of g, indicating anisotropic behavior, and hence, orientational selection. The effective hyperfine splittings obtained from the simulations are shown in figure 4-9. These data show slight anisotropy in the hyperfine couplings of certain protons. The 0.20 MHz splitting seems to be invariant throughout the ENDOR spectra. This splitting may be a natural void in the spectra resulting from the simultaneous excitation of both hyperfine transitions. This effect prevents nuclear polarization, which must be achieved to see an absorption of energy. In addition, the RF frequency is modulated at 40 kHz during the ENDOR experiments. This modulation attempts to excite more spins, but since the detection does not follow this modulation, the experiment is blind to features less than 80 kHz wide.

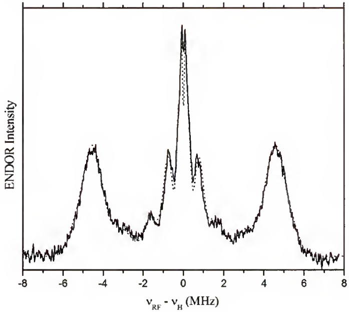

Figure 4-5 High field cw-ENDOR spectrum of BChl *a* radical anion, measured at 30K, with g = 2.00402 (–7 mT). The experimental spectrum (solid)was simulated (dotted) using the GENDOR software to estimate the hyperfine tensors. The effective hyperfine splittings are plotted in figure 4-9.

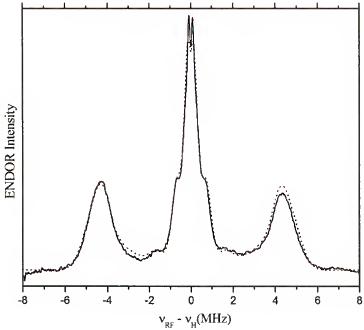

Figure 4-6 High field cw-ENDOR spectrum of BChl *a* radical anion, measured at 30K, with g = 2.00303 (-2 mT). The experimental spectrum (solid)was simulated (dotted) using the GENDOR software to estimate the hyperfine tensors. The effective hyperfine splittings are plotted in figure 4-9.

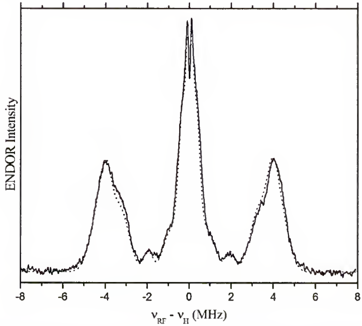

Figure 4-7 High field cw-ENDOR spectrum of BChl *a* radical anion, measured at 30K, with g = 2.00218 (+2 mT). The experimental spectrum (solid)was simulated (dotted) using the GENDOR software to estimate the hyperfine tensors. The effective hyperfine splittings are plotted in figure 4-9.

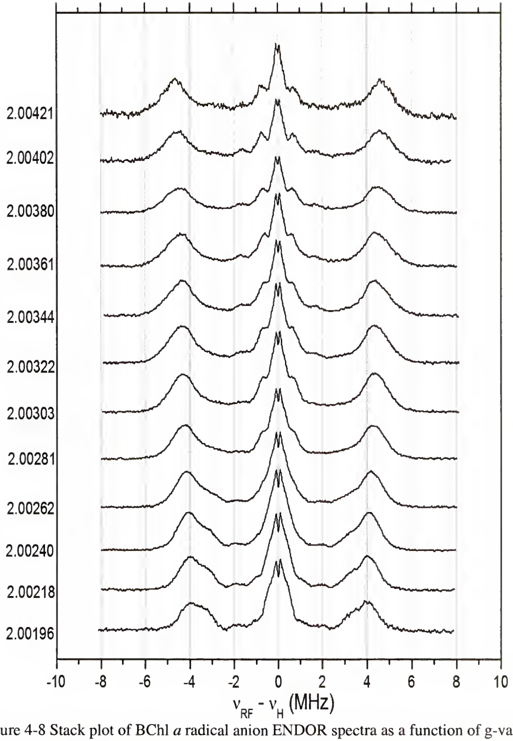

Figure 4-8 Stack plot of BChl *a* radical anion ENDOR spectra as a function of g-value. All spectra measured at 30 K, and 240 GHz. Each spectrum was signal averaged (10-20 times), which takes 3 to 7 hours.

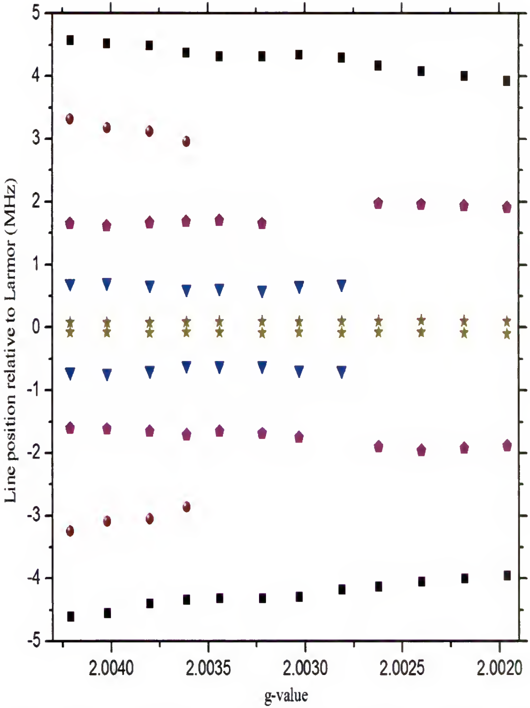

Figure 4-9 Effective hyperfine splittings obtained from the fitting of the experimental ENDOR spectra shown in figure 4-8.

Bacteriopheophytin *a* Radical Anion

BPheo *a* radical anion was generated chemically, as described in Chapter 3. This radical was measured with EPR, ENDOR and ESEEM at X-band, as well as EPR and ENDOR at W-band and at 240 GHz. The cw-EPR at X-Band shows partially resolved hyperfine structure at room temperature. Figure 4-10 shows the experimental and the simulated X-band spectra. This experiment was done at 298 K, 1.0 mW microwave power, 0.5 G field modulation at 100 kHz, 10 ms time constant, 20 ms conversion time, and a microwave frequency of 9.42581 GHz. The experimental data (solid) was fitted using the DOUBLET software to determine $g_{iso} = 2.003263 \pm 6\times10^{-6}$. The simulation (dotted) used averaged contributions from the methine bridge protons (α, β, δ), methyl protons (1a and 5a), and nitrogens 22 and 24 (see figure 1-3). The hyperfine coupling

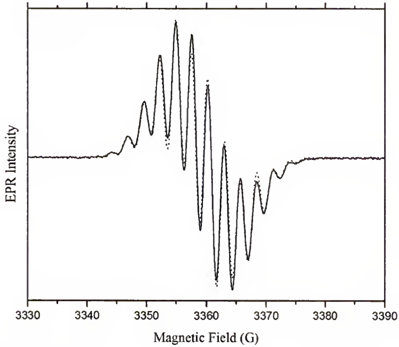

Figure 4-10 Cw-EPR of BPheo *a* radical anion at 298 K and 9.42581 GHz (X-band), with 1.0 mW microwave power, 10ms time constant, 20 ms conversion time, and 0.7 G field modulation at 100 kHz. The experimental data (solid) were simulated (dotted) to determine three unique isotropic hyperfine coupling constants: 3 x $A_{methine} = 2.5$ G, 6 x $A_{methyl} = 3.0$ G, and 2 x $A_N = 2.3$ G.

constants used for the fitting are as follows: $A_{methine}$ = 2.5 G (7.0 MHz), A_{methyl} = 3.0 G (8.4 MHz), and A_N = 2.3 G (6.4 MHz). The linewidth used in the simulation was 0.92 G. These hyperfine couplings are in agreement with previously published results, which are collected with the experimental results in table 4-1 [56].

Table 4-1 Isotropic hyperfine coupling constants for BChl a^- and BPheo a^- determined with X-band EPR.

Bacterial Pigment	Coupling Assignment	# atoms	hfc from EPR (Gauss) [56]	hfc from ENDOR (Gauss) [56]	hfc from experiment (Gauss)
BChl a^-	$A_{methine}$	2	2.5	2.5	2.4
	$A_{methine}$	1	2.0	2.0	2.4
	A_N	2	2.2	2.2	2.2
	A_{methyl}	6	3.2	3.1, 3.3	3.0
BPheo a^-	$A_{methine}$	3	2.5	2.5	2.5
	A_N	2	2.3	2.3	2.3
	A_{methyl}	6	3.0	3.0, 3.0	3.0
	$A_{unresolved}$	4	<1	0.1, 0.6	0.92 G (linewidth)

In addition to the cw experiments done at X-band, pulsed experiments were done in an attempt to estimate the hyperfine splittings of the coupled nuclei. Figure 4-11 shows the results of a 3-pulse ESEEM experiment done at 23 K. The pulse separation between the second and third pulses was increased in 8 ns steps from 100 ns to 16,376 ns. This ESEEM spectrum was baseline corrected for the T_1 decay and Fourier transformed using the Bruker software on the E580 spectrometer. The Fourier transform, shown in figure 4-12, shows a somewhat weak proton coupling at 14.7 MHz, as well as peaks at 1.77 MHz and 2.35 MHz, which result from the single quantum transitions between quadrupole levels of the nitrogen nuclei (I = 1). Isotropic hyperfine coupling constants may be estimated from the frequencies of these nitrogen transitions, but this data is known and was not extracted here.

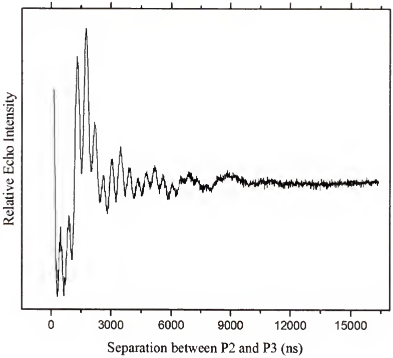

Figure 4-11 X-band 3-pulse ESEEM on BPheo *a* radical anion at 23K. The T_1 decay curve was fitted and subtracted from the ESEEM spectrum to generate this plot. The microwave frequency was 9.6854 GHz, with the magnetic field at 3452 G, with 16 ns pulses, $\tau = 120$ ns, and T incremented in 4 ns steps.

Pulsed ENDOR experiments were done at W-Band (95 GHz) on a Bruker e680 spectrometer at the NHMFL in Tallahassee, FL. These experiments showed slight g-tensor resolution enhancement over X-band, as seen in figure 4-13. This spectrum is a plot of the Hahn echo intensity as a function of the external field. The small shoulder on the low field side of the signal belongs to $g_{\perp} = 2.007766$ while the rest of the signal belongs to $g_{\parallel} = 2.005667$. These g-values are likely inaccurate due to the uncertainty in

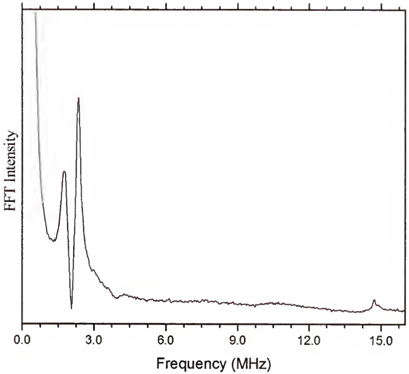

Figure 4-12 Fast Fourier transform of the time domain 3-pulse ESEEM data in figure 4-11. The spectrum shown in figure 4-11 was zero-filled to 2046 points, then smoothed with an RC filter before FFT to generate this plot.

the static magnetic field, but the anisotropy is consistent with the expected high field g-values, since $\Delta g = 2.09\times10^{-3}$. ENDOR experiments were done at the fields indicated in figure 4-13. Figure 4-14 shows the Davies ENDOR, which employed a long, 320 ns saturating microwave pulse, a 12 microsecond RF pulse, a short 180 ns microwave pulse, and a 236 ns refocusing pulse. The horizontal scale on the figure is the difference between the RF frequency of the pulse and the proton's Larmor frequency. The central feature of the spectra, at 0 MHz offset frequency, results from the matrix protons in the sample that show no hyperfine splitting. A small splitting of about 2 MHz, is apparent, yet unresolved, and appears as shoulders on the matrix peak. ENDOR transitions are also

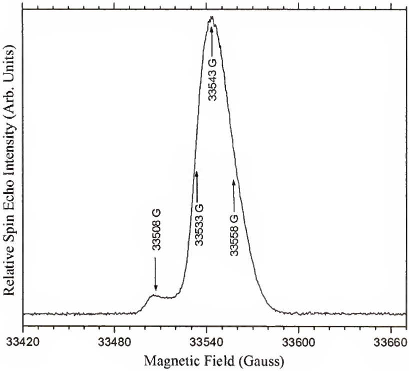

Figure 4-13 W-band echo detected field sweep of BPheo *a* radical anion, measured at 15K and 94.08275 GHz. The microwave pulses were 72 ns and 120 ns in length, separated by 300 ns. The Δg between 33508 G ($g = 2.00777$) and 33543 G ($g = 2.00567$) is 2.09×10^{-3}, which fits the estimated g-tensor anisotropy obtained at high field EPR measurements.

visible around ±4.0 MHz, at A = 8.0 MHz. Despite the presence of this ENDOR intensity around ± 4 MHz, the lack of resolution prevents the accurate determination of the hyperfine coupling. Also, several hyperfine couplings are expected to be observed in this region, so this intensity is most likely a superposition of several ENDOR lines. If orientation selection has sufficiently resolved the two apparent g-components, the convolution of lines has obscured the anisotropic information. These results indicate the need for higher fields to resolve the anisotropic hyperfine couplings.

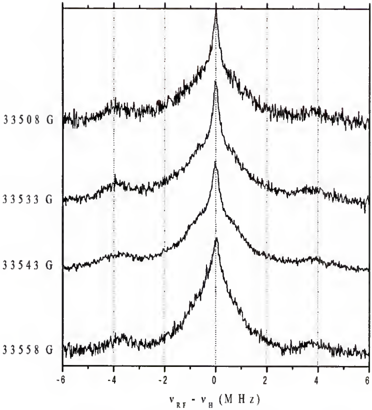

Figure 4-14 Davies ENDOR of BPheo *a* radical anion taken at 15K and 94.077 GHz ± 0.005 GHz. This experiment employed a 320 ns saturating microwave pulse, a 12 μs RF pulse, a 180 ns microwave pulse, and a 236 ns refocusing pulse. Each spectrum is a result of 20-40 averages, 7-10 hours/spectrum.

BPheo *a* radical anion was measured at high-field using the transmission cw-EPR setup described in chapter 3. Figure 4-15 shows the high field EPR spectrum (solid) as well as a simulated powder pattern (dotted). The experiment was done at 10 K with ~1 mW microwave power, 4 Gauss field modulation at 1 kHz, and a microwave frequency of 326.577 GHz. The sample was accompanied by a phosphorus doped silicon field calibration standard. The doublet lines at 11.6750 T result from the phosphorus signal (I= ½) in the standard, while the feature at 11.6400 T is of unknown origin. The simulation of the EPR data was performed using DOUBLET software that calculates

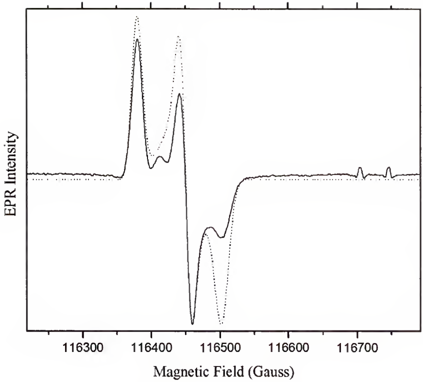

Figure 4-15 High field EPR of BPheo *a* radical anion in THF at 10 K and 326.577 GHz, with 1mW microwave power, and 6 G field modulation at ~1 kHz,. The experiment data (solid) was simulated (dotted), employing anisotropic linewidths for the components of **g**: $\Lambda_x = 7$ G, $\Lambda_y = 7$ G, $\Lambda_z = 15$ G.

field values based on the work of Michael Zerner [80]. The phosphorus spectral contribution was fitted and the g-value obtained from that fitting, $g(P_{exp})$, was used to correct the g-values for the powder pattern. The powder pattern was fitted and the experimental g-values from that fitting were adjusted by the correction factor, which is the ratio of the accepted phosphorus g-value, $g(P) = 1.998525 \pm 5\text{x}10^{-5}$, and the experimental $g(P_{exp})$. The fitting and the field correction indicate the following g-values: $g_x = 2.004459 \pm 5\text{x}10^{-5}$, $g_y = 2.003249 \pm 5\text{x}10^{-5}$, and $g_z = 2.002299 \pm 5\text{x}10^{-5}$. The average of these principal components of **g** give the isotropic constant, $g_{ave} = 2.00334 \pm 5\text{x}10^{-5}$. The estimated error in these values is derived from the minimum amount of variability in the fitted g-values while maintaining a good fit to the experimental spectrum. The discrepancies between the calculated and experimental intensities may result from incorrect polarization of the microwaves throughout the sample. Without a cavity, the polarization of the microwave radiation may not be consistent throughout the sample.

This sample was also measured on the superheterodyne setup at NHMFL, which has ENDOR capabilities. These cw-ENDOR experiments detect changes in the EPR intensity as a function of the RF frequency. The EPR transition is saturated, shown in figure 4-16, then ENDOR experiments were done at 12 different field positions across the powder spectrum. These ENDOR spectra are shown in figures 4-17 to 4-19 and show hyperfine interactions that are field dependent. These ENDOR spectra are collected in a stack plot in figure 4-20, where the ENDOR frequency seems to be dependent on the g-value.

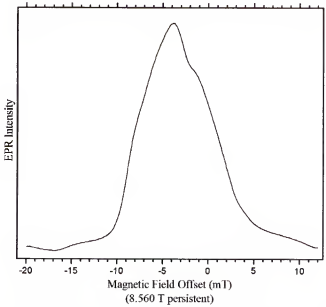

Figure 4-16 Saturated EPR absorption of BPheo *a* radical anion at 40 K and 239.57 GHz, with ~1 mW microwave power and 6 G field modulation at 1 kHz. The underlying backgound signal (below –13 mT and above 5 mT) is due to manganese in the sample holder. Rapid passage and saturation affects lead to the absorptive appearance of this powder pattern.

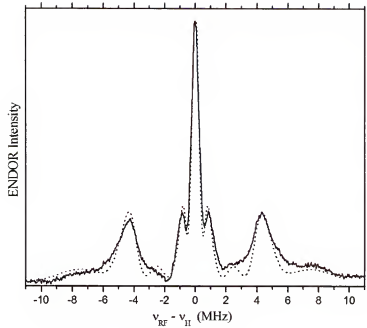

Figure 4-17 High field cw-ENDOR on BPheo *a* anion, measured on g_x at $g = 2.00415$ and 10 K. The experimental spectrum (solid) was simulated using the GENDOR software (dotted) to estimate the effective hyperfine splittings, shown in figure 4-21, and the anisotropic hyperfine tensors discussed in chapter 5.

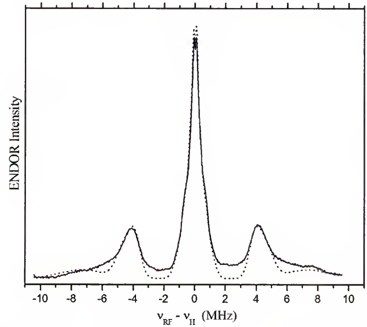

Figure 4-18 High field cw-ENDOR of BPheo *a* anion, measured on g_y at $g = 2.00338$ and 10 K. The experimental spectrum (solid) was simulated using the GENDOR software (dotted) to estimate the effective hyperfine splittings, shown in figure 4-21, and the anisotropic hyperfine tensors discussed in chapter 5.

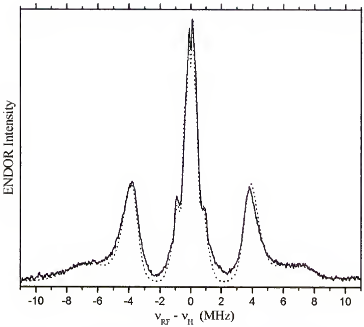

Figure 4-19 High field cw-ENDOR of BPheo *a* anion, measured on g_z at g = 2.00228 and 10 K. The experimental spectrum (solid) was simulated using the GENDOR software (dotted) to estimate the effective hyperfine splittings, shown in figure 4-21, and the anisotropic hyperfine tensors discussed in chapter 5.

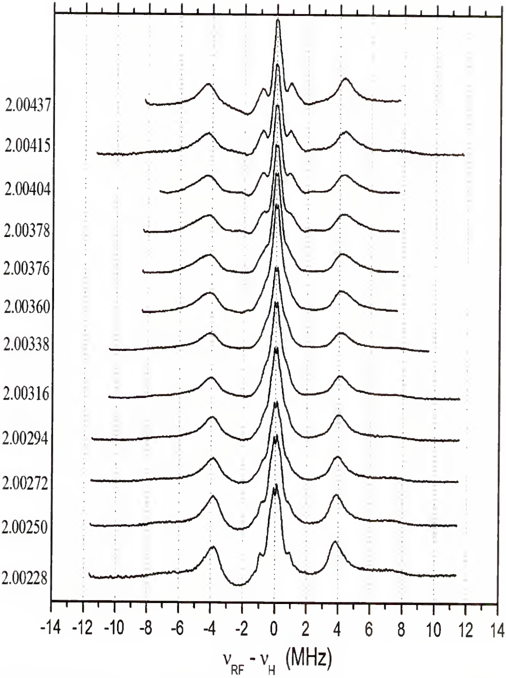

Figure 4-20 Stack plot of cw-ENDOR spectra on BPheo *a* radical anion at 10 K and 239.57 GHz. Each spectrum was signal averaged 10-30 times, which requires 4-9 hours/spectrum.

The position of the ENDOR transitions leads to effective hyperfine splittings, which are presented in figure 4-21.

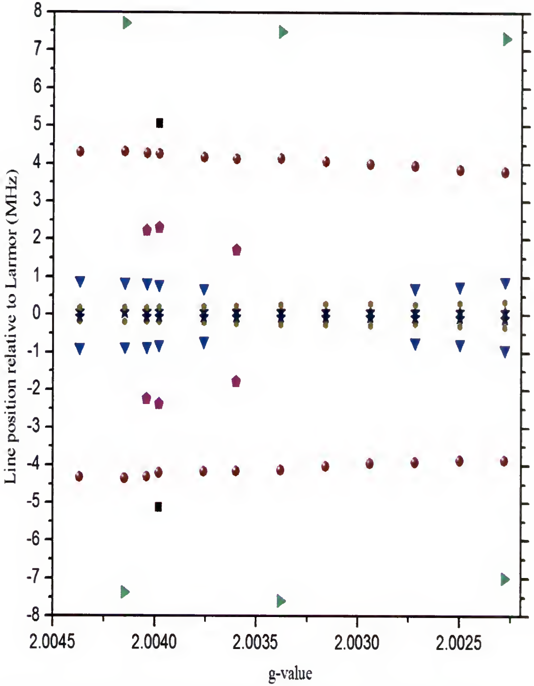

Figure 4-21 Effective hyperfine splittings for BPheo *a* radical anion obtained through simulation of the orientationally selective ENDOR spectra shown in figure 4-20.

Bacteriochlorophyll *a* Radical Cation

The BChl *a* radical cation was investigated using pulsed W-band EPR and ENDOR techniques. The EPR signal was initially detected using X-band, which shows little hyperfine resolution, shown in figure 4-22. This spectrum is shown with a DOUBLET simulation, which determined $g_{iso} = 2.003308 \pm 5 \times 10^{-5}$. The simulation includes isotropic hyperfine interactions that were determined through ENDOR and TRIPLE resonance studies [67,109]. Higher fields were employed in attempts to resolve the anisotropic interactions. The W-band EPR signal was detected using a Hahn echo pulse sequence. This experiment uses a 72 ns pulse, followed by a 120 ns pulse. Figure 4-23 plots the

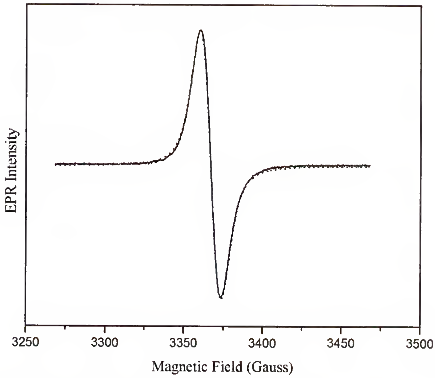

Figure 4-22 X-band cw-EPR spectrum of BChl *a* radical cation at 298 K and 9.440197 GHz with 2 mW microwave power, 10 ms time constant, 20 ms conversion time, and 1 G field modulation at 100 kHz. The experimental data (solid) was fitted using DOUBLET, which employed a Lorentzian lineshape with 3.9 G linewidth and the following hyperfine couplings: 4 x A_{beta}= 4 G, 3 x $A_{methyl-1}$ = 1.76 G, and 3 x $A_{methyl-5}$ = 3.4 G.

intensity of the spin echo as a function of magnetic field at W-band. This EPR line appears to be a single, featureless line with little g-resolution. This result is not surprising considering the g-tensor anisotropy for this cation is known to be less than the corresponding anion. The spin-spin (T_2) and spin lattice (T_1) relaxation times were determined to be 475 ns and 6 μs, respectively. T_2 was measured by generating a spin echo, then increasing the time between the second microwave pulse and the detection, τ. This separation, t, is plotted against the echo intensity. This experiment uses two 120 ns microwave pulses, initially separated by 400 ns, which is increased in 8 ns steps. This experiment detects the diffusion of the spin packets, which is seen as a

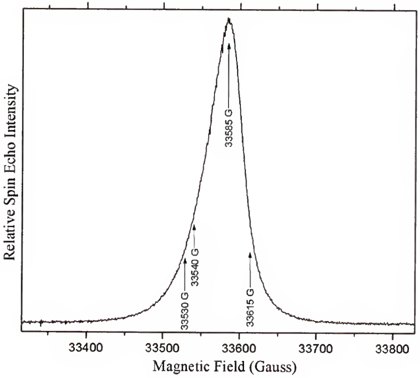

Figure 4-23 Echo detected field sweep on BChl *a* radical cation measured at 15 K and 94.2862 GHz. Two 80 ns pulses were separated by 240 ns, followed by a 180 ns pulse at 604 ns. The arrows indicate the field values for the Davies ENDOR spectra.

reduction in the echo intensity as τ is increased. T_2 was found to be 475 ns. The T_1 measurement was estimated using a saturation recovery experiment, which polarizes the spins by 180° microwave pulse, followed by a long delay time (on the order of T_1), which is increased in 32 ns steps. The magnetization is then projected onto the xy-plane by a Hahn echo sequence. Thus, the magnitude of the longitudinal magnetization vector will determine the intensity of the echo. The echo intensity is monitored as the delay between the long saturating pulse and the Hahn sequence are increased. The echo intensity grows with a time constant, $T_1 = 6\ \mu s$, for this sample.

Mims and Davies ENDOR experiments were performed at the field positions indicated in figure 4-23. These ENDOR spectra are shown in figures 4-24 and 4-25. The Davies ENDOR experiments use a 184 ns microwave pulse, followed by an 18 μs RF

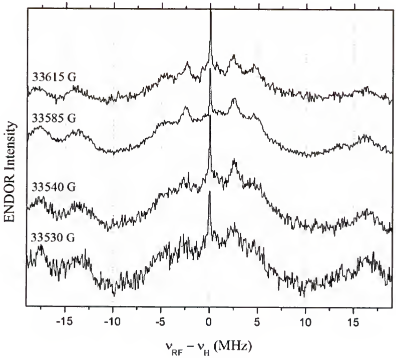

Figure 4-24 Davies ENDOR on BChl *a* radical cation taken at 15K and 94.1415 GHz, which employed a 180 ns π pulse, 11 μs RF pulse, and two 160 ns microwave pulses. The shot repetition time was 8 ms.

pulse, followed by a Hahn echo pulse sequence (92ns and 160 ns). Figure 4-24 shows the Davies spectra taken at different field positions on the EPR envelope. The hyperfine couplings show little variation between these spectra, which indicates that orientational selection may not have been achieved. However, the spectra taken at the low and high field edges of the EPR envelope show an additional hyperfine coupling which is not visible in the 33585 G spectrum. The experimental values for these couplings are tabulated in table 4-2. The Mims ENDOR spectra show similar spectra at the different field positions, however, the differences are subtle, and unfortunately, not resolved enough to make definitive assignments.

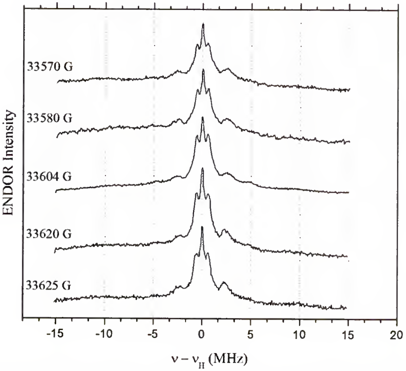

Figure 4-25 Mims ENDOR on BChl *a* radical cation taken at 15K and 94.2862 GHz with two 80 ns microwave pulses separated by 240 ns, a 12 μs RF pulse, then a third 80 ns microwave pulse. The shot repetition time was 8 ms.

Table 4-2 Davies and Mims ENDOR data for BChl *a* radical cation

Field (G) Davies	Field (G) Mims	hfc #	A ± 0.25 MHz Davies Couplings	A ± 0.25 MHz Mims Couplings
33530	33570	1	1.18	1.16
		2	4.93	5.12
		3	9.39	-
33540	33580	1	1.49	1.12
		2	5.17	5.1
		3	9.86	-
33585	33604	1	-	1.11
		2	4.93	5.09
		3	9.78	-
33615	33620	1	1.48	1.17
		2	5.09	4.63
		3	9.24	-
	33625	1	-	1.22
		2	-	4.69

Bacteriopheophytin *a* Radical Cation

The BPheo *a* radical cation was successfully studied with X-band and W-band EPR and ENDOR, while complications limited the success of the high field work. The X-band EPR results in a featureless line at room temperature and under cryogenic conditions, with a linewidth of 9 G (not shown). W-band experiments showed little enhancement in g-resolution, as seen in figure 4-26 by the lack of resolution in the principal g-components. The bulk of this signal results from the BPheo *a* cation, while the sharp feature at 33668 G could be another radical species formed during the oxidation. The 33668 G feature is most likely due to a different radical with a much longer T_2, since it has a much sharper linewidth than the BPheo *a* radical signal. This sharp radical signal has g = 2.002964, while the low field signal is closer to 2.005943 ±

0.003. Unfortunately, the lack of a field calibration standard prevents accurate g-value measurements at this frequency. ENDOR spectra were taken at the indicated points on the spin echo envelope. The Davies spectra, shown in figure 4-27, show little anisotropy with respect to the magnetic field. The measured hyperfine coupling values from the W-band experiments are listed in table 4-5. The Mims ENDOR spectra show slight differences in the range of A = 6 MHz. The high field spectrum in figure 4-28 shows broad wings with A = 14-15 MHz, which are absent in the low field spectrum. Due to the apparent lack of resolution in g, these experiments were not pursued. High field EPR was attempted but line-broadening affects were observed above W-band, which prevented the measurement of the principal components of **g**.

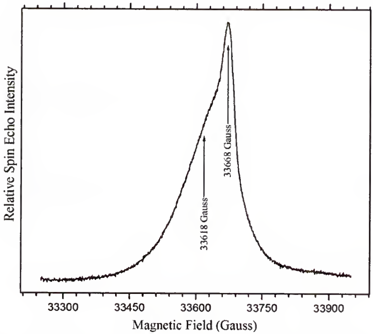

Figure 4-26 Echo detected field sweep of BPheo *a* radical cation at 20 K and 94.3859 GHz. This experiment employed two microwave pulses of length, 192 ns and 260 ns separated by 800 ns. The shot repetition time was 6 ms.

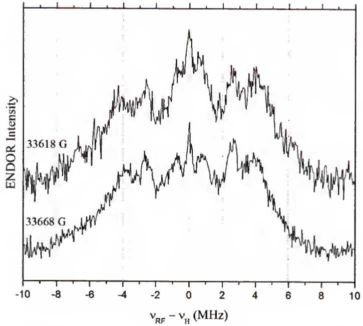

Figure 4-27 Davies ENDOR of BPheo *a* radical cation at 20 K and 94.0827 GHz, which employed a 200 ns π pulse, 12 μs RF pulse, and two 190 ns microwave pulses. The shot repetition time was 8 ms.

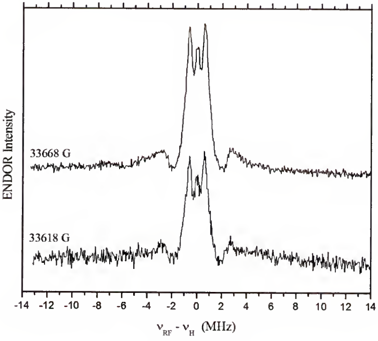

Figure 4-28 Mims ENDOR of BPheo *a* radical cation at 20 K and 94.0730 GHz, which employed three 80 ns microwave pulses with the second and third pulses separated by a 12 μs RF pulse. The shot repetition time was 10 ms.

Table 4-3 BPheo *a* radical cation pulsed W-band ENDOR data.

ENDOR Experiment	Field	A_1	A_2	A_3	A_4
Davies	33618	1.6 MHz	3.3 MHz	5.2 MHz	8.7 MHz
	33668	1.6 MHz	3.1 MHz	5.2 MHz	7.7 MHz
Mims	33618	1.3 MHz		5.2 MHz	
	33668	1.3 MHz		5.2 MHz	

Chlorophyll *a* Radical Anion

The Chl *a* radical anion was generated using potassium metal in tetrahydrofuran (THF) using high vacuum techniques described in chapter 3. This radical was examined with EPR at 9.5 GHz and 330 GHz. X-Band EPR spectra consist of a single inhomogeneously broadened line, with an isotropic g-value of 2.002667 $\pm$ 6x10^{-6}. Figure 4-29 shows the X-band spectrum taken at 298 K, with a 100 kHz field modulation of 2 G, 20.48 ms time constant, 40.96 ms conversion time, and 2 mW microwave power. This radical signal has a linewidth of 8 G at room temperature. The experimental data was simulated using DOUBLET to obtain the g-value, as well as the indication of unresolved hyperfine interactions. The fit (dotted line) in figure 4-29 uses hyperfine contributions from three different types of protons (A = 1.1, 2.7, 2.9 G). These contributions are estimates since the splitting is unresolved under these conditions. The lineshape in this simulation is assumed to be 90 percent Lorentzian. EPR of this radical was also measured at higher fields in frozen solution, shown in figure 4-30. This experiment was performed on the transient EPR setup at the NHMFL, described in chapter 3. The g-tensor achieved full resolution above 280 GHz, with values: g_x = 2.004074 $\pm$ 5x10^{-5}, g_y = 2.002884 $\pm$ 5x10^{-5}, g_z = 2.002024 $\pm$ 8x10^{-5}, which lead to an average value of g_{ave} =

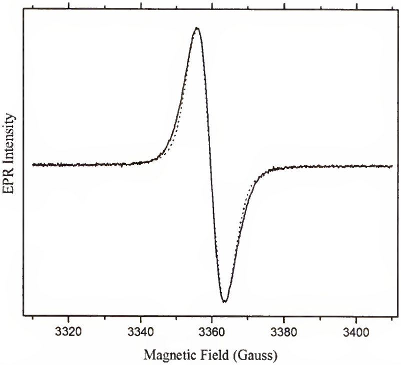

Figure 4-29 EPR spectrum of Chl *a* radical anion at 298 K and 9.423040 GHz with 2 mW microwave power and 2 G field modulation at 100 kHz. The experimental data (solid) was simulated (dotted) assuming a Lorentzian lineshape at g_{iso}= 2.002667 ± 6x10^{-5} with three different proton hyperfine interactions: A_1 = 1.1 G, A_2 = 2.7, and A_3 = 2.9 G.

2.002994 ± 8x10^{-5}. The g-values were obtained through fitting the data with the DOUBLET software. The magnetic field was calibrated using a phosphorus doped silicon standard with known g-value. The field correction procedure was described in the bacteriopheophytin *a* radical anion high field EPR results. This spectrum was fitted using anisotropic linewidth approximations where, Λ_x = 10 G, Λ_y = 7 G, and Λ_z = 15 G. The poor fit on g_z introduces some error in this data point, and the sources of this poor fit will be addressed in the discussion.

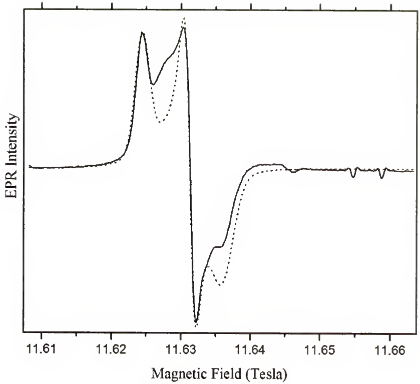

Figure 4-30 EPR of Chl *a* radical anion with phosphorus standard at 15 K and 326.13 GHz with 4 G field modulation, and ~0.9 mW microwave power. The experimental spectrum (solid) was simulated (dotted) using anisotropic linewidths given by: $\Lambda_x = 10$ G, $\Lambda_y = 7$ G, $\Lambda_z = 15$ G..

Chlorophyll *b*

Chl *b* radical anion was studied with EPR at X-band and at 330 GHz. The X-band spectrum at 298 K shows a single EPR line with $g_{iso} = 2.002846 \pm 6\text{x}10^{-6}$. Figure 4-31 shows the X-band data with a simulation that accounts for three predicted hyperfine couplings. The parameters for this experiment are: 2 G field modulation at 100 kHz, 20.48 ms time constant, 40.96 ms conversion time, and 2 mW microwave power. Unresolved hyperfine couplings are present and are possibly broadened by concentration effects. However, these hyperfine couplings must be on the order of the linewidth, so they should hardly be resolved under these conditions. The solid line in figure 4-31 is experimental data and the dotted line is a simulation obtained with the DOUBLET

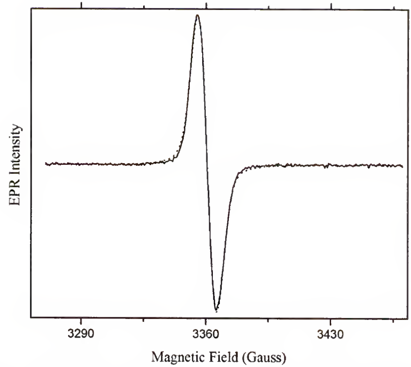

Figure 4-31 X-band EPR of Chl *b* radical anion at 298K and 9.426530 GHz, with 1 mW microwave power, 10 ms time constant, 20 ms conversion time, and 1 G field modulation at 100 kHz. The experimental data (solid) was simulated (dotted) using the DOUBLET software with the following hyperfine coupling constants: 3 x A_1 = 1.0 G, 3 x A_2 = 2.7 G, and 3 x A_3 = 3.1 G.

software. The simulation approximates a Lorentzian shape, with isotropic hydrogen and nitrogen couplings, $A < 3$ G.

The Chl *b* radical anion was measured using high field, cw-EPR on the transmission instrument described in chapter 3. This experiment applies 326.13 GHz microwave radiation at magnetic fields around 11 T. These experimental conditions are required to fully resolve the g-tensor into the three principle components. The high field spectrum is shown in figure 4-32, with $g_x = 2.003964 \pm 5\text{x}10^{-5}$, $g_y = 2.002779 \pm 5\text{x}10^{-5}$, and $g_z = 2.001896 \pm 7\text{x}10^{-5}$, which lead to an average value of $g_{ave} = 2.002880 \pm 7\text{x}10^{-5}$. The radical sample is accompanied by a phosphorus doped silicon, field calibration standard. The standard is the source of the weak doublet up field from the powder pattern. The field correction procedure has been discussed in the BPheo *a* radical anion results. The experimental g-values are shown in table 4-4.

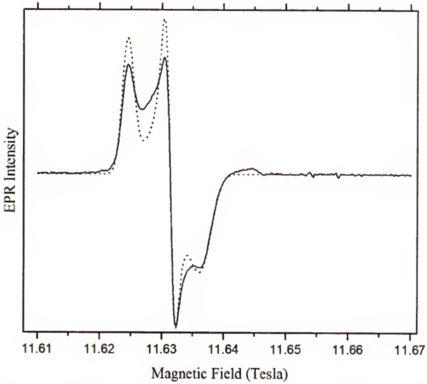

Figure 4-32 High field EPR spectrum of Chl *b* radical anion at 15K and 326.13 GHz, with 5 G field modulation and ~0.9 mW microwave power. The two weak, high field lines are the phosphorus field calibration standard. The experimental spectrum (solid) was simulated (dotted) using anisotropic linewidths given by: $\Lambda_x = 10.5$ G, $\Lambda_y = 7.3$ G, $\Lambda_z = 17$ G..

Table 4-4 Radical anion g-tensor data. These measurements were taken on the transmission setup and correspond to different samples, which were prepared identically, according to the procedures in chapter 3.

Sample	g_{xx}	g_{yy}	g_{zz}	$(g_{xx}-g_{yy})$	$(g_{yy}-g_{zz})$	Microwave Frequency (GHz)
Bacteriochlorophyll *a* $^{-}$	2.004257[a]	2.003150[a]	2.002513[a]	0.001107	0.000637	326.81
	2.004257[a]	2.003123[a]	2.002333[b]	0.001134	0.000790	327.98
	2.004237[a]	2.003112[a]	2.002051[c]	0.001125	0.001061	326.81
	2.004567	2.003207	2.002256	0.001360	0.00951	DFT
Bacteriopheophytin *a* $^{-}$	2.004459[a]	2.003249[a]	2.002299[a]	0.001210	0.000950	326.13
	2.004423[a]	2.003144[c]	2.002274[f]	0.001279	0.000870	326.13
	2.004504[b]	2.003294[b]	2.002344[e]	0.001210	0.000950	326.58
	2.003991	2.002945	2.002176	0.001047	0.000768	DFT
Chlorophyll *a* $^{-}$	2.004012[a]	2.002912[a]	2.002027[d]	0.00110	0.000885	326.11
	2.004074[a]	2.002884[a]	2.002024[d]	0.00119	0.000860	326.36
	2.004079[a]	2.002869[a]	2.002239[f]	0.00121	0.00063	326.16
Chlorophyll *b* $^{-}$	2.003964[b]	2.002779[b]	2.001896[c]	0.001185	0.000883	326.13

The superscripts a-f denote the experimental error in that measurement: a = $5\text{x}10^{-5}$, b = $6\text{x}10^{-5}$, c = $7\text{x}10^{-5}$, d = $8\text{x}10^{-5}$, e = $9\text{x}10^{-5}$, f = $1\text{x}10^{-4}$. These values were derived from the quality of the fitting to the hf-EPR data.

CHAPTER 5
DISCUSSION

Bacteriochlorophyll *a* Radical Anion

At 210 GHz the anisotropy of the Zeeman splitting exceeds the hyperfine linewidth, allowing accurate g-tensor determination. The high-field EPR spectrum shown in figure 4-3 shows a fully resolved powder pattern with rhombic symmetry. The following discussion will require the use of a reference frame for the g-tensor orientation. The molecular axes will be defined X, Y, and Z, where X forms a vector between N_{II} and N_{IV}, Y forms a vector between N_I and N_{III}, and Z is normal to the XY plane containing all four nitrogens. The $g_z = 2.002513 \pm 5 \times 10^{-5}$ component closely resembles the free electron g-value, $g_e = 2.0023193$. This value is in good agreement with density functional theory (DFT) predictions using a double zeta basis, which gives $g_z = 2.0022558$, oriented 84° to the XY plane. The IIRC calculation used an unrestricted Hartree-Fock double zeta basis, which describes each atomic orbital with two functionals (dz) that are functions of the electron density and the gradient of this density over the entire molecule. The gradient correction to the exchange functional is "revised PBE" and the correlation functional is "PBE." This predicted orientation of g_z is in line with generally accepted theory regarding the nature of the electron density on a planar, organic π-radical. According to Stone, the g_z axis for doublet π-radicals should lie perpendicular to the plane of conjugation [76]. In this normal orientation, the p_z orbital cannot mix with heavy atoms or orbitals in the plane of the conjugation to obtain orbital angular momentum. This orientation allows it to maintain a value close to that of the free electron, as shown in equation 2-3. Relativistic mass effects and gauge corrections are proposed to explain the observed behavior of $g_z < g_e$ [41,75,79,80]. However, the deviation of the measured g_z value from g_e could also result from an angle slightly less than 90° to the conjugation plane, as was determined by Bratt et al. for the Chl *a* radical cation [74].

In order to fit the powder pattern, anisotropic linewidths for the principal components of **g** were employed. These linewidth affects indicate a broadening phenomenon such as anisotropic hyperfine interaction or environmental interactions that selectively broaden g_z. Burghaus et al. have observed selective broadening effects in quinone radicals where hydrogen-bonding interactions shift the components of **g** oriented toward the interacting solvent molecule up to $g \pm 1\text{x}10^{-4}$ [113]. Their study observed dipolar broadening of certain lines of a powder pattern depending on the hydrogen bonding ability of the solvent with the quinone radical. A similar phenomenon may be responsible for the broadened g_z component of the BChl *a* radical anion EPR spectrum. The THF solvent molecules contain an oxygen atom which can serve as a fifth ligand to the central Mg atom in BChl *a*. Although hydrogen bonding would be expected to have a stronger effect on the MO of the radical, the potential for electrostatic interaction exists. This prediction is justified by the localization of electron density in the Z dimension of the radical, which is the very same dimension that has the potential for intermolecular interactions with Mg. It should be mentioned, that the concentration of spin density on the oxygen atoms of quinone radicals is much higher than on the magnesium atom of BChl *a* radical anion. This behavior should weaken the effect of intermolecular interactions on the g-tensor.

The remaining components of the g-tensor were found to be $g_x = 2.004257 \pm 5x10^{-5}$, $g_y = 2.003150 \pm 5x10^{-5}$, which deviate from g_z. The spin-orbit interactions that lead to this deviation mainly result from heavy atoms, such as nitrogen and oxygen. The nitrogen atoms of rings II and IV are directly linked to the conjugated system, which should lead to a higher concentration of spin density than N_I and N_{III}. This assumption would indicate a larger degree of spin-orbit interaction along the X-axis than on the Y-axis of the radical. Only two oxygen atoms, the ring I acetyl group and the ring V carbonyl group, are expected to interact with the spin density of this radical. It has been predicted that the acetyl group's orientation can affect the values of the g-tensor and it's orientation for BChl a^+ [33,73] and Chl a^+ [74]. Plato et al. predict that by rotation of the acetyl group, relative to the conjugation plane, g_z and g_y become nearly degenerate at an angle of ± 45° [33]. As this group is rotated out of the molecular plane, the p_z orbitals

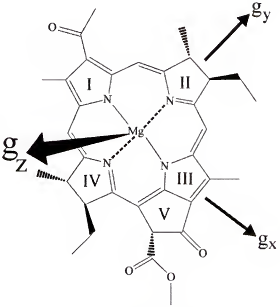

Figure 5-1 Proposed orientation of **g** on the BChl *a* radical anion. The smallest spin-orbit interactions lead to g_z oriented perpendicular to the plane of the molecule, while the highest degree of spin-orbit interactions are found on rings I and III. The nitrogen atoms on rings II and IV also interact with the spin density, bringing the value of g_y away from g_z.

can mix with the lone pairs on the oxygen. This interaction increases g_z and decreases g_y, which results in near axial symmetry. The g-tensor will be influenced by the amount of spin density on the acetyl group, which may differ between the cation and the anion. Since powder EPR experiments provide limited information on the orientation of the g-tensor, theoretical models were employed.

Using the revPB BLYP level of theory and employing a double-zeta basis set, DFT predicts the following g-values: g_x= 2.004567 and g_y = 2.003207, which differ from experiment by $2x10^{-4}$ for g_x and $-2.3x10^{-5}$ for g_y. The calculation of g_x predicted an orientation of 89° from X and 105° from Y, while g_y was predicted to be 19° from X and 74° from Y. This orientation of the g-tensor on the molecular axes is depicted in figure 5-1. The spin density, per carbon atom, on rings I (0.051) and III (0.057) has been estimated theoretically to be approximately four times larger than the density on rings II (0.026) and IV (0.014) [56]. This concentration of spin density on the opposing rings should influence the geometry of the g-tensor. However, the influence of the heavier nitrogen atoms, N_{II} and N_{IV}, may outweigh the relatively light atoms, with small spin-orbit coupling constants, such as hydrogen and carbon. The spatial spin density plots shown in figure 5-2 were generated by Dr. Alex Angerhofer from DFT calculations to help visualize the atoms with a higher concentration of spin density. Figure 5-2(a) contains a spatial distribution plot of the alpha spin HOMO state (neutral LUMO), while the total spin density, which is the difference between the alpha and the beta spin densities, is shown in figure 5-2(b) and 5-2(c). In figure 5-2(b) and 5-2(c), the blue regions of highly concentrated spin density indicate the atoms that can contribute orbital angular momentum to the electronic wavefunction. Of course, atoms such as nitrogen and oxygen are expected to have a stronger effect on the g-tensor than carbon and hydrogen. The nitrogen atoms, N_{II} and N_{IV}, are indicated with the arrows in figure 5-2(b) and 5-2(c). According to the DFT predictions, these two atoms have considerable spin density, which should lead to spin orbit interactions in this dimension of **g**. Lubitz et al. found the isotropic hyperfine couplings to be $A_{N(II)} = 6.52$ MHz and $A_{N(IV)} = 5.86$ MHz, with negligible couplings on N_I and N_{III}, using TRIPLE and ENDOR spectroscopy in solution [108]. However, the sheer number of coupled protons and the weakly coupled oxygen atoms on ring V and the carbon 2 acetyl, could introduce more spin-orbit interaction along the Y dimension, which would explain the predicted g-tensor orientation shown in figure 5-1. A similar g-tensor orientation has been determined through experiment and theory for P_{700}^+ [124], P_{865}^+ [33,73], and BChl *a*$^+$ [33].

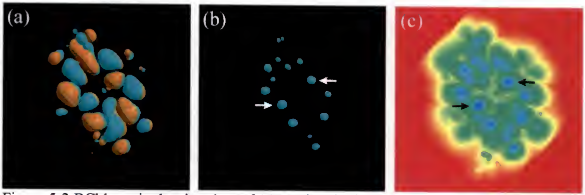

Figure 5-2 BChl *a* spin density plots of (a) spatial distribution of the neutral LUMO (b) net spin density spatial plot, (c) average net spin density projection with increasing concentration from red to blue. The arrows in (b) and (c) indicate nitrogens II and IV, which should strongly contribute to the g-factor.

Isotropic hyperfine data have been obtained previously with EPR [56], ENDOR [56,108], and TRIPLE [108] resonance techniques, as well as DFT predictions [109]. At X-Band (9.5 GHz), and W-Band (95 GHz), frozen solution EPR yields a single featureless line, which is inhomogeneously broadened to 18 G (at X-band) by unresolved hyperfine couplings. In solution, however, this anisotropic interaction is averaged beyond the timescale of the experiment and the isotropic coupling can be measured. Figure 4-1 contains the X-band cw-EPR spectrum with partially resolved hyperfine couplings. These splittings represent the Fermi contact interaction between the electron density and coupled protons, which is directly proportional to the electron density at the carbon nucleus. The spectrum shown in figure 4-1 was fitted using DOUBLET software to approximate the hyperfine couplings. The values obtained were in agreement with Fajer et al., who performed solution state EPR and ENDOR experiments on selectively deuterated BChl *a* and BPheo *a* radical anions [56]. Fajer's work concluded that the methyl groups of carbons 1 and 5 produce the largest couplings of 3.1 G (8.7 MHz) and 3.3 G (9.2 MHz) respectively (see figure 5-3 for atomic numbering). These couplings are observed in solution state EPR as the average of the splittings from the protons on each methyl group. The methine protons (α, β, and δ) produced partially resolved ENDOR lines with hyperfine couplings of 2.0 G (5.6 MHz) and 2.5 G (7.0 MHz) with relative intensities 1:2, indicating that two of the methine protons show similar hyperfine interaction at 5.6 MHz, and one shows a stronger interaction at 7.0 MHz. ENDOR lines were also observed at 0.6 G (1.7 MHz), assigned to β-protons (positions 3, 4, 7, 8), and 0.1 G (0.3 MHz), which were assigned to the remaining weakly coupled protons. The X-band EPR experiment shown in figure 4-1 identifies the radical as BChl *a* radical anion, and measures the isotropic hyperfine couplings for reference. The simulation in figure 4-1 employs the following couplings to fit the experimental data: $A_{methine} = 3.0$ G (8.4 MHz), $A_{methyl} = 2.4$ G (6.72 MHz), and $A_N = 2.2$ G (6.16 MHz). These numbers are in agreement with published data [40], and are presented in table 4-1.

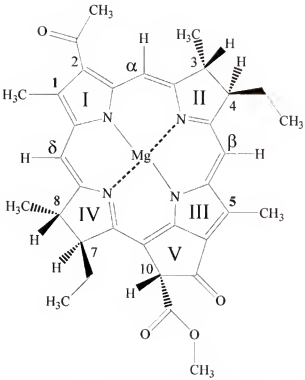

Figure 5-3 Molecular structure and atomic numbering of BChl *a*. The phytyl tail (originating from carbon 7) has been truncated to a methyl group.

In order to build on the isotropic hyperfine coupling estimations from X-band, high field ENDOR experiments were done to estimate the total hyperfine interaction. This work shows orientationally selected ENDOR, which probes the total (anisotropic and isotropic) hyperfine coupling. The ENDOR spectra, shown in figure 4-8, imply that the hyperfine tensors are oriented perpendicular to the g-tensor reference frame [86,88,110]. This relative orientation is assumed since the A_z component of the A-tensor is expected to lie along the σ bond that links the proton to the conjugated system. As seen in figure 5-1, the g-tensor maintains g_z normal to the plane of conjugation, while the protons lie within the g_{xy}. Also, the symmetric spacing of the ENDOR transitions about the nuclear Larmor frequency indicates that the hyperfine tensors are oriented with axes coincident with the g-frame [86,87]. In this radical, hydrogen and nitrogen nuclei directly interact with the electronic wavefunction, but only proton couplings were measured here, due to experimental limitations on the spectrometer. The ENDOR coil of the probe, shown in figure 3-6, was optimized for protons. Hydrogen nuclei are about 10 times more sensitive to NMR since, $\frac{\gamma_H}{\gamma_N} \cong 10$. Due to the difference in gyromagnetic ratio, nitrogen nuclei require a much larger B_2 field to induce a nuclear transition. Since BChl *a* radical anion has strongly and weakly coupled protons, a range of hyperfine interactions is observed.

The distant or weakly coupled nuclei show somewhat isotropic splittings. That is, the hyperfine interaction is weaker in general, due to smaller electron density at the nuclei (which reduces the A_{iso}) and a larger distance from the electronic wavefunction (which reduces A_{dip}). The anisotropic (dipolar) hyperfine interaction dies off as r^{-3}, where r represents the averaged distance between the electron density and the coupled nucleus. This separation dependence is shown in equations 2.10 and 2.11. As seen in figure 4-8, these distant protons show the smallest splittings, between 0.20 MHz and 1.0 MHz. It is reasonable to assume that the ENDOR intensity at the $A_1 = 0.20$ MHz splitting could result from many distant protons whose coupling constants are too similar to resolve (see figure 5-4). These transitions could result from protons at positions 3, 4, 7, 8, and 10, which have been estimated experimentally and theoretically to have isotropic couplings between 0.50-1.8 MHz [56,109]. The presented theoretical DFT predictions estimate isotropic couplings of 1-2 MHz for these protons. The splitting of the second set of ENDOR lines increases as the field is increased from g_x to g_z. At g_x the splitting is around 0.4 MHz that seems to increase to 0.85 MHz at g_z. This coupling was fit to the following hyperfine tensor: $A_2 = [0.4, 0.85, 0.4]$ MHz, which gives $A_{2(iso)} = 0.55$

MHz. This coupling could result from the carbon 2 methyl group, which is known to have $A^{2methyl(iso)} = 0.4\text{-}0.5$ MHz [108]. The third coupling is weak, and becomes broadened between the low and high field ENDOR spectra. The approximate splitting of this transition ranges from 3.0 MHz at g_x to 4.0 MHz at g_z and was fit to an anisotropic hyperfine tensor, $A_3 = [3.0, 3.0, 4.0]$ (in MHz). The broadening of these lines through the other ENDOR spectra could indicate the presence of another pair of ENDOR lines crossing the A_3 lines. So, there is some uncertainty in the assignment of A_3 to this feature, since the lines cannot be distinguished in many of the spectra. The fourth pair of ENDOR transitions has a splitting of ~6 MHz at g_x, which increases to ~7 MHz at g_z. These ENDOR lines fall on the outer wings of the spectra, which appear to be a superposition of two or three unresolved transitions. The expected hyperfine couplings for the methyl and methine protons are similar enough to fall in these outer wings. So, it is conceivable that protons from α, β, methyl 1, and methyl 5 are superimposed in the region of A_4 and A_5. The ENDOR spectra were fitted to the following hyperfine tensors: $A_4 = [6.6, 7.2, 9.2]$ MHz, where $A_{4(iso)} = 7.7$ MHz and $A_5 = [8.0, 9.2, 9.5]$ MHz, where $A_{5(iso)} = 8.9$ MHz. These isotropic couplings have been compared to the DFT theoretical predictions in figure 5-5. Since ENDOR experiments are blind to the sign of a hyperfine coupling constant, these numbers could be positive or negative, and both have been plotted in figure 5-5. The best agreement with the literature X-band data and the theoretical predictions assign A_4 to the β proton or the methyl 1 protons (shown in table 5-1 and 5-2). The isotropic value of A_5 agrees with the α and methyl 5 couplings. Measuring the ENDOR at 30 K stopped the rotational motion of the methyl groups, which could complicate the resolution in the individual protons' resonances. Higher temperature experiments were attempted, but the EPR intensity was too weak to detect ENDOR above 60 K. Since these couplings are unresolved, the experimental spectra can only be estimated through speculation and theoretical models.

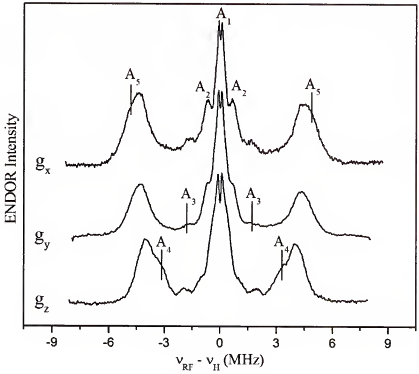

Figure 5-4 BChl *a* radical anion ENDOR spectra from the principal g-tensor components with the individual transitions labeled A_1-A_5.

Theoretical (DFT) methods were employed to investigate the hyperfine couplings measured in the hf-ENDOR experiments. Figure 5-5 plots the isotropic hyperfine coupling constants calculated with the indicated basis sets, the data measured experimentally by Lubitz et al. at X-band [108,109], and the average values of the hyperfine tensors derived from the hf-ENDOR experiments. Agreement between the theoretical predictions and the X-band experiments is good, except on the α and β protons. The theory does quite well for the methyl protons, but deviates from the methine protons: α and β. However, the DFT calculations presented here predict the correct sign of the hyperfine coupling constant, which is an improvement over pure DFT functionals [109] as well as semi-empirical methods. The double zeta (DZ) ADF calculations show the best agreement for protons α, β, and methyl 5, while the best agreement for δ and methyl 1 is found in the triple zeta (TZ) calculation. It seems that the EPR specific basis sets and higher levels of theory do not improve the predictions in this case. The predicted anisotropic hyperfine tensors are given in tables 5-1 and 5-2, with the measured experimental data.

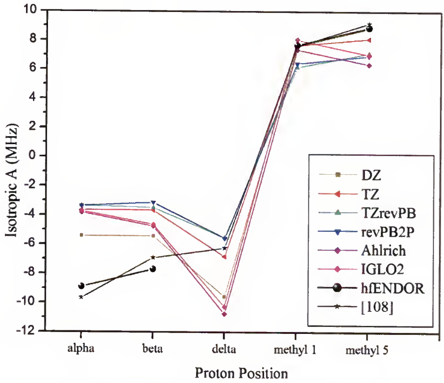

Figure 5-5 Theoretical and experimental isotropic hyperfine couplings for BChl *a* radical anion. The hf-ENDOR data points result from the averaged hyperfine tensor components of A_4 and A_5. Since the sign of the coupling constant is uncertain in ENDOR, these values have been added to this plot with both sign possibilities.

Table 5-1 Isotropic hyperfine coupling constants estimated with DFT and X-Band EPR for BChl *a* anion. DFT calculations employed a molecular geometry optimized with one THF molecule coordinated to Mg. The individual component of each methyl proton tensor has been averaged to anticipate the isotropic nature of a spinning methyl group on a tumbling molecule in solution.

Proton		ADF (DZ)	ADF (TZ)	ADF (TZ, revPB)	Neese (DZ, Ahlrich)	Neese (DZ, IGLOII)	Barone (EPRII)	Exp. [109]	hf-ENDOR
α	A_{iso}	-5.41	-3.65	-3.32	-3.81	-3.71	-3.84	-9.65	-8.9 ?
β	A_{iso}	-5.43	-3.65	-3.08	-4.75	-4.64	-4.76	-6.91	-7.7 ?
δ	A_{iso}	-9.55	-6.81	-5.52	-10.72	-10.25	-10.45	-6.23	
Methyl 1	A_1^{av}	6.53	6.64	5.99	6.26	6.93	7.39		
	A_2^{av}	7.01	7.10	6.06	6.65	7.34	7.84		
	A_3^{av}	8.48	9.35	0.75	9.24	9.96	10.36		
	A_{iso}^{av}	7.60	7.70	6.49	7.39	8.08	8.53	7.63	7.7 ?
Methyl 5	A_1^{av}	7.84	7.25	6.86	5.52	6.16	6.50		
	A_2^{av}	8.31	7.66	6.99	5.91	6.55	6.93		
	A_3^{av}	9.82	8.99	8.33	7.73	8.39	8.67		
	A_{iso}^{av}	8.81	8.12	7.14	6.39	7.03	7.36	9.19	8.9 ?

Table 5-2 Hyperfine tensor data, where $A_x = A_{dip} + A_{iso}$

Proton Position		ADF (DZ)	ADF (TZ)	ADF (TZ, revPB)	ADF (TZ, revPB -2p)	Neese (DZ, Ahlrich)	Neese (DZ, IGLOII)	Barone (EPRII)	hf-ENDOR
									A_5
α	A_1	-7.26	-5.31	-5.04	-5.14	-5.31	-5.23	-5.37	8.0 ?
	A_2	-6.73	-4.86	-4.53	-4.43	-5.03	-4.95	-5.09	9.2 ?
	A_3	-2.25	-0.78	-0.39	-0.50	-1.10	-0.96	-1.06	9.5 ?
									A_4
β	A_1	-7.37	-5.32	-4.73	-4.85	-6.63	-6.55	-6.67	6.6 ?
	A_2	-6.51	-1.50	-3.93	-3.83	-5.59	-5.48	-5.61	7.2 ?
	A_3	-2.42	-1.13	-0.57	-0.66	-2.02	-1.90	-2.01	9.2 ?
δ	A_1	-13.24	-10.53	-9.07	-9.27	-15.69	-15.20	-15.41	
	A_2	-11.12	-7.83	-6.56	-6.36	-11.80	-11.33	-11.59	
	A_3	-4.30	-2.06	-0.94	-1.12	-4.67	-4.22	-4.36	
Methyl									A_4
1	A_1	11.88	11.99	10.29	10.20	11.47	12.63	13.44	6.6 ?
	A_2	12.42	12.41	10.66	10.63	11.78	13.00	13.84	7.2 ?
	A_3	14.69	14.72	12.91	12.81	14.40	15.67	16.35	9.2 ?
	A_1	7.94	8.28	6.89	6.78	7.79	8.41	9.03	
	A_2	8.34	8.68	7.30	7.27	8.11	8.75	9.46	
	A_3	10.52	10.84	9.39	9.33	10.60	11.27	11.84	
	A_1	-0.25	-0.36	0.79	-0.80	-0.46	-0.25	-0.31	
	A_2	0.27	0.22	0.21	-0.20	0.05	0.26	0.23	
	A_3	0.26	2.50	0.20	1.95	2.74	2.95	2.89	
Methyl									A_5
5	A_1	12.83	11.49	10.00	9.88	8.83	9.74	10.28	8.0 ?
	A_2	13.34	11.88	10.40	10.35	9.23	10.16	10.75	9.2 ?
	A_3	15.43	13.68	12.15	12.09	11.00	11.96	12.41	9.5 ?
	A_1	11.28	10.93	9.55	9.42	8.39	9.27	9.79	
	A_2	11.72	11.35	9.98	9.93	8.82	9.71	10.29	
	A_3	13.86	13.12	11.70	11.64	10.56	11.48	11.92	
	A_1	-0.60	-0.67	1.03	-1.02	-0.65	-0.54	-0.59	
	A_2	-0.12	-0.26	0.59	-0.6	-0.33	-0.22	-0.27	
	A_3	0.16	0.16	1.13	1.13	1.64	1.73	1.67	

Bacteriopheophytin *a* Radical Anion

The high field EPR spectrum for the BPheo *a* radical anion is shown in figure 4-15, and the g-tensor data of repeated experiments are tabulated in table 4-4. The sample for each experiment was prepared in the same way, as described in chapter 3, but may vary in concentration since the yield of the reduction reaction is unknown. The g-values for this radical provide a unique distinction between the BPheo *a* and BChl *a* radical anions since the former has a more anisotropic g-tensor than the latter. BPheo *a* radical anion has $g_z = 2.002299 \pm 5\text{x}10^{-5}$, which is within experimental error of the free electron g-value, $g_e = 2.002319$. The proximity of g_z to g_e leads to the assumption that g_z is close to perpendicular to the conjugation plane (as mentioned in the BChl *a* radical anion discussion). Figure 5-6 shows the proposed orientation of **g** on the BPheo *a* structure.

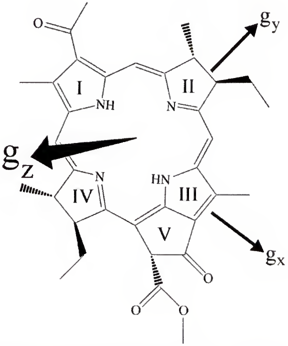

Figure 5-6 Molecular structure and atomic numbering of BPheo *a* with the estimated g-tensor orientation for BPheo *a* radical anion.

In order to fit the hf-EPR spectra, an anisotropic linewidth was used, which required a broader linewidth for g_z than for g_x and g_y. This result could originate from anisotropic hyperfine interactions, or from g-strain. Since the g_z orientation is more likely to have a distribution of solvent and intermolecular interactions, the g_z feature may become broadened, relative to the other components, as a result of a distribution of environments in the Z coordinate. Such interactions have been observed in bacterial reaction centers and quinone anion radicals in frozen solution and in single crystals [111-113]. The possible environmental affects on the g_z component will be influenced by the nature of the excited states of the radical. That is, since the unpaired electron density is located in the p_z orbitals of the carbon atoms, it is conceivable that environmental interactions, with other BPheo *a* radicals or solvent (THF) molecules, could broaden g_z. These interactions may be responsible for the poor fits along g_z on the hf-EPR spectra. This larger uncertainty in the simulations translates directly to the uncertainty of the g-tensor.

The values of g_x and g_y were measured to be $2.004459 \pm 5\text{x}10^{-5}$ and $2.003249 \pm 5\text{x}10^{-5}$ respectively. Spin-orbit interactions lead to the deviation of g_x and g_y from g_z, and this interaction is heavily weighted by the spin-orbit coupling constant (λ) of the nitrogen nuclei of rings II and IV. The net spin density on N_{II} and N_{IV} are indicated in figure 5-7 with arrows. Figure 5-7(a) is a plot of the spatial distribution of the neutral LUMO function of BPheo *a*. The molecular orientation in this figure is identical to figure 5-6. Figures 5-7(b) and 5-7(c) were generated by subtracting the alpha spin density from the beta spin density, which results in a net spin density plot, revealing only the nuclei with a high concentration of unpaired spin density. This net spin density determines the g-tensor orientation. From figure 5-2 the spin density appears to be concentrated along the Y axis of the molecular frame. This prediction resembles the BChl *a* anion predictions, which is believed to have a similar orientation of the g-tensor with g_x along the molecular Y axis between rings I and III.

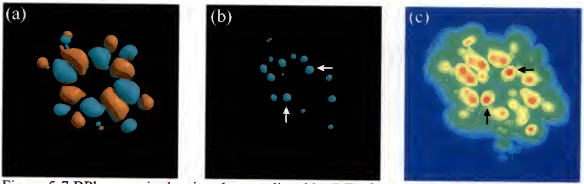

Figure 5-7 BPheo *a* spin density plots predicted by DFT for the (a) HOMO wavefunction, (b) net spin density (difference between the alpha and beta HOMO), (c) projection of the average net spin density distribution with increasing concentration from blue to red.

The BPheo *a* radical anion shows similar orientationally selected ENDOR spectra to BChl *a*, with subtle differences. This radical has been studied a bit more closely with theory and anisotropic hyperfine couplings have been predicted by O'Malley with the B3LYP level of theory [47,114]. The atomic numbering for this radical is shown on the structure in figure 5-8. The presented data show superscripts to indicate the literature values, and subscripts indexing the ENDOR transition number from the experimental spectra. The smallest splitting was fitted to a hyperfine tensor, $A_1 = [0.5, 0.5, 0.7]$ MHz (see figure 5-8 for the labeled hyperfine couplings). This tensor leads to an isotropic hyperfine coupling value of $A_{1(iso)} = 0.57$ MHz. O'Malley predicts the proton of the ring I nitrogen to give such a coupling, $A^{NH(iso)} = 0.50$ MHz, with a total hyperfine tensor, $A^{NH} = [2.8, 0.2, -1.5]$ MHz. The prediction of such a tensor does not necessarily conflict with

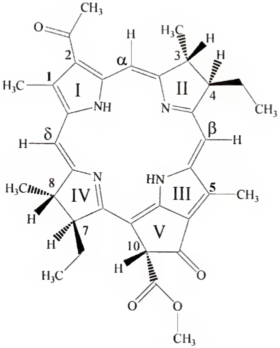

Figure 5-8 Molecular structure and atomic numbering of BPheo *a*.

the presented ENDOR data, but the superposition of many resonances with effective splittings between 0.5 MHz and 2.2 MHz complicate tensor assignments. The second set of ENDOR transitions are described by $A_2 = [0.7, 1.8, 1.8]$ MHz and $A_{2(iso)} = 1.43$ MHz. The features of this coupling likely result from the proton on carbon 8, which O'Malley predicts to have $A^8 = [-0.2, -1.3, -1.8]$ MHz, with $A^{8(iso)} = -1.1$ MHz. Again, the uncertainty in the experimental data increases at small hyperfine couplings, which may explain the difference in the first component of A^8 and A_2. The orientation of this tensor, relative to the g-tensor axes, may be assumed from the experimental ENDOR data. The A^8 splitting appears to be at a maximum at the edges of the powder pattern, at g_x and g_z, and at a minimum at g_y. This would indicate, assuming an axial tensor with $A_x < A_y = A_z$, that the A_x axis lies along g_y. This assumption puts A_y and A_z in the g_{xz} plane.

The third set of resolved ENDOR lines show somewhat isotropic behavior, with $A_3 = [2.0, 2.2, 2.0]$ MHz, which gives $A_{3(iso)} = 2.1$ MHz. O'Malley predicts similar behavior for the proton on carbon 3, giving $A^3 = [-1.3, -2.2, -2.5]$ and $A^{3(iso)} = -2.0$ MHz. This proton is bound to the ring II pyrrole and is not predicted to have much spin density [47,113]. However, the possibility exists that this feature in the ENDOR spectra is a superposition of several resonances from similar protons, such as those at positions 3, 4, and 7. These protons are positioned on opposing sides of the molecule (rings II and IV), which could mean that their A-tensors are approximately 180^o apart in their orientation relative to the g-frame. This assumption is made since the z-component of the A-tensor usually lies on the bond between the proton and the molecule, where the largest component of the A-tensor should result. O'Malley's predictions for the position 3, 4, and 7 protons show similar anisotropies and similar isotropic couplings with an average of $A_{iso(ave)} = 2.5$ MHz $\pm$ 0.5 MHz. The fourth and fifth couplings comprise the wings of the ENDOR spectra and show anisotropic behavior, with $A_4 = [8.5, 7.8, 7.5]$ MHz, and $A_5 = [9.1, 8.8, 8.3]$, with $A_{4(iso)} = 7.93$ MHz and $A_{5(iso)} = 8.73$ MHz. These resonances are most likely due to the methyl protons on positions 1 and 5. The X-band data predict an average, isotropic, methyl contribution of 8.4 MHz. Thus, it is plausible that the outer wings result from methyl proton resonance, since the high-field anisotropic values average to 8.33 MHz. This agreement is also in line with previous work at X-band, which similarly finds a value of 8.4 MHz [56]. Theoretical predictions for the methyl tensors seem to be much more anisotropic. O'Malley's predictions assume an average value for the methyl protons, which should not be the case here, since the ENDOR data were collected at 10 K. It is possible that the resolution of the couplings for these protons could be improved by measuring at higher temperatures. Above 100 K the methyl rotation should sufficiently average out the individual proton couplings.

Beyond the outer wings in the ENDOR spectra, a 13-15 MHz splitting seems to be present as shoulders on the wings, around A_5, and was fitted to $A_6 = [15, 15, 13]$ MHz. This region was not examined in all the spectra, but the feature is present in each of the wide scans shown in figure 4-20. A hyperfine coupling of this magnitude is predicted in O'Malley's calculations for the methine proton β where $A^{\beta} = [-3.4, -8.8, -12.1]$ MHz and $A^{\beta(iso)} = -8.1$ MHz [47]. For such a hyperfine tensor to exist, the ENDOR transitions must be very weak, or very broad since they are not obvious in the hf-ENDOR experiments presented here. A strongly anisotropic tensor such as this would result in ENDOR intensity between the outer wings (A_4) and the central feature of the ENDOR spectra (A_3) in figure 5-8. The lack of intensity in this region, in every ENDOR spectrum, seems to indicate that such an anisotropy does not exist, or is too broad and weak to be detected. However, the A_6 splitting could be due to methyl protons.

Measurement of the ENDOR at 10 K freezes out the methyl group rotation. In this case, the individual protons on each methyl group will have different orientations (i.e. different orientations of their A-tensor), as well as different hyperfine couplings. This scenario should add a pair of lines to the ENDOR spectra for each different proton, unless the lines are not fully resolved. According to theoretical estimations for BChl *a* radical anion, the closer a methyl proton is to being in the plane with the conjugation system, the smaller the total hyperfine interaction (shown in table 5-2). This behavior results from the nature of the spin density on this radical, which is present above and below the plane of conjugated carbon atoms. Since the isotropic couplings are an average of all the protons of a given methyl group, a negligible value for one of these protons results in above average values for the other two. In other words, if one of the methyl protons at 10 K has a negligible hyperfine coupling, the other two protons must have a coupling much larger than 8-9 MHz, which is the averaged methyl coupling. So, the 13-15 MHz splitting could be due to methyl protons that are out of the plane on methyl 1 or 5.

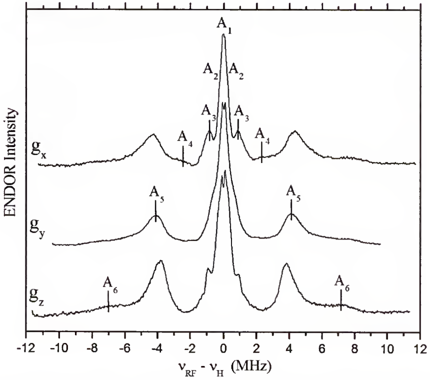

Figure 5-8 Hf-ENDOR spectra of BPheo *a* radical anion with labeled hyperfine couplings.

Table 5-3 Hyperfine tensor data for BChl *a* and BPheo *a* radical anions. The tensors were obtained by fitting the experimental ENDOR spectra using GENDOR [107]. All simulations used Euler angle $\phi = 90^o$.

Radical		Splitting A_1	A_2	A_3	A_4	A_5	A_6
BChl a^-	A_x	0.2	0.4	3.0	6.6	8.0	--
	A_y	0.2	0.85	3.0	7.2	9.2	--
	A_z	0.2	0.4	4.0	9.2	9.5	--
	A_{iso}	0.2	0.6	3.3	7.7	8.9	--
BPheo a^-	A_x	0.5	0.7	2.0	8.5	9.1	15.0
	A_y	0.5	1.8	2.2	7.8	8.8	15.0
	A_z	0.7	1.8	2.0	7.5	8.3	13.0
	A_{iso}	0.6	1.4	2.1	7.9	8.7	14.3

Bacteriochlorophyll *a* Radical Cation

BChl *a* is a versatile component of the bacterial reaction center of *Rb. sphaeroides* and has been the subject of much low-field EPR and ENDOR research [33-36,115]. This molecule helps collect solar energy by it's presence in the light harvesting complexes (LH1 and LH2), and is involved in the primary charge separation; the primary donor (D) is a dimer of BChl *a* molecules, and the first intermediate acceptor in the primary charge separation is likely to be a BChl *a* monomer. Essentially, the initial charge separation involves the interaction of the cationic (HOMO) and anionic (LUMO) states of BChl *a* molecules. The cationic species is a direct probe of the HOMO wavefunction, which is the first species created in the primary charge separation, D^+. Although the primary donor is a dimer of BChl *a* molecules, previous work has shown that the electronic structure of the dimer is highly asymmetric, and the g-values are too similar to distinguish between D^+ and BChl a^+ [33]. High-field studies on the primary donor, and monomeric BChl *a* cations have produced isotropic hyperfine coupling information, as well as g-tensor values ($\Delta g_{x-z} = 0.0011$) and orientations from single crystal experiments [33,35,74]. In addition to the small g-anisotropy of this radical, the hf-EPR measurements were complicated by the presence of g-strain. This is a broadening phenomenon that is proportional to the external field. As the resonance conditions of the experiment were increased from 0.35 T/9.5 GHz to 7 T/210 GHz, g-strain became more obvious and eventually broadened the powder pattern several hundred gauss at 210 GHz. This broadening effect could be circumvented by deuteration of the radical, but since this option was not immediately available, lower frequency measurements were pursued.

X-band proton and nitrogen hyperfine couplings have been published by others [116-119] and calculations have shown good agreement with experimental values [109]. According to Sinnecker et al, the electron density is concentrated on the beta protons of rings II and IV at positions 3, 4, 7, and 8 [109]. This finding is in contrast to the radical anion's spin density distribution, which is heavily localized on the alpha protons and the position 1 and 5 methyl groups. For the cation, these beta protons show isotropic hyperfine couplings of 11-16 MHz, while the alpha protons have much smaller couplings of 1-2 MHz [67,136]. Figure 5-9, contains plots of the spin density predicted with DFT calculations. The alpha HOMO level is shown in figure 5-9(a), while the more revealing plots for the hyperfine and g-tensor behavior are shown in 5-9(b) and 5-9(c). These images depict the predicted net spin density, which explains the hyperfine interactions and the origin of the g-tensor. Relative to BChl *a* radical anion, the cation shows a much more even distribution of spin density around all the pyrrole rings, especially on the nitrogen atoms. This observation could, in principle, explain the smaller g-anisotropy

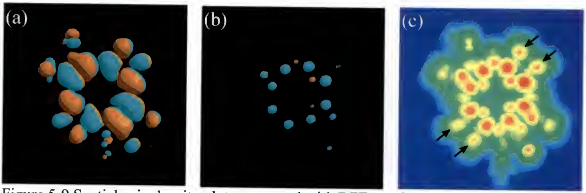

Figure 5-9 Spatial spin density plots generated with DFT predictions for BChl *a* radical cation. (a) The alpha HOMO wavefunction, (b) depicts the net spin density, and (c) is the average net spin density plot showing the increasing spin concentration of blue to red.

observed for the cation. The spin density appears to be similarly localized on each of the four pyrrole nitrogen atoms. This prediction has been experimentally justified with the hyperfine coupling measurements of the nitrogens, $A_N = 2.7$ MHz $\pm$ 0.5 MHz [108]. This even distribution of spin density should influence the deviation of g_x and g_y from g_z similarly. The carbonyl group on ring V also appears to have a substantial amount of net spin density, which adds to the spin-orbit coupling potential of the X dimension. But, since N_{II} and N_{IV} are directly linked to the conjugation system, the Y dimension may have more spin-orbit interaction due to nitrogen. The spin density for this radical seems to be concentrated between rings II and IV. High field studies have assigned a g-tensor orientation which aligns g_x with X and g_y with Y [33]. The BChl *a* radical anion, on the other hand, has spin density concentrated on rings I and III, which should orient the anion's g-tensor ~90° to the cation's g-tensor.

The W-band echo detected field sweep of BChl *a* radical cation in frozen solution shows little Zeeman resolution, indicating higher fields are necessary to obtain full orientation selection (shown in figure 4-23). However, the possibility of partial orientational selection was not abandoned and Davies and Mims ENDOR spectra were taken through the EPR line. Within experimental error, these ENDOR spectra show no anisotropic behavior. This result is not surprising, given the small g-anisotropy for this radical, $\Delta g_{x\text{-}z} = 0.0011$ [33]. The beta protons, at positions 3, 4, 7, and 8 show up weakly on the Davies spectra as wings at $A \cong 14$ MHz. The highly dipolar nature of this hyperfine interaction leads to very broad resonances which are unresolved. These ENDOR frequencies are also likely to be slightly different, which contributes to the lack of resolution. The position 1 and 5 methyl resonances are expected to be around 4.93 MHz and 9.62 MHz, while the β and δ proton contributions are expected around 1.30 MHz [67,109]. These numbers agree very well with the measured splittings of 1.15 MHz, 5.0 MHz, and 9.5 MHz. The invariance of these hyperfine couplings between the different ENDOR spectra indicates that the g-tensor resolution was insufficient to select orientations from the powder average.

So, the BChl *a* cation and anion seem to have very different spin density distributions, which lead to their very different spectroscopic behavior. The pulsed ENDOR experiments presented here confirm the known hyperfine data and contribute the knowledge that W-band provides insufficient Zeeman resolution for orientational selection. In order to conduct orientational selection experiments above W-band, deuterated samples may be needed.

Bacteriopheophytin *a* Radical Cation

X-band experiments performed on this cation yield an unresolved EPR line, which may be partially resolved at W-band, see figure 4-27. The W-band EPR line is broader than the X-band line, and is beginning to show some asymmetry on the low field side, possibly indicating spectral separation in the Zeeman orientations. However, the sharp feature at 33668 G may result from another radical species formed during the oxidation. The inaccuracy of the magnetic field at W-band prevents g-value determination of the features, which could help identify the radical. The similarity between the pulsed ENDOR spectra at each of these features, shown in figures 4-28 and 4-29, indicates the presence of only one type of radical. This cation has been partially characterized by J. Fajer at X-band using deuteration and theoretical techniques [120]. Fajer et al. report $g_{iso} = 2.0025$ for BPheo a^+, which is in agreement with this work, which finds $g_{iso} = 2.00253 \pm 4x10^{-5}$ at X-band. The measured hyperfine couplings from W-band ENDOR experiments are presented in table 4-3. It has been predicted with theory that rings II and IV carry most of the electron spin density, which leads to the largest hyperfine interactions [120]. However, the hyperfine couplings from the protons on these rings, 11-20 MHz, exceed the couplings measured here [120]. So the splittings observed in the W-band ENDOR experiments result from the methine and methyl protons.

The lack of orientational selection in these experiments prevents the determination of hyperfine tensor components, but the isotropic constants can be assigned. In light of the known assignments for BChl *a* radical cation, The 1.6-1.3 MHz coupling is assigned to the methine protons, β and δ. These protons produce 1.3 MHz coupling in BChl *a* radical cation [108,109]. The 3.1-3.6 MHz coupling could be due to the remaining methine proton, α, which shows a 2.35 MHz coupling in BChl *a* radical cation. This larger coupling is plausible considering the absence of the metal atom should distribute more electron density on the conjugated atoms. The 5.2 MHz coupling closely resembles the 4.93 MHz coupling for BChl *a* radical cation, which has been assigned to the position 1 methyl group. The position 5 methyl group shows a coupling of 9.62 MHz for BChl *a* cation, so the 7.7-8.7 MHz splitting is assumed to belong to the protons of this group.

High field EPR measurements on BPheo *a* radical cation were attempted with similar results to BChl *a* radical cation. The presence of g-strain prevented full resolution in the g-tensor, and thus, orientationally selected ENDOR experiments. The spectra measured here show that W-band does not provide sufficient Zeeman resolution to select individual orientations from the powder average. Deuteration could possibly improve on the information contained in W-band spectra, as was suggested for BChl *a* cation. But the measured isotropic couplings indicate a similar spin density distribution to BChl *a* radical cation, with slightly more density on the position 1 methyl and a slightly smaller density on the position 5 methyl. Also, the methine proton, α, seems to be more strongly coupled in BPheo *a* cation than in BChl *a* cation.

Chlorophyll Radical Anions

Fully resolved g-tensor measurements on the radical anions of Chl *a* and Chl *b* have been taken and are shown in figures 4-30 and 4-32, and the g-tensor data is tabulated in table 4-4. The magnitude and anisotropy of the g-tensors are similar between these two chlorophyll species. The g-tensor of doublet radicals is known to be very sensitive to the molecular structure of the radical [74,80,121,122], and intermolecular interactions [123]. The structural difference between these two chlorophylls amounts to a methyl group on carbon 3 for Chl *a*, where Chl *b* has an acetyl group. Zeeman resolution was achieved by 330 GHz, which seems to indicate the lack of g-strain, which has been demonstrated by the Chl a^+ [74,124]. Since the high field EPR experiments were done on frozen solutions, the principal g-tensor values were measured, but assignment of an orientation relative to the molecular frame requires additional methods. However, it is possible to make certain conclusions from the g-tensor data.

The proximity of the chlorophyll radical anions' g_z to the free electron value is expected since these species are conjugated π-radicals [125]. The Chl *a* radical anion showed $g_z = 2.002024 \pm 8\text{x}10^{-5}$, and for Chl *b* radical anion, $g_z = 2.001896 \pm 7\text{x}10^{-5}$. The values of g_z indicate the shift of the entire g-tensor between the two radicals. This shift is expected from the X-band experiments, where Δg_{iso}(Chl *a* – Chl *b*) = $1.8\text{x}10^{-4}$. The anisotropy between the principal components of **g** is similar between these two radicals, but the absolute value of **g** is shifted. This shift in the high field g-values (Δg_{ave}(Chl *a* – Chl *b*) = $1.14\text{x}10^{-4}$) exceeds the uncertainty in the field calibration standard ($\pm 5\text{x}10^{-5}$) and exceeds the expected shift of **g** due to intermolecular affects with THF or residual water (on the order of $1\text{x}10^{-4} \pm 5\text{x}10^{-5}$). These environmental effects would most likely affect the g_z component more than the other components of **g**, since the unpaired electron density occupies this dimension generated by the p_z atomic orbitals.

These two molecules differ in structure on carbon 3, where Chl *a* has a methyl group and Chl *b* has an acetyl group. If these functional groups have considerable spin density, then the presence and orientation of the acetyl group could heavily influence the value of the g-tensor. The presence of an oxygen atom can greatly affect the value and orientation of the g-tensor components, as has been shown on quinone radicals [ref]. However, the extent of the affect on the g-tensor is directly related to the amount of spin density localized on the oxygen, which appears to be quite small for the chlorophyll radical anions. The affect of the acetyl orientation on the g-tensor has been predicted using the BLYP level of DFT theory, on other photosynthetic ions, and can shift the g-tensor components by up to $17\text{x}10^{-4}$ [33,111]. The results presented here indicate that this functional group has a small affect on the total anisotropy of the g-tensor, since the difference in the total anisotropies is given by: $|\Delta g_{x\text{-}z}(\text{Chl}a - \text{Chl}b)| = 9\text{x}10^{-5}$. This difference in the g-anisotropy is on the order of the error in the g-tensor measurements, which is $5\text{x}10^{-5}$ to $1\text{x}10^{-4}$. Thus, the interaction of the acetyl group with the electron density seems to be negligible. If it is assumed that carbon 3 falls on the Y-axis of the molecular reference frame, the g-tensor component closest to this axis should be the most strongly affected by the presence and orientation of the acetyl group. But since the g-anisotropies are similar between the Chl *a* and Chl *b* radical anions, a g-tensor orientation cannot be assumed from this data.

Density functional estimations of the spin density on the Chl *a* radical anion predict the acetyl group to have negligible spin density [126]. This result is surprising considering that chlorin pigments, such as chlorophylls, have a conjugation system that extends to rings I, II, and III. This conjugation brings carbon 3 into an alpha position (on ring II), where it could possess considerable electron density. However, the negligible affect of the acetyl group on the g-tensor agrees with the experimental data and the theoretical predictions of Sinnecker [126] and O'Malley [127] who have calculated a negligible spin density on ring II. This result is in contrast to the bacterial anions, which are predicted to use the carbon 2 acetyl group in the primary electron transfer events [47,114]. This difference may indicate an evolution of a more specialized chlorophyll. That is, the electron density and chemically active groups lie along the X-axis (connecting rings I and III). In this case, the acetyl group on carbon 3 may not be directly involved in the charge separation chemistry.

The orientation of the g-tensor has been estimated for Chl *a* cation to have g_x connecting rings I and III, g_y connecting rings II and IV, and g_z approximately normal to the conjugation plane [33,74,113]. This orientation seems to follow the predicted spin density symmetry on the Chl *a* anion species as well, which maintains subtle differences from the cationic wavefunction, but maintains a higher concentration of spin density on rings I and III, and a relatively lower concentration on rings II and IV [121]. The orientation of the g-tensor has been shown theoretically to be very sensitive to the geometry of the radical [41,80]. The presence of g-strain impaired the g-tensor measurement of the cation, which led to the study of deuterated material [74]. This g-strain is a broadening phenomenon that increases the linewidth as the field is increased. The g-anisotropy for the Chl *a* radical anion exceeds that of its cationic counterpart, which most likely indicates a similar trend in spin density distribution to the bacterial ions. This distribution entails strongly coupled rings I and III, with a more symmetric distribution on all of the pyrrole nitrogens, $N_I - N_{IV}$.

The variation in experimental g-tensor data for Chl *a* can be rationalized through solvation effects. It is known that solvent ligation as well as aggregation between radicals and their neutral counterparts can affect the electronic structure of the radical species, which directly affects the g-tensor [79,112]. These effects are rooted in electronic interactions such as hydrogen bonding or π-π stacking (which are purely dipolar interactions). This additional dipolar interaction can account for shifts in the g-value on the order of 10^{-4} [113]. The presence of heavy atoms can increase the shift for such an interaction. The solvent for all the anion studies was tetrahydrofuran (C_4H_8O), which contains an oxygen atom that can serve as the fifth ligand to the central Mg atom in the chlorophylls. Although water was rigorously removed from the system (as described in chapter 3), the presence of residual water in the sample could promote aggressive hydrogen bonding and varied ligation to Mg. This interaction was observed as early as the 1970's to explain discrepancies in the isotropic g-value for BChl *a* radical anion [36]. The principal g-tensor components have a relatively small uncertainty ($7 \times 10^{-5} \pm 2 \times 10^{-5}$), but the possibility of environmental affects resulting from the nature of the sample increase this value (up to 2×10^{-4}). This level of uncertainty is still very small relative to the g-values and should not take away from the utility of these data.

The primary charge separation in photosystem I is still under investigation with optical and magnetic resonance experiments to study the radical species formed [128,129]. The primary acceptor, A_o, has been determined by crystallography to be a Chl *a* monomer [130], which takes on an electron during the primary charge separation. This charge separated state is very short-lived, making it difficult to study *in vivo*. Knowledge of the g-values and anisotropies of the Chl *a* radical anion could be useful in one of two ways: the identity of an *in vivo* radical may be determined by its g-tensor, or the extent of the interaction between the radical and the environment may be assessed. This g-tensor data on the individual anion species should allow further identification of the radical formed during the primary charge separation, A_o, which has never been successfully measured with high field EPR. This data also provides a reference frame for the measurement of environmental interactions within the RC. It may be possible to estimate the extent of protein interactions by the difference between the *in vivo* and *in vitro* g-tensor values. High-field EPR [72] and DFT [49,83] methods have been used to investigate protein interactions with organic radicals. The presence of hydrogens on the chlorophyll structure allows hydrogen-bonding possibilities to the surrounding proteins, which could affect the energetics of the radical species.

Due to the relatively small g-tensor anisotropy ($\sim 10^{-4}$), as well as from the predicted atomic spin densities [127], that the oxygen and nitrogen atoms have a relatively small concentration of electron density. The uncertainty in the g_z component seems to be much larger than the uncertainty in g_x or g_y. This could result from the dipolar solvent ligation that is sterically limited to the direction of g_z. This ligation should be prominent in the Mg containing pigments, and thus could explain the heightened variation of the g_z component for the metallated pigments. The pheophytin radicals were not measured here, but the heightened g_z broadening is present in the bacterial pigments between BChl *a* and BPheo *a* radical anions. It must be disclosed that ligation along g_z does not guarantee that this component will be most effected by the interaction. However, since the spin density is largely localized in the p_z orbitals, g_z is likely to be more affected by electrostatic interactions along this dimension than g_x or g_y.

CHAPTER 6
CONCLUSIONS

The high field EPR data report the first full characterization of the electronic Zeeman interaction for the radical anions of BChl *a*, BPheo *a*, Chl *a*, and Chl *b* (shown in table 6-1). The BChl *a* and BPheo *a* radical cations showed unresolved, g-strain broadened EPR spectra at 240 GHz, which limited study to 95 GHz. At this frequency, no orientation selection was achieved, which prevented g and A-tensor measurement. The high field EPR on the radical anions estimates the nature of the electron density and also firms the differences between the radical anion species studied. The bacterial pigments show that the presence of the central Mg atom affects g_{ave} (g_{iso}) more than the g-anisotropy, $\Delta g_{x\text{-}z}$. However, Δg is a more reliable experimental signature for any radical, since the magnitude of g_{iso} is limited by the quality of the field standard. The orientation of the g-tensor appears to be similar between all the radical anions, which have an electron spin density localized on rings II and IV. This result is not surprising considering the species' structural similarities. Also, the spin density on the carbon and hydrogen atoms, rather than the nitrogen and oxygen atoms, dictates the g-tensor orientation. This behavior is seen in the radical cations as well, where a much more symmetric distribution of spin density results in a much smaller g-anisotropy. Further work should be done to measure the radical cations' g-tensors, and ultimately A-tensors with high field ENDOR.

These experiments could also be extended to study Chl *a* and Chl *b*, and possibly Pheo *a* and Pheo *b* radical anions and cations. The exclusive presence of the *a* derivatives in plant reaction centers merits the investigation of the differences between the *a* and *b* derivatives. In light of the g-anisotropy observed for Chl *a* and Chl *b* radical anions, the high field ENDOR experiments should be straightforward and similar to the procedures presented here for BChl *a* and BPheo *a* radical anions. The study of the cations will likely be less straightforward since deuteration would enhance the g-tensor resolution, but would complicate ENDOR measurements. If selective deuteration were available and precise, this technique would be ideally suited for these experiments.

Table 6-1 Radical anion g-values measured with high field EPR. These values correspond to the high field EPR spectra shown in chapter 4 and are the most reliable of the experimental data for each species. Reliability was determined by the quality of the fitting, which is indicated by the experimental error.

Sample	g_{xx}	g_{yy}	g_{zz}	$(g_{xx}-g_{yy})$	$(g_{yy}-g_{zz})$	Microwave Frequency (GHz)
Bacteriochlorophyll *a* $^{-}$	2.004257 ^{a}	2.003150 ^{a}	2.002513 ^{a}	0.001107	0.000637	210.37
Bacteriopheophytin *a* $^{-}$	2.004459 ^{a}	2.003249 ^{a}	2.002299 ^{a}	0.001210	0.000950	326.13
Chlorophyll *a* $^{-}$	2.004012 ^{a}	2.002912 ^{a}	2.002027 ^{d}	0.001100	0.000885	326.11
Chlorophyll *b* $^{-}$	2.003964 ^{b}	2.002779 ^{b}	2.001896 ^{c}	0.001185	0.000883	326.13

The superscripts a-f denote the experimental error in that measurement: a = 5×10^{-5}, b = 6×10^{-5}, c = 7×10^{-5}, d = 8×10^{-5}.

The high field ENDOR spectra provide the first experimental measurement of the anisotropic hyperfine interactions for BChl *a* and BPheo *a* radical anions. This data provides experimental estimates of the hyperfine tensors and their orientations relative to g. The resolution of these ENDOR spectra is limited by the ENDOR linewidth and similarity of the hyperfine splittings. Out of the 12-16 possible couplings, 5-6 are observable. Granted, 7-9 of these expected couplings have $A_{iso} < 2$ MHz. The linewidths of the ENDOR transitions ranged from 0.2 MHz to 2 MHz. Such broadening may result from the distribution of molecular orientations, which was accounted for using gaussian lineshapes in the fitting procedures. Regardless, the high field ENDOR spectra present orientationally selected data, which provides experimental data for parameters that have only been theoretically predicted in the past. Although quantitation of all hyperfine tensors was complicated by poor resolution between transitions occurring at similar ENDOR frequencies, estimations of the tensor components and trends in the splitting were obtained. The largest splittings, A_4 and A_5 for BChl *a*, and A_5 and A_6 for BPheo *a*, are tentatively assigned to the methyl protons of positions 1 and 5 (shown in table 6-2). These tensor predictions may be inaccurate due to the overlap of several lines. For example, the outer band of the BChl *a* ENDOR spectra (figure 5-4) is predicted to result from two couplings, A_4 and A_5. The BPheo *a* radical anion is expected to behave similarly, but this outer band is totally unresolved, thus limiting the assignment of an A-tensor (figure 5-9). The methine protons show similar average hyperfine couplings, but are predicted by DFT to show larger anisotropy than the methyl protons. This assignment may be investigated further by examining the temperature dependence of the ENDOR spectra. This rotation would average out the individual methyl proton interactions, which should sharpen the ENDOR lines resulting from methyl protons. Also, partial deuteration could help determine the nature of the hyperfine interactions by removing the ENDOR lines of the isotopically substituted protons from the spectra.

The presented high field ENDOR experiments are truly groundbreaking and demonstrate the possibility of measuring hyperfine tensors in frozen solution, despite the

Table 6-2 Experimental hyperfine data for BChl *a* and BPheo *a* radical anions.

Proton		BChl *a* Anion			BPheo *a* Anion		
		X-band Data [109]	DFT Calcs. [A.Angerhofer]	hf-ENDOR Data	X-band Data [109]	DFT Calcs. [47]	hf-ENDOR Data
Methyl 1	A_1	--	6.64	6.6	--	8.0	8.5
	A_2	--	7.31	7.2	--	6.0	7.8
	A_3	--	9.35	9.2	--	5.5	7.5
	A_{iso}	7.63	7.70	7.7	7.10	6.5	7.9
Methyl 5	A_1	--	7.25	8.0	--	12.0	9.1
	A_2	--	7.66	9.2	--	9.7	8.8
	A_3	--	8.99	9.5	--	9.1	8.3
	A_{iso}	9.19	8.12	8.9	8.32	10.2	8.7

small Zeeman and hyperfine anisotropy of doublet, π-radicals with relatively weak spin-orbit and hyperfine interactions. Knowledge of these g and A-tensors should be immediately useful for *in vivo* studies. The radicals formed during the primary charge separation may be identified by their electronic signature, which has been approximated in this work *in vitro*. The protein subunits of the reaction center could influence the *in vitro* signature through electrostatic interactions such as H-bonding. Such interaction may complicate the *in vivo* identification of the radical species, but at the same time may be useful in studying the environmental influence on the electronic structure. Single-crystal measurements may provide fully resolved hyperfine tensor information since the dominant broadening affect in these ENDOR spectra appears to arise from the distribution of environments and geometries of the radicals in frozen solution. Such affects would be eliminated in a single-crystal sample, but preparing such a sample is currently not routine. However, crystallization of the entire reaction center is possible and produces a highly ordered system due to the protein structure [33,73].

APPENDIX
ABBREVIATIONS AND CONSTANTS

Abbreviation	Definition
A	Hyperfine coupling tensor
A_{mn}	Component of the hyperfine coupling tensor
ADF	Amsterdam Density Functional Theory
β_e	Bohr Magneton: 9.27402×10^{-24} JT^{-1}
β_N	Nuclear Magneton: $5.0507866 \times 10^{-27}$ JT^{-1}
B_A	Bacteriochlorophyll molecule on A-branch of bacterial RC
B_o	Static magnetic field
B_1	Magnetic component of microwave radiation
B_2	Magnetic component of radiofrequency radiation
BChl *a*	Bacteriochlorophyll *a*
BPheo *a*	Bacteriopheophytin *a*
Chl *a*	Chlorophyll *a*
Chl *b*	Chlorophyll *b*
cw	Continuous Wave
D	Primary Donor
DFT	Density Functional Theory
DOUBLET	Simulation program used to fit the experimental EPR data
EMR	Electron Magnetic Resonance
ENDOR	Electron Nuclear DOuble Resonance
EPR	Electron Paramagnetic Resonance
ESR	Electron Spin Resonance
ESEEM	Electron Spin Echo Envelope Modulation
FFT	Fast Fourier Transform
Φ_A	Bacteriopheophytin molecule on A-branch of RC
g	g-tensor
g_{ave}	Average g-value: $(g_x+g_y+g_z)/3$
g_e	Free electron g-value: 2.002319304386(20) [76]
g_{iso}	Isotropic g-value
g_{mn}	Component of the g-tensor
GENDOR	Simulation program used to fit the high field ENDOR data
h	Planck's constant: $6.6260755(40) \times 10^{-34}$ Js
H	Hamiltonian operator
hfc	Hyperfine coupling constant
HOMO	Highest Occupied Molecular Orbital (of neutral)
I	Nuclear spin moment
L	Orbital angular momentum
LUMO	Lowest Unoccupied Molecular Orbital (of neutral)

$\mathbf{M}$	Bulk spin magnetization
M_S	Projection of electron spin moment on quantization axis
MO	Molecular orbital
ν_H	Proton Larmor frequency
ν_{RF}	RF frequency
NHMFL	National High Magnetic Field Laboratory
NMR	Nuclear Magnetic Resonance
μ_B	Bohr magneton: $9.2740154(31) \times 10^{-24}$ JT^{-1}
PS I	Photosystem I
PS II	Photosystem II
Q_A	Quinone acceptor on A-branch of bacterial RC
RC	Photosynthetic Reaction Center
$\mathbf{S}$	Electron spin angular momentum
UV-Vis	UltraViolet – Visible absorption spectroscopy
W-band	Naming convention for ~95 GHz
X-band	Naming convention for ~9.5 GHz

LIST OF REFERENCES

1 R. Clayton. "Primary Processes in Bacterial Photosynthesis" *Annual Reviews of Biophysics and Bioengineering* **1973** *2* 131

2 R. Clayton. "Physical Mechanisms in Photosynthesis: Past Elucidations and Current Problems" *PNAS U.S.A.* **1972** *69* 44

3 W. Parson. "Bacterial Photosynthesis" *Annual Reviews in Microbiology* **1974** *28* 41

4 X. Jordanides, G. Scholes, G. Fleming. "The Mechanism of Energy Transfer in the Bacterial Photosynthetic Reaction Center" *J. Phys. Chem. B* **2001** *105* 1652

5 K. M"obius. "Primary Processes in Photosynthesis: What Do We Learn from High Field EPR Spectroscopy?" *Chem. Soc. Rev.* **2000** *29* 129

6 G. Feher, P. Allen, M. Okamura, D. Rees. "Structure and Function of Bacterial Photosynthetic Reaction Centres" *Nature* **1989** *339* 111

7 R. Clayton. *Photosynthesis* Cambridge University Press, New York: 1980

8 L. Stryer. *Biochemistry* W. H. Freeman and Company, New York: 1981 p432

9 A. Wild, R. Ball. *Photosynthetic Unit and Photosystems* Blackhuys Publishers, Leiden: 1997 p.163

10 J. Deisenhofer, O. Epp, K. Miki, R. Huber, H. Michel. "X-Ray Structure Analysis of a Membrane Protein Complex: Electron Density Map at 3 A Resolution and a Model of the Chromophores of the Reaction Center from *Rhodopseudomonas viridis*" *Journal of Molecular Biology* **1984** *180* 385

11 J. Deisenhofer, O. Epp, K. Miki, R. Huber, H. Michel. "Structure of the Protein Subunits in the Photosynthetic Reaction Centre of *Rhodopseudomonas viridis* at 3 A Resolution" *Nature* **1985** *318* 618

12 H. Michel, O. Epp, J. Deisenhofer. "Pigment Protien Interactions in the Photosynthetic Reaction Center from *Rhodopseudomonas Viridis*." *EMBO Journal* **1986** *5* 2445

13 J. Allen, G. Feher, T. Yeates, D. Rees, J. Deisenhofer, H. Michel, R. Huber. "Structural Homology of Reaction Centers from *Rhodopseudomonas-sphaeroides* and *Rhodopseudomonas-viridis* as Determined by X-Ray Diffraction" *PNAS USA* **1986** *83* 8589

14 (a)A. Zouni, H. T. Witt, J. Kern, P. Fromme, N. Krauss, W. Saenger, P. Orth. "Crystal Structure of Photosystem II from *Synechococcus elongatus* at 3.8 Angstrom Resolution." *Nature* **2001** *409* 739 (b) P. Fromme, P. Jordan, N. Kraub. "Structure of Photosystem I" *BBA* **2001** *1507* 5

15 P. Jordan, P. Fromme, H.T. Witt, O. Klukas, W. Saenger, N. Krauss. "Three Dimensional Structure of Cyanobacteriul Photosystem I at 2.5 Angstrom Resolution." *Nature* **2001** *411* 909

16 B. Commoner, J. Heise, J. Townsend. "Light-Induced Paramagnetism in Chloroplasts" *PNAS U.S.A.* **1956** *42* 710

17 W. Parson, R. Cogdell. "The Primary Photochemical Reaction of Bacterial Photosynthesis" *BBA* **1975** *416* 105

18 A. Frenkel. "Multiplicity of Electron Transport Reactions in Bacterial Photosynthesis" *Biological Reviews* **1970** *45* 569

19 D. Borg, J. Fajer, R. Felton, D. Dolphin. "The Pi-Cation Radical of Chlorophyll *a*" *PNAS U.S.A.* **1970** *67* 813

20 J. Norris, R. Uphaus, H. Crespi, J. Katz. "Electron Spin Resonance of Chlorophyll and the Origin of Signal I in Photosynthesis" *PNAS U.S.A.* **1971** *68* 625

21 L. Slooten. "Reaction Center Preparations of *Rhodopseudomonas Spheroides*: Energy Transfer and Structure" *BBA* **1972** *256* 452

22 M. Calvin, G. Androes. "Primary Quantum Conversion in Photosynthesis" *Science* **1962** *138* 867

23 E. Weaver. "Electron Paramagnetic Resonance Signal Produced by Ferricyanide in Photosynthetic Plant Materials" *BBA* **1968** *162* 286

24 L. Duysens, W. Huiskamp, J. Vos, J. van der Hart. "Reversible Changes in Bacteriochlorophyll in Purple Bacteria Upon Illumination" *BBA* **1956** *19* 188

25 R. Felton, G. Sherman, H. Linschitz. Formation of Phase Test Intermediate of Chlorophyll by Electrolytic Reduction" *Nature* **1964** *203* 637

26 J.R. Norris, R.A. Uphaus, H.L. Crespi, J.J. Katz. "Electron Spin Resonance of Chorophyll and the Origin of Signal I in Photosynthesis" *PNAS USA* **1971** *68* 625

27 J.D. McElroy, G. Feher, D.C. Mauzerall. "Characterization of Primary Reactants in Bacterial Photosynthesis. I. Comparison of the Light Induced EPR Signal (g = 2.0026) with that of a Bacteriochlorophyll Radical" *BBA* **1972** *267* 363

28 G. Feher, A.J. Hoff, R.A. Isaacson, L.C. Ackerson. "ENDOR Experiments on Chlorophyll and Bacteriochlorophyll *in vitro* and in Photosynthetic Unit" *Annals of the NY Academy of Sciences* **1975** *244* 239

29 J.R. Norris, H. Scheer, J.J. Katz. "Models for Antenna and Reaction Center Chlorophylls" *Annals of the NY Academy of Sciences* **1975** *244* 260

30 W. Parson. "The Role of P^{870} in Bacterial Photosynthesis" *BBA* **1968** *153* 248

31 J. McElroy, G. Feher, D. Mauzerall. "Characterization of Primary Reactants in Bacterial Photosynthesis" *BBA* **1972** *267* 363

32 J. Warden, J. Bolton. "Simultaneous Optical and Electron Spin Resonance Detection of the Primary Photoproduct P700 in Green Plant Photosynthesis" *JACS* **1972** *94* 4351

33 M. Plato, K. M"obius. "Structural Characterization of the Primary Donor in Photosynthetic Bacteria by its Electronic g-Tensor." *Chemical Physics* **1995** *197* 289

34 H. K"ass, W. Lubitz. "Evaluation of 2D-ESEEM data of ^{15}N-Labeled Radical Cations of the Primary Donor P_{700} in Photosystem I and Chlorophyll *a*" *Chemical Physics Letters* **1996** *251* 193

35 F. Lendzian, M. Huber, R.A. Isaacson, B. Endeward, M. Plato, B. Bonigk, K. M"obius, W. Lubitz, G. Feher. "The Electronic Structure of the Primary Cation Radical in *Rhodobacter sphaeroides* R-26: ENDOR and TRIPLE Resoanance Studies in Single Crystals of Reaction Centers" *BBA* **1993** *1183* 139

36 H. Levanon, K. M"obius, "Advanced EPR Spectroscopy on Electron Transfer Processes in Photosynthesis and Biomimetic Model Systems" *Annual Review Biophysics Biomolecular Structure*, **1997** *26* 495

37 G.A. Peschek. "Phylogeny of Photosynthesis and the Evolution of Electron Transport: The Bioenergetic Backbone." *Photosynthetica* **1981** *15* 543

38 M. Blomberg, E. Siegbahn, G. Babcock. "Modelling Electron Transfer in Biochemistry: A Quantum Chemical Study of Charge Separation in *Rhodobacter sphaeroides* and Photosystem II" *JACS* **1998** *120* 8812

39 H. Michel, J. Deisenhofer. "Relevance of the Photosynthetic Reaction Center from Purple Bacteria to the Structure of Photosystem II" *Biochemistry* **1988** *27*

40 J. Deisenhofer, H. Michel. "The Photosynthetic Reaction Center from the Purple Bacterium Rhodopseudomonas Viridis." *EMBO Journal* **1989** *8* 2149

41 M. Engstr"om, O. Vahtras, H. Agren. "Hartree-Fock Linear Response Calculations of g-Tensors of Substituted Benzene Radicals" *Chemical Physics* **1999** *243* 263

42 R. Bittl, E. Schlodder, I. Geisenheimer, W. Lubitz, R. Cogdell. "Transient EPR and Absorption Studies of Carotenoid Triplet Formation in Purple Bacteria Antenna Complexes." *Journal of Physical Chemistry* **2001** *105* 5525

43 D. Kohl, J. Townsend, B. Commoner, H. Crespi, R. Dougherty, J. Katz. "Effects of Isotopic Substitution on Electron Spin Resonance Signals in Photosynthetic Organisms" *Nature* **1965** *206* 1105

44 J.P. Allen, G. Feher, T.O. Yeates, H. Komiya, D. Rees. "Structure of the Reaction Center of *Rhodobacter sphaeroides* R-26: The Cofactors" *PNAS USA* **1987** *84* 5730

45 A. de Winter, S. Boxer. "The Mechanism of Triplet Energy Transfer from the Special Pair to the Carotenoid in Bacterial Photosynthetic Reaction Centers" *J. Phys. Chem. B* **1999** *103* 8786

46 J. Roberts, D. Holten, C. Kirmaier. "Primary events in photosynthetic reaction centers with multiple mutations near the photoactive electron carriers" *J. Phys. Chem. B* **2001** *105* 5575

47 P. O'Malley. "The Electronic Structure of the Bacteriopheophytin *a* Anion Radical, in Vivo" *JACS* **1999** *121* 3185

48 P. Loach, G. Androes, A. Maksim, L. Calvin. "Variation in Electron Paramagnetic Resonance Signals of Photosynthetic Systems with the Redox Level of Their Environment" *Photochemistry and Photobiology* **1963** *2* 443

49 P. O'Malley. "Hybrid Density Functional Studies of Pheophytin Anion Radicals: Implications for Initial Electron Transfer in Photosynthetic Reaction Centers" *Journal of Physical Chemistry* **2000** *104* 2176

50 S. Schenkl, S. Sporlein, F. M"uh, H. Witt, W. Lubitz, W. Zinth, J. Wachtveitl. "Selective Pertubration of the Second Electron Transfer Step in Mutant Bacterial Reaction Centers" *BBA* **2002** *1554* 36

51 J. Hughes, M. Hutter, J. Reimers, N. Hush. "Modeling the Bacterial Photosynthetic Reaction Center. 4. The Structural, Electrochemical, and Hydrogen-Bonding Properties of 22 Mutants of *Rhodobacter sphaeroides*" *JACS* **2001** *123* 8550

52 M. Bixon, J. Jortner, M. Michel-Beyerle, A. Ogrodnik, W. Lersch. "The Role of the Accessory Bacteriochlorophyll in Reaction Centers of Photosynthetic Bacteria: Intermediate Acceptor in the Primary Electron Transfer?" *Chemical Physics Letters* **1987** *140* 626

53 K. Kaufmann, P. Dutton, T. Netzel, J. Leigh, P. Rentzepis. "Picosecond Kinetics of Events Leading to Reaction Center Bacteriochlorophyll Oxidation" *Science* **1975** *188* 1301

54 M. Rockley, M. Windsor, R. Cogdell, W. Parson. "Picosecond Detection of an Intermediate in the Photochemical Reaction of Bacterial Photosynthesis" *PNAS U.S.A* **1975** *72* 2251

55 J. Fajer, D. Brune, M. Davis, A. Forman, L. D. Spaulding. "Primary Charge Separation in Bacterial Photosynthesis: Oxidized Chlorophylls and Reduced Pheophytin" *PNAS U.S.A* **1975** *72* 4956

56 J. Fajer, A. Forman, M. Davis, L. Spaulding, D. Brune, R. Felton. "Anion Radicals of Bacteriochlorophyll *a* and Bacteriopheophytin *a*. Electron Spin Resonance and Electron Nuclear Double Resonance Studies" *JACS* **1977** *99* 4134

57 D. Tiede, R. Prince, G. Reed, P. Dutton. "EPR Properties of the Electron Carrier Intermediate Between the Reaction Center Bacteriochlorophylls and the Primary Acceptor in *Chromatium Vinosum*" *FEBS Letters* **1976** *65* 301

58 J. Fajer, D.C. Brune, M.S. Davis, A. Forman, L.D. Spaulding. "Primary Charge Separation in Bacterial Photosynthesis: Oxidized Chlorophylls and Reduced Pheophytin" *PNAS USA* **1975** *72* 4956

59 B. King, T. McAnaney, A. de Winter, S. Boxer. "Excited State Energy Transfer Pathways in Photosynthetic Reaction Centers. Ultrafast Emission from the Monomeric Bacteriochlorophylls" *J. Phys. Chem. B* **2000** *104* 8895

60 A. Ogrodnik, N. Remy-Richter, M. Michel-Beyerle. "Observation of Activationless Recombination in Reaction Centers of R. Sphaeroides. A New Key to the Primary Electron-Transfer Mechanism" *Chemical Physics Letters* **1987** *135* 576.

61 T. Artl, M. Bibikova, H. Penzkofer, D. Oesterhelt, W. Zinth. "Strong Acceleration of Primary Photosynthetic Electron Transfer in a Mutated Reaction Center of *Rhodopseudomonas viridis*" *Journal of Physical Chemistry* **1996** *100* 12060

62 J.-L. Martin, J. Breton, A.J. Hoff, A. Mingus, A. Antonetti. "Femtosecond Spectroscopy of Electron Transfer in the Reaction Center of the Photosynthetic Bacterium Rhodopseudomonas sphaeroides R-26: Direct Electron Transfer from the Dimeric Bacteriochlorophyll Primary Donor to the Bacteriopheophytin Acceptor with a Time Constant of 2.8 ± 0.2 psec" *PNAS USA* **1986** *83* 957

63 J. Breton, J.-L. Martin, J. Petrich, A. Mingus, A. Antonetti. "The absence of a spectroscopically resolved intermediate state P^+B^- in bacterial photosynthesis" *FEBS Letters* **1986** *209* 37

64 J. Breton, J.-L. Martin, A. Mingus, A. Antonetti, A. Orszag. "Femtosecond Spectroscopy of Excitation Energy Transfer and Initial Charge Separation in the Reaction Center os the Photosynthetic Bacterium *Rhodopseudomonas viridis*" *PNAS USA* **1986** *83* 5121

65 P. Dutton, K. Kaufmann, B. Chance, P. Rentzepis. "Picosecond Kinetics of the 1250 nm Band of the *RPS. Sphaeroides* Reaction Center: The Nature of the Primary Photochemical Intermediary State" *FEBS Letters* **1975** *60* 275

66 U. Till, B. Klenina, I. Proskuryakov, A. Hoff, P. Hore. "Recombination Dynamics and EPR Spectra of the Primary Radical Pair in Bacterial Photosynthetic Reaction Centers with Blocked Electron Transfer to the Primary Acceptor" *J. Phys. Chem. B* **1997** *101* 10939

67 A. Hoff, J. Amesz. *Chlorophylls* CRC Press: Boca Raton 1991 pp. 723-738 Ed. Hugo Scheer

68 R.A. Marcus, N. Sutin. "Electron Transfers in Chemistry and Biology" *BBA* **1985** *811* 265

69 J. Weil, J. Wertz, J. Bolton. *Electron Spin Resonance: Elementary Theory and Practical Applications* Wiley and Sons, Inc, New York. 1994

70 A. Hoff. *Advanced EPR: Applications in Biology and Biochemistry* Elsevier, New York 1989

71 G. Feher. "Observation of Nuclear Magnetic Resonance via the Electron Spin Resonance Line." *Physical Review* **1956** *103* 834

72 S. Un, M. Atta, M. Fontecave, A. W. Rutherford. "g-Values as a Probe of the Local Protein Environment: High Field EPR of Tyrosyl Radicals in Ribonucleotide Reductase and Photosystem II" *JACS* **1995** *117* 10713

73 M. Huber, J. T"orring "High-Field EPR on the Primary Electron Donor Cation Radical in Single Crystals of Heterodimer Mutant Reaction Centers of Photosynthetic Bacteria – First Characterization of the g-Tensor." *Chemical Physics* **1995** *194* 379

74 P. Bratt, O. Poluektov, M. Thurnauer, J. Krzystek, L-C. Brunel, J. Schrier, Y-W. Hsiao, M. Zerner, A. Angerhofer. "The g-Factor Anisotropy of Plant Chlorophyll $a^{+\cdot}$" *Journal of Physical Chemistry B* **2000** *104* 6973

75 M. Kn"upling, J. T"orring, S. Un. "The Relationship Between the Molecular Structure of Semiquinone Radicals and their g-Values." *Chemical Physics* **1997** *219* 291

76 J. Wertz, J. Bolton. *Electron Spin Resonance: Elementary Theory and Practical Applications* Chapman and Hall, New York 1986

77 A. J. Stone. "Gauge Invariance of the g-Tensor" *Proceedings of the Royal Society A* **1963** *271* 424

78 M. Pryce. "A Modified Perturbation Procedure for a Problem in Paramagnetism" *Proceedings of the Physical Society A* **1950** *63* 25

79 J.T. T"orring, S. Un, M. Kn"upling, M. Plato, K. M"obius. "On the Calculation of g-Tensors of Organic Radicals." *Journal of Chemical Physics* **1997** *107* 3905

80 Y.-W. Hsiao, M. Zerner. "Calculating ESR g-Tensors of Doublet Radicals by the Semiemperical INDO/S Method" *International Journal of Quantum Chemistry* **1999** *75* 577

81 M. Mustafaev, P. Schastnev. "Quantum-Chemical Analysis of the Effect of Geometrical and Electronic Factors on the G-Tensor of Nitroxyl Radicals" *Journal of Structural Chemistry* **1989** *30* 582

82 P. Zandstra. "Solvent Effects on the Spin-Orbit Coupling on Semiquinone Ion" *Journal of Chemical Physics* **1964** *41* 3655

83 M. Kaupp, C. Remenyl, J. Vaara, O. Malkina, V. Malkin. "Density Functional Calculations of Electronic g-Tensors for Semiquinone Radical Anions. The Role of Hydrogen Bonding and Substituent Effects" *JACS* **2002** *124* 2709

84 G. Feher. "Electron Spin Resonance Experiments on Donors in Silicon .1. Electronic Structure of Donors by the Electron Nuclear Double Resonance Technique" *Physical Review* **1959** *114* 1219

85 E. Hahn. "Spin Echos" *Physical Review* **1950** *109* 1867

86 G. Hurst, T. Henderson, R. Kreilick. "Angle-Selected ENDOR Spectroscopy. 1. Theoretical Interpretation of ENDOR Shifts from Randomly Orientated Transition Metal Complexes" *JACS* **1985** *107* 7294

87 A. Shubin, S. Dikanov. "Determination of Hyperfine Tensor Components from Nuclear Frequencies at Canonical Orientations of the g-Tensor" *Journal of Magnetic Resonance* **2002** *155* 100

88 T. Henderson, G. Hurst, R. Kreilick. "Angle-Selected ENDOR Spectroscopy. 2. Determination of Proton Coordinates from a Polycrystalline Sample of Bis(2,4-pentanedionato)copper(II)" *JACS* **1985** *107* 7299

89 A. True, M. Nelson, R. Venters, W. Orme-Johnson, B. Hoffman. "^{57}Fe Hyperfine Coupling Tensors of the FeMo Cluster in *Aztobacter vinelandii* MoFe Protein: Determination by Polycrystalline ENDOR Spectroscopy" *JACS* **1988** *110* 1935

90 D. Attanasio. "Structural Information from Powder ENDOR Spectroscopy" *J. Chem. Soc. Faraday Transactions* **1989** *85* 3927

91 C. Gebner, M. Stein, S. Albrecht, W. Lubitz. "Orientation Selected ENDOR of the Active Center in *Chromatium vinosum* [NiFe] Hydrogenase in the Oxidized "Ready" State" *Journal of Biological Inorganic Chemistry* **1999** *4* 379

92 H. McConnell, C. Heller, T. Cole, R. Fessenden. "Radiation Damage in Organic Crystals. I. $CH(COOH)_2$ in Malonic Acid" *JACS* **1960** *82* 766

93 P.J. O'Malley, G. Babcock. "Powder ENDOR Spectra of *p*-Benzoquinone Anion Radical: Principle Hyperfine Tensor Components for Ring Protons and for Hydrogen Bonded Protons" *JACS* **1986** *108* 3995

94 E. Davies. "A New Pulse ENDOR Technique" *Physics Letters A* **1974** *47* 1

95 W. Mims. "Pulsed ENDOR Experiments." *Proceedings of the Royal Society* **1965** *A283* 452

96 L. Rowan, E. Hahn, W. Mims. "Electron-Spin-Echo Envelope Modulation" *Physical Review* **1965** *137* A61

97 W.B. Mims. "Envelope Modulation in Spin-Echo Experiments" *Physical Review B* **1972** *5* 2409

98 A. Hassan, L. Pardi, J. Krzystek, A. Sienkiewicz, P. Goy, M. Rohrer, L-C. Brunel. "Ultrawide Badn Multifrequency High Field EMR Techique: A Methodology for Increasing Spectroscopic Information" *Journal of Magnetic Resonance* **2000** *142* 300

99 E. Solomon, M. Hanson. "Bioinorganic Spectroscopy" in *Inorganic Electronic Structure and Spectroscopy, Volume II: Applications and Case Studies* John Wiley and Sons, New York 1999 p. 1-22

100 J. McCracken. *Handbook of Electron Spin Resonance: Volume 2* Springer, New York 1999 Ed. C. Poole, H. Farach p. 69-76

101 Y. Deligiannakis, M. Louloudi, N. Hadjiliadis. "Electron Spin Echo Envelope Modulation (ESEEM) Spectroscopy as a Tool to Investigate the Coordination Environment of Metal Centers" *Coordination Chemistry Reviews* **2000** *204* 1

102 W. Holzapfel, U. Finkele, W. Kaiser, D. Oesterhelt, H. Scheer, H. Stilz, W. Zinth. "Observation of a Bacteriochlorophyll Anion During the Primary Charge Separation in a Reaction Center" *Chemical Physics Letters* **1989** *160* 1

103 S. Lotjonen, P. Hynninen. "An Improved Method for the Preparation of (10R)- and (10S)- Pheophytins *a* and *b*" *Synthesis* **1983** *?* 708

104 K. Iriyama, M. Yoshiura, M. Shiraki. "An Improved Method for Extraction, Partial Purification, Separation, and Isolation of Chlorophyll from Spinach Leaves" *Journal of Liquid Chromatography* **1977** *2* 255

105 T. Omata, N. Morata. "A Rapid and Efficient Method to Prepare Chlorophyll A and B from Leaves" *Photochemistry and Photobiology* **1980** *31* 183

106 J. van Tol, L-C. Brunel, R. Wylde. "A 120/240 GHz Transient Electron Spin Resonance Spectrometer" *Review of Scientific Instruments* **2003** In press.

107 Simulation software written by Brian Hoffman and Peter Doane. Available at http://endor1.chem.northwestern.edu/

108 W. Lubitz, F. Lendzian, K. M"obius. "^{14}N and ^{1}H Nuclear Multiple Resonance Experiments on BChl*a* Anion Radicals in Solution." *Chemical Physics Letters* **1981** *81* 235

109 S. Sinnecker, W. Koch, W. Lubitz. "Bacteriochlorophyll *a* Radical Cation and Anion – Calculation of Isotropic Hyperfine Coupling Constants by Density Functional Methods." *Physical Chemistry Chemical Physics* **2000** *2* 4772

110 A. Shubin, S. Dikanov. "Determination of Hyperfine Tensor Components from Nuclear Frequencies at Canonical Orientations of the g-Tensor" *Journal of Magnetic Resonance* **2002** *155* 100

111 M. Fuchs, A. Schnegg, M. Plato, C. Schulz, R. M"uh, W. Lubitz, K. M"obius. "The Primary Donor Cation P^+ in Photosynthetic Reaction Centers of Site Directed Mutants of *Rhodobacter sphaeroides*: g-Tensor Shifts Revealed by High-Field EPR at 360 GHz / 12.8 T" In press, *Chemical Physics*

112 R. Isaacson, F. Lendzian, E. Abresch, W. Lubitz, G. Feher. "Electronic Structure of Q-A in Reaction Centers from *Rb. sphaeroides*. I. Electron Paramagnetic Resonance in Single Crystals" *Biophysical Journal* **1995** *69* 311

113 O. Burghaus, M. Plato, K. M"obius, F. MacMillan, W. Lubitz. "3-mm High-Field EPR on Semiquinone Radical Anions Q^- Related to Photosynthesis and on the Primary Donor P^+ and Acceptor Q_A^- in Reaction Centers of *Rhodobacter sphaeroides* R-26" *Journal of Physical Chemistry* **1993** *97* 7639

114 P. O'Malley. "Hybrid Density Functional Studies of a Bacteriopheophytin *a* Model and Its Anion Radical Form: Geometry, Spin Densities, and Hyperfine Couplings" *Journal of Computational Chemistry* **1999** *20* 1292

115 J. Fajer, D. Borg, A. Forman, D. Dolphin, R. Felton. "Pi-Cation Radicals and Dications of Metalloporphyrins" *JACS* **1970** *92* 3451

116 J. Fajer, D. Borg, A. Forman, D. Dolphin, R. Felton. "Anion Radical of Bacteriochlorophyll" *JACS* **1973** *93* 2739

117 J. Norris, M. Druyan, J. Katz. "Electron Nuclear Double Resonance of Bacteriochlorophyll Free Radical *in Vitro* and *in Vivo*" *JACS* **1973** *95* 1680

118 J. Hoff, K. M"obius. "Nitrogen ENDOR and Proton Triple Resonance Experiments on the Bacteriochlorophyll Cation in Solution." *PNAS USA* **1978** *75* 2296

119 D. Borg, A. Forman, J. Fajer. "ESR and ENDOR Studies of the Pi Cation Radical of Bacteriochlorophyll" *JACS* **1976** 6889

120 J. Fajer, D. Borg, A. Forman, R. Felton, D. Dolphin, L. Vegh. "The Cation Radicals of Free Base and Zinc Bacteriochlorin, Bacteriochlorophyll, and Bacteriopheophytin" *PNAS USA* **1974** *71* 994

121 J. McElroy, G. Feher. "On the Nature of the Free Radical Formed During the Primary Process of Bacterial Photosynthesis" *BBA* **1969** *172* 180

122 A. Bresgunov, A. Dubinsky, O. Poluektov, Y. Lebedev. "The Structure of Phenoxyl Radicals as Studied by 2mm Band ESR" *Molecular Physics* **1992** *75* 1123

123 F. Lendzian, K. M"obius, M. Plato, U. Smith, M. Thurnauer, W. Lubitz. "^{25}Mg ENDOR and TRIPLE Resonance in Liquid Solution of BChl*a* Cation and Anion Radicals." *Chemical Physics Letters* **1984** *111* 583

124 P. Bratt, M. Rohrer, J. Krzystek, M. Evans, L.-C. Brunel, A. Angerhofer. "Submillimeter High-Field EPR Studies of the Primary Donor in Plant Photosystem I" *Journal of Physical Chemistry B* **1997** *101* 9686

125 N. Atherton. *Electron Spin Resonance* John Wiley and Sons, New York 1973

126 S. Sinnecker, W. Koch, W. Lubitz. "Chlorophyll a Radical Ions: A Density Functional Study" *J. Phys. Chem. B* **2002** *106* 5281

127 P. O'Malley. "The Effect of Oxidation and Reduction of Chlorophyll *a* on Its Geometry, Vibrational and Spin Density Properties as Revealed by Hybrid Density Functional Methods" *JACS* **2000** *122* 7798

128 M. Berry, P. Bratt, M. Evans. "Relaxation Properties of the Photosystem 1 Electron Transfer Components: Indications of the Relative Positions of the Electron Transfer Cofactors in Photosystem 1" *BBA-Bioenergetics* **1997** *1319* 163

129 N. White, G. Beddard, J. Thorne, T. Freehan, T. Keyes, P. Heathcote. "Primary Charge Separation and Energy Transfer in the Photosystem I Reaction Center of Higher Plants" *Journal of Physical Chemistry* **1996** *100* 12086

130 Y. Wang, X. Hu. "Quantum Chemical Study of Pi-Pi Stacking Interactions of the Bacteriochlorophyll Dimer in the Photosynthetic Reaction Center of *Rhodobacter sphaeroides" Journal of Chemical Physics* **2002** *117* 1

131 H. Scheer, J. Katz, J. Norris. "Proton-Electron Hyperfine Coupling Constants of the Chlorophyll *a* Cation Radical by ENDOR Spectroscopy" *JACS* **1976** *99* 1372

132 A. Hoff, F. Lendzian, K. M"obius, W. Lubitz. "Proton and Nitrogen Electron Nuclear Double and Triple Resonance of the Chlorophyll a Anion in Liquid Solution" *Chemical Physics Letters* **1982** *85* 3

BIOGRAPHICAL SKETCH

Lee Matthew Walker was born in Charlottesville, VA on the second day of August, 1975. His high school education took place at the Darlington School in Rome, GA. Lee then moved on for undergraduate education at Centre College in Danville, KY where he earned a Bachelor of Science degree in chemical physics. His love for the physical sciences brought him to graduate school in this area, and his love for his family brought him back to Florida. Little did he know that fate had planted him in Gainesville where we would find the love of his life. Now his life is truly complete, with a loving wife, a career ahead, and an inspiration to share.

I certify that I have read this study and that in my opinion it conforms to acceptable standards of scholarly presentation and is fully adequate, in scope and quality, as a dissertation for the degree of Doctor of Philosophy.

Alexander Angerhofer

Alex Angerhofer, Chairman
Associate Professor of Chemistry

I certify that I have read this study and that in my opinion it conforms to acceptable standards of scholarly presentation and is fully adequate, in scope and quality, as a dissertation for the degree of Doctor of Philosophy.

William Weltner

William Weltner
Professor of Chemistry

I certify that I have read this study and that in my opinion it conforms to acceptable standards of scholarly presentation and is fully adequate, in scope and quality, as a dissertation for the degree of Doctor of Philosophy.

Philip Brucat
Associate Professor of Chemistry

I certify that I have read this study and that in my opinion it conforms to acceptable standards of scholarly presentation and is fully adequate, in scope and quality, as a dissertation for the degree of Doctor of Philosophy.

Ben Horenstein
Associate Professor of Chemistry

I certify that I have read this study and that in my opinion it conforms to acceptable standards of scholarly presentation and is fully adequate, in scope and quality, as a dissertation for the degree of Doctor of Philosophy.

David Silverman
Distinguished Professor of Pharmacology
and Therapeutics

This dissertation was submitted to the Graduate Faculty of the Department of Chemistry in the College of Liberal Arts and Sciences and to the Graduate School and was accepted as partial fulfillment of the requirements for the degree of Doctor of Philosophy.

August 2003

Dean, Graduate School